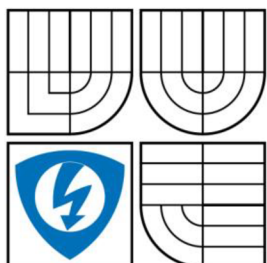


VYSOKÉ UČENÍ TECHNICKÉ V BRNĚ
BRNO UNIVERSITY OF TECHNOLOGY



FAKULTA ELEKTROTECHNIKY A KOMUNIKAČNÍCH
TECHNOLÓGIÍ
ÚSTAV BIOMEDICÍNSKÉHO INŽENÝRSTVÍ

FACULTY OF ELECTRICAL ENGINEERING AND COMMUNICATION
DEPARTMENT OF BIOMEDICAL ENGINEERING

CALIBRATION OF AN ULTRASONIC TRANSMISSIVE COMPUTED TOMOGRAPHY SYSTEM

KALIBRACE ULTRAZVUKOVÉHO PRŮZVUČNÉHO SYSTÉMU VÝPOČETNÍ TOMOGRAFIE

DOKTORSKÁ PRÁCE
DOCTORAL THESIS

AUTOR PRÁCE
AUTHOR

Ing. ADAM FILIPÍK

VEDOUCÍ PRÁCE
SUPERVISOR

prof. Ing. JIŘÍ JAN, CSc.

BRNO 2009

Keywords

Transmissive ultrasonic computed tomography, ultrasound attenuation imaging, sensitivity calibration, geometrical calibration

Klíčová slova

Průzvučná ultrazvuková počítačová tomografie, zobrazování ultrazvukového útlumu, kalibrace citlivostí, geometrická kalibrace

Acknowledgements

This dissertation thesis would have not been possible without the support of several people.

First of all, I want to thank my academic advisor Prof. Jiří Jan for giving me direction throughout the whole doctoral study. His observations made me rethink and reformulate large parts of the dissertation work making it more clear and concise.

A special thank goes to all members of the Karlsruhe USCT team, namely Dr. Rainer Stotzka, Dr. Nicole Rüter, and Michael Zapf, who gave me excellent support during the months I spent in the Karlsruhe Forschungszentrum.

Further I would like to thank all members of the DAR team, who formed a very good basis for exchanging ideas. Especially Radovan Jiřík PhD gave me a lot of advice in the initial stages of work and also formed the route I would take in this dissertation. Igor Peterlík PhD and Dušan Hemzal PhD I want to thank for helping me mathematically formulate some of the most important parts of the dissertation.

Many thanks also go to my fellow doctoral students making the studies enjoyable and unforgettable.

And last but most importantly I want to thank my wife and my parents for giving me support throughout my whole studies. Thank you.

Frame of the dissertation

The presented dissertation project has been running from September 2003 to August 2009 at the Department of Biomedical Engineering, Brno University of Technology, under the academic supervision of Prof. Jiří Jan. The work direction was determined by the long-term orientation of research in the department towards ultrasonic related problems and especially by the research cooperation with the Institute of Data Processing and Electronics, Forschungszentrum Karlsruhe (German National Research Center).

A substantial part of the experimental research was done in the Karlsruhe research facility, where the author joined the development team several times for a total of 4 months. The team in Karlsruhe is developing a prototype of a novel 3D ultrasound tomography system aimed at breast cancer screening. The cooperation and the research visit were great sources of inspiration, exchange of ideas, and most importantly experimental data, on which newly developed methods could be tested.

One of the main problems in the Karlsruhe USCT prototype was the absence of any calibration. The thousands of transducers used in the system have deviations in sensitivity, directivity, and frequency response. Moreover, these parameters change over time as the transducers age. Finally (and most importantly), the mechanical positioning of the transducer elements is not precise. All these aspects greatly affect the overall quality of the reconstructed images. The problem of calibration of a USCT system was chosen as the main topic for this dissertation.

The dissertation work and the stay in the Karlsruhe research facility was supported by:

- National research center DAR (Data, Algorithms, and Decision making), sponsored by the Ministry of Education, Czech Republic, project no. 1M6798555601
- Bilateral Czech-German agreement AVČR - DAAD (grants no. D-CZ 22/05-06 and D12-CZ9/07-08 and the grants of the German Academic Exchange Service)
- Research frame of the FEEC BUT (Ministry of Education, Czech Republic), project no. MS 0021630513 (MS 1850023)

Used Acronyms

- DOP – dilution of precision (described in detail in chapter 2.4.1.4)
- FZK – Forschungszentrum Karlsruhe
- GPS – global positioning system
- ITE – individual transducer element, an alternative approach to the novel geometrical calibration technique (described in chapter 6.1.1)
- TAS – transducer array system, a module consisting of several ultrasound transducer elements (chapter 2.2.2.2) or also an alternative approach to the novel geometrical calibration technique (described in chapter 6.1.2)
- TOA – time-of-arrival
- TOF – time-of-flight
- USCT – ultrasound computer tomography
- XCT – X-ray computer tomography

Contents

ACKNOWLEDGEMENTS	II
FRAME OF THE DISSERTATION	III
USED ACRONYMS	IV
1. INTRODUCTION	5
1.1 COMPUTED TOMOGRAPHY SYSTEMS	5
1.2 ULTRASOUND COMPUTED TOMOGRAPHY	6
1.2.1 <i>Example of a USCT system</i>	6
1.2.2 <i>History of USCT</i>	7
1.3 IMAGE RECONSTRUCTION PRINCIPLES	8
1.3.1 <i>Filtered backprojection</i>	8
1.3.2 <i>Diffraction tomography</i>	10
1.3.3 <i>Reflectivity imaging</i>	11
1.3.4 <i>Algebraic Reconstruction Techniques</i>	12
1.4 THE NEED FOR CALIBRATION	12
2 STATE OF THE ART IN USCT	14
2.1 ULTRASOUND COMPUTED TOMOGRAPHY SYSTEMS	14
2.1.1 <i>High-Resolution Ultrasonic Transmission Tomography System</i>	14
2.1.2 <i>The Ring Transducer System for Medical Ultrasound Research</i>	14
2.1.3 <i>A diffraction tomography system</i>	15
2.1.4 <i>Computerized Ultrasound Risk Evaluation (CURE) program</i>	16
2.1.5 <i>Karlsruhe USCT system</i>	17
2.2 KARLSRUHE USCT SYSTEM AND PREVIOUS RESULTS	17
2.2.1 <i>The Karlsruhe 2D USCT system</i>	17
2.2.2 <i>The Karlsruhe 3D USCT system</i>	18
2.2.2.1 <i>System architecture</i>	18
2.2.2.2 <i>Transducer array systems - TAS</i>	19
2.2.3 <i>FZK Reconstruction method (the sum-and-delay algorithm)</i>	20
2.3 PUBLISHED SENSITIVITY CALIBRATION METHODS.....	22
2.4 KNOWN POSITION CALIBRATION METHODS	23
2.4.1 <i>Global Positioning System (GPS)</i>	23
2.4.1.1 <i>Pseudorange equations</i>	24
2.4.1.2 <i>Linearization</i>	24
2.4.1.3 <i>Solving the system of equations</i>	25
2.4.1.4 <i>Dilution of Precision (DOP)</i>	27
2.4.1.5 <i>The use of GPS principles in USCT</i>	28
2.4.2 <i>A published GPS modification for an ultrasonic systems</i>	28
2.4.2.1 <i>The calibration method</i>	29
2.4.3 <i>The RTS calibration approach</i>	31
2.4.4 <i>Multidimensional scaling</i>	31
2.4.5 <i>Localization methods in wireless networks</i>	33
3 AIMS OF THE DISSERTATION	34
4 A CONTRIBUTION TO ATTENUATION IMAGE RECONSTRUCTION	35
4.1 ATTENUATION COEFFICIENT CALCULATION	35
4.2 THE STRAIGHT BEAM RECONSTRUCTION	36
4.3 THE REFLECTED BEAM RECONSTRUCTION	38
4.4 RECONSTRUCTION RESULTS	39
5 NOVEL TRANSDUCER SENSITIVITY CALIBRATION METHOD	41
5.1 THE 2D SENSITIVITY CALIBRATION METHOD	41

5.1.1	<i>The measured signal model</i>	41
5.1.2	<i>The equation system</i>	42
5.1.3	<i>Stabilizing the system</i>	42
5.1.4	<i>Sensitivity calibration results based on experimental data</i>	44
5.1.4.1	Verification via hydrophone measurement	45
5.1.4.2	Comparison with wave-equation based simulation	46
5.2	THEORETICAL EXTENSION TO 3D	47
6	NOVEL TRANSDUCER POSITION CALIBRATION METHOD	49
6.1	FORMULATION OF THE POSITION CALIBRATION METHOD	49
6.1.1	<i>The ITE (individual transducer element) approach</i>	50
6.1.2	<i>The TAS (transducer array system) approach</i>	53
6.2	ANCHORING	56
6.2.1	<i>Position anchoring</i>	57
6.2.1.1	Dilution of precision (DOP)	57
6.2.1.2	Minimizing the DOP for a 2D USCT	58
6.2.1.3	Minimizing the DOP for a 3D USCT	59
6.2.2	<i>Time-delay anchoring</i>	63
6.2.3	<i>The rank deficiency test</i>	64
6.3	NUMERICAL ANALYSIS AND TESTING	64
6.3.1	<i>Convergence analysis</i>	64
6.3.2	<i>Condition number analysis</i>	66
6.3.3	<i>Noise effect analysis</i>	67
6.4	ALTERNATIVE SOLUTIONS TO THE CALIBRATION PROBLEM	69
6.4.1	<i>The Levenberg-Marquardt algorithm</i>	69
6.4.2	<i>The weighted least squares approach</i>	70
6.4.3	<i>Solution based on a common time-delay parameter</i>	70
6.4.4	<i>Solution based on angle-dependent common time-delay</i>	71
6.4.5	<i>Theoretical extension to a thread-phantom-based calibration</i>	71
6.4.5.1	2D thread reflections	71
6.4.5.2	3D thread reflections	72
6.4.5.3	Expressing the TOA equations	74
6.4.5.4	Phantom description	75
6.5	POSITION CALIBRATION OF THE KARLSRUHE 3D USCT SYSTEM	76
6.5.1	<i>Extracting the TOA from A-scans</i>	76
6.5.1.1	Pulse detection	77
6.5.1.2	Pulse selection	79
6.5.2	<i>Analysis of measurement errors</i>	83
6.5.2.1	Speed of sound errors	83
6.5.2.1.1	Thermometer errors	84
6.5.2.1.2	Temperature variations	84
6.5.2.1.3	Error of the speed of sound	85
6.5.2.2	Thermal expansion errors	86
6.5.3	<i>Calibration results based on experimental data</i>	87
6.5.3.1	The ITE and the TAS approaches	87
6.5.3.2	Different TOA selection methods	88
6.5.3.3	Alternative calibration solutions	88
7	CONCLUSION	93
7.1	DISCUSSION OF THE ACHIEVED RESULTS	93
7.1.1	<i>Attenuation image reconstruction</i>	93
7.1.2	<i>Sensitivity calibration</i>	93
7.1.3	<i>Geometrical calibration</i>	94
7.2	SUGGESTIONS FOR FURTHER RESEARCH	95
7.2.1	<i>Ethanol solution measurement medium</i>	95
7.2.2	<i>3D extension to sensitivity calibration</i>	95
7.2.3	<i>Thread phantom calibration</i>	95
7.2.4	<i>LSQR solution to the system of equations</i>	96
7.2.5	<i>Different pulse shapes, Pulse trains, Chirps</i>	96

	7.2.6	<i>Single- and double-differences</i>	96
8		REFERENCES	97
9		LIST OF AUTHOR'S PUBLICATIONS	101

1. Introduction

This dissertation is centered on a medical imaging modality – the ultrasonic computed tomography (USCT) – and algorithms which improve the resulting image quality, namely the calibration of a USCT device.

The USCT is in principle capable of producing quantitative 3D image volumes with high resolution and tissue contrast. Although the idea of USCT has been around for more than three decades, the lack of computing power did not allow the scientists and engineers to make full use of its potential. With computers that are more and more powerful, the idea of USCT came back to life and at the moment several teams around the world are experimenting on prototypes of USCT scanners.

The USCT is primarily aimed at breast cancer diagnosis. Breast cancer is the most common cancer among women worldwide. In 2000, the last year for which global data exists, over one million cases have been diagnosed around the world and some 400.000 women have died, representing 1.6 per cent of all female deaths. Early detection of breast cancer is vital since early detection has repeatedly been shown to improve the chance of survival [74].

X-ray mammography, magnetic resonance, and the conventional ultrasound are established methods for breast cancer diagnosis. Currently the most common modality used for breast cancer diagnosis is X-ray, but is often supplemented with an ultrasound examination, which in many cases leads to additional information about e.g. cysts and fibroadenomas. Besides the fact that ultrasound is much less expensive than X-ray mammography, it can be applied more frequently. There is still an ongoing debate about the limits on the energy which the human tissue should be exposed to by ultrasonic waves (especially the thermal damage to the nervous system is a potential risk [6]). Ultrasound waves are however not ionizing and can therefore be applied on a regular basis.

The disadvantage of the conventional echo ultrasound methods is mainly poor resolution and therefore the inability to reliably detect microcalcifications. Both the resolution and contrast depend on the distance of the ultrasonic probe from the region of interest inside the breast. As the medical doctor tries to get as close to the desired area, the breast gets deformed, and therefore exact measurements of the tissue structure, e.g. the tumor size are hardly possible. The image contents and their quality are highly dependable on the expertise of the examiner and are hardly reproducible.

In the following subchapters of the introduction, the principles USCT will be explained. First a brief overview of the kinds of existing computed tomography systems (used in medical imaging) is given in chapter 1.1. Chapter 1.2 gives explanations on the principles of the USCT and some ultrasound-specific aspects of this imaging modality. The general principles of image reconstruction methods are explained in chapter 1.3. Finally, chapter 1.4 shortly describes why there is a need to calibrate USCT systems and what can be calibrated.

1.1 *Computed tomography systems*

Tomographic systems, are systems providing images by sections. Computed tomography systems are those, which feed the collected data to a tomographic reconstruction software yielding the tomographic images after being processed by a computer. The modern systems usually reconstruct a whole 3D volume and then offer the examiners to view a 2D slice of the volume at any angle.

The computed tomography systems currently used for medical imaging can be classified into the following categories according to the imaging medium or the basic imaging principle [29]:

- X-ray computed tomography (XCT)
- Nuclear imaging (SPECT and PET)
- Ultrasonic imaging (USG)
- Magnetic resonance imaging (MRI)
- Electrical impedance tomography (IT)

Although the conventional B-mode ultrasonography is usually not considered a computed tomography system, because in principle it does not need a computer to yield sectional images, the generation of images in all modern systems is assisted by a computer. This is especially true, when considering the new three-dimensional ultrasonic systems or freehand ultrasound [7], [29].

The ultrasonic computed tomography (USCT) is a completely new approach combining the conventional ultrasonic imaging with the principles of image reconstruction used in XCT.

1.2 Ultrasound computed tomography

The ultrasonic computed tomography is an imaging modality which combines the phenomenon of ultrasound and some image reconstruction principles developed for other tomographic systems. The basic objective of a USCT system is the same as for other tomographic equipment: to obtain scans of all possible directions around the object and then reconstruct the entire volume. In comparison with the conventional B-mode ultrasound, the USCT receiving transducer elements need not necessarily be in the same place as the emitting elements. Therefore these systems are sometimes referred to as transmissive ultrasound systems.

1.2.1 Example of a USCT system

In practice, a USCT system can resemble the following: thousands of ultrasonic transducers attached to the inner side of a circular frame encompass the imaged object. Since the ultrasonic waves are not transmissible in the air (at the frequencies used in diagnostic medicine), water has to be used as coupling medium to create an acoustic link.

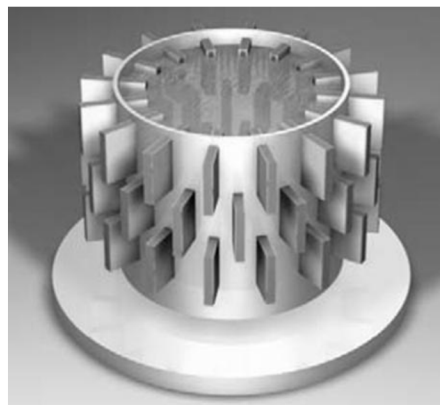


Figure 1-1: A schematic drawing of the Karlsruhe 3D USCT prototype. (Taken from [69])

Scanning is done in the following way: one emitter at a time broadcasts a broadband ultrasonic pulse wave and all receivers record the direct, reflected and scattered ultrasonic waves. This procedure is repeated for each emitter separately creating a fan projection each time (Figure 1-2).

Several ultrasonic properties of the scanned object can be estimated from each of the acquired signal can. These are: attenuation, reflectivity and the speed of sound. Here we can find a difference from the X-ray tomography in which it is only possible to calculate the atten-

uation of the ray intensity as it passes through the human tissue. An XCT detector integrates the radiation over a small period of time resulting in one value of intensity. The USCT receivers however, can record longer signals containing a series of immediate pressure values.

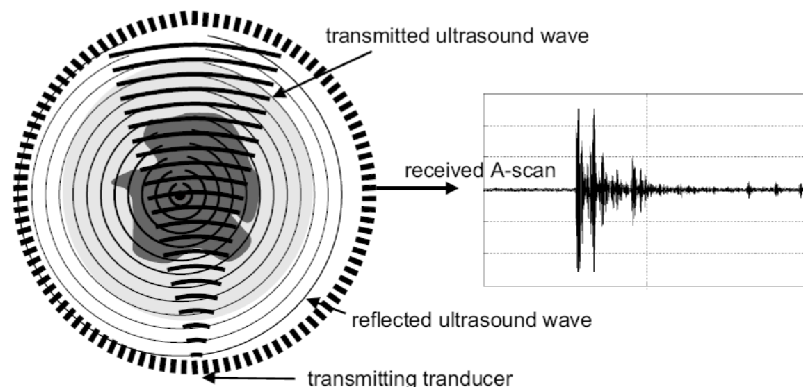


Figure 1-2: Architecture of the 2D USCT system built in Karlsruhe. A ring of ultrasonic transducers surround the examined object. One transducer transmits an ultrasonic pulse while all other transducers receive simultaneously. (Taken from [65])

Thus, USCT offers significantly more information about the scanned object. At the same time, this approach poses great problems as the volume of the recorded data dramatically increases and one has to deal with increased demands on storage space and processing speed.

1.2.2 History of USCT

The idea of ultrasound tomography is not new. The earliest attempts were made in the late seventies and early eighties of the last century. One of the first works in this area [21] dealt with only reconstructing the absorption of the tissue, the same property (in terms of signal processing) as the one reconstructed in the XCT systems. Soon, however, it was clear that the USCT systems have a much greater potential. The speed of the ultrasound waves is relatively small (compared to the speed of electromagnetic waves - the speed of light) and easily measured. Because it varies in different kinds of tissues, the local velocity is an additional parameter which can be reconstructed [22].

Norton and Linzer [52] showed that it is possible to reconstruct the “reflectivity” (like the conventional B-mode systems). Although reflectivity is not a precisely defined property of the tissue and corresponds to a combination of scattering, refraction and reflection, the images provide information about the structure of the tissue and have a high diagnostic value. This work also developed the idea of using unfocused transducers, which emit into the whole scanned volume. In previous experiments only transducers radiating a narrow focused ultrasonic beam were used. This change corresponds to the transition of XCT systems from the first to the third generation. Making one projection of the entire area at once, rather than sequentially, shortens the minimum period of capturing the entire scene from several hours to several seconds.

In spite of the limited technology available to these investigators, they showed promising results. For example, Greenleaf et al. achieved a sensitivity of 100% for palpable lesions with USCT for a small sample population [23]. In a larger study (n=78), Schreiman et al. showed that a computer-aided diagnosis using USCT had a sensitivity of 82.5% for the diagnosis of a malignancy [62].

One of the biggest problems encountered was the enormous amounts of data flows, which the technology was not able to cope with. Especially the researchers were not able to record enough data (at least not quickly enough) [34]. And so after the first years of significant

development, USCT gradually retreated from the practical implementation (the companies Philips and Siemens closed their programs of developing commercial systems), and further work continued primarily on the theoretical level [4]. In the last decade or two, however, the researchers have again slowly gained interest and the topic of USCT has been reopened. The most recent approaches are documented in chapters 2.1 and 2.2.

1.3 Image reconstruction principles

The first approaches to reconstruct images of the USCT led naturally in the footsteps of the already developed methods used in XCT. These methods assume the radiation of signals along straight thin lines - rays. The phenomena such as reflection, refraction and scattering are not taken into account. In such cases the *filtered backprojection* can be used as an effective method to reconstruct attenuation and velocity images (chapter 1.3.1). A different approach the *diffraction tomography* allows the “rays” to be slightly bent (1.3.2). Finally, *reflectivity imaging* takes advantage of the whole length of the recorded ultrasonic signals (chapter 1.3.3).

1.3.1 Filtered backprojection

The simplest (and a very fast) method of reconstruction is called the backprojection method. The method assumes that the imaging system collects data organized in the so-called *projections*

$$p_{\theta_0}(\tau) = \int_{R_\tau} f(x, y) dr. \tag{1.1}$$

Any projection $p_{\theta_0}(\tau)$ at an angle θ_0 consists of a set of *ray-integrals* (Figure 1-3). Each ray-integral is an individual measurement of a two-dimensional function $f(x, y)$ (representing the distribution of a certain parameter to be imaged) integrated along a straight line.

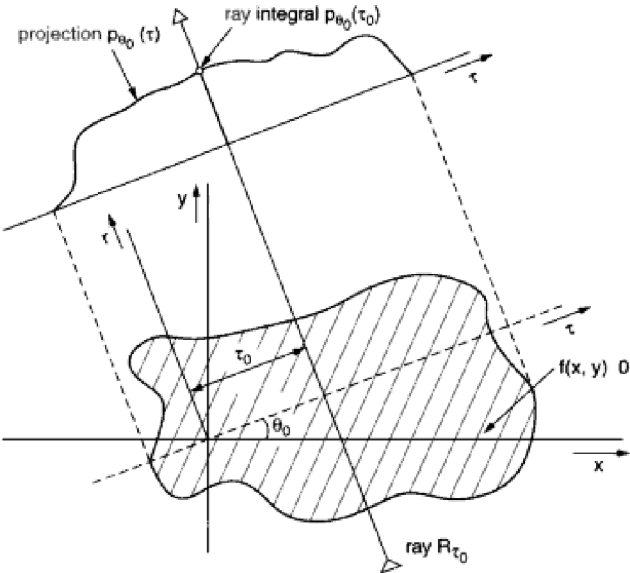


Figure 1-3: Ray integrals and a projection representation of an image. (Taken from [29])

If we have a continuous two-dimensional function (a so called sinogram)

$$p(\tau, \theta) = \int_{R_{\tau, \theta}} f(x, y) dr, \quad \tau \in (-\infty, \infty), \quad \theta \in (0, 2\pi) \quad (1.2)$$

both in θ and τ , it is possible to invert it using the inverse Radon transform, and obtain the original function $f(x, y)$ - the reconstructed image. Although the inverse Radon transform shows that, the original image can be reconstructed from its projections, it is very unstable in the presence of measurement noise.

The backprojection algorithm is a practically usable and a stable alternative to the inverse Radon transform. It follows a simple logic that each projection can be “smeared” back into the image in the direction originally used to for the projection. The resulting image is then the composition of all the smeared projections, where every point (x, y) is contributed to by a single value (the ray-integral) from each projection.

$$b(x, y) = \int_0^\pi p_\theta(\tau) d\theta = \int_0^\pi p_\theta(x \cos \theta + y \sin \theta) d\theta \quad (1.3)$$

The backprojection is not equivalent to the inverse Radon transform. Because the projections are smeared over the whole reconstruction plain (x, y) , an original image consisting of a single point will be reconstructed with non-zero values also outside of that point. A modification of this algorithm was developed to account for this difference and is known as the filtered backprojection

$$f(x, y) = \int_0^\pi q_\theta(\tau) d\theta = \int_0^\pi q_\theta(x \cos \theta + y \sin \theta) d\theta \quad (1.4)$$

where the modified projection $q_\theta(\tau) = p_\theta * h|\tau)$ is the convolution of the original projection with a ramp filter h having a ramp-like frequency response $|w|$ (linearly growing with the frequency). The derivation the filtered backprojection is closely related to the Fourier slice theorem and is documented in numerous publications [7],[10],[12],[27],[28],[29],[35].

The backprojection algorithm can also be implemented in the frequency domain using the so called *slice theorem*. The slice theorem relates the spectrum of a two-dimensional function to the spectrum of its parallel projection:

$$\mathfrak{F}\{p_\theta(\tau)\} = \mathfrak{F}_{2D}\{f(x, y)\}(\omega \cos \theta, \omega \sin \theta) \quad (1.5)$$

That is, the spectrum of the projection $p_\theta(\tau)$ obtained from the image $f(x, y)$ is equal to the central slice, at the angle θ , of the two-dimensional image spectrum [29].

This theorem can be used to reconstruct an image from its projections in the following way. Each parallel projection is first transformed (by DFT) into its one-dimensional spectrum. The spectra are then filled according to the theorem (as central slices) into a two-dimensional function which becomes the two-dimensional spectrum of the image. Interpolation is needed to resample the 2D spectrum from polar to rectangular grid. Finally a 2D inverse DFT is applied yielding the reconstructed image.

The USCT devices usually do not provide data in the form of projections with parallel ray paths. In modern USCT systems, the transducers are usually placed on a circular frame. When the emitting element sends out a pulse wave it is recorded at once by all the receivers as fan-shaped equiangular projection.

In order to be able to use the backprojection algorithm (which is only suited for the parallel projection geometry) a procedure called *rebinning* is necessary to apply to the collected data. The main idea of rebinning is that each ray-integral from a fan projection $r_\beta(\alpha)$ can also

be a part of a parallel projection $p_\theta(\tau)$. Thus the equiangular fan-projections can be rearranged into parallel projections and subsequently used in the backprojection algorithm to reconstruct the image.

Attenuation imaging

The filtered backprojection algorithm is for instance suitable to reconstruct images of local attenuation of the scanned tissue. Ultrasonic attenuation is derived from the recorded signals. There are three basic ways of determining the attenuation: the energy ratio method, the frequency shift method, and the method of log-spectra differences [14].

All three methods require a reference measurement, which can be done by making a scan with only water inside the tank. Then the imaged object is inserted into the system and the scan is repeated. The attenuation values are then computed using both scans. Each calculated attenuation value represents the complete attenuation along the line from the emitter to the receiver - the ray-integral - and can be directly used as the input of the filtered backprojection algorithm, yielding an image representing the distribution of local attenuation in the scanned object.

Velocity imaging

The distribution of local ultrasonic velocity can be reconstructed in a similar manner as the attenuation. The velocity can be simply calculated by taking the distance between the emitter and receiver and dividing it by the measured time-of-flight of the ultrasonic pulse. Although this method is the most straightforward, it is not very easy to determine the exact moment of the arrival of the pulse. Rather than measuring the absolute velocities, one can obtain relative changes by making two scans (an empty one and one with the scanned object inside) [25].

No matter which method is used, the calculated speed of sound values (average velocities along the ultrasonic “rays”) can be again used to reconstruct an image of the local velocities inside the object using the filtered backprojection algorithm.

1.3.2 Diffraction tomography

The above-mentioned reconstruction method assumes the radiation of the ultrasonic signals along straight thin rays. This assumption is not always valid, especially in the cases where the size of displayed objects is approximately same as the size of the ultrasound pulse wavelength. In such an environment, diffraction becomes a significant factor in the propagation of the waves. The wave equations are then the more suitable means to describe the propagation of waves [35].

The solution of the wave equations is usually only possible under certain simplifications. The two most cited are the Born and Rytov approximations (both simplify the equations by limiting the amount of diffraction to some small amount - about 10%) [35]. An important step in the reconstruction is the use of the Fourier diffraction theorem, which plays the same role in diffractive tomography as the slice theorem does in the conventional tomography.

The theorem (1.6) says that the Fourier spectrum of a parallel projection (after illumination of the object by a plane wave) is equal to the values of the two-dimensional spectrum of the image along a half-circle curve:

$$\begin{aligned} \mathfrak{S}\{p_\theta(\tau)\} = \mathfrak{S}_{2D}\{f(x,y)\} & \left(\omega \cos \theta - \left(\sqrt{K_0^2 - \omega^2} - K_0 \right) \sin \theta, \omega \sin \theta \right. \\ & \left. - \left(\sqrt{K_0^2 - \omega^2} - K_0 \right) \cos \theta \right) \end{aligned} \quad (1.6)$$

where $K_0 = 2\pi/\lambda$, and λ is the wave length. The radius of the curve is proportional to the frequency of the waves. If we increase the frequency of the waves (radiation) the radius gets larger and the curve straightens up. It can be said that the slice theorem is a good approximation of the diffraction theorem for high-frequency radiation sources like X-rays [10].

The diffraction theorem is used in a similar way in the reconstruction of the images as the slice theorem in the backprojection method in the frequency domain (compare to the slice theorem in eq. (1.5)).

1.3.3 Reflectivity imaging

The pioneering work on this topic was done by Norton and Linzer [52]. "Reflectivity" is understood as a property of the tissue causing the change of direction of the propagating ultrasound signal. It is not only the scattering but also refraction on the boundaries of parts of tissue with different acoustic impedance. The theory was originally designed for a circular two-dimensional scanning geometry, but it is simply extendable to three dimensions.

The previously mentioned methods make it possible to reconstruct the local attenuation or speed of sound properties of the scanned object. In velocity imaging it is the time-of-flight, in attenuation imaging it is the shape and magnitude of the first pulse in the recorded signal, which are used as the source of data for the reconstruction. Both modalities only utilize the properties of the first pulse giving information about the object along the straight line (the shortest path) between the emitter and receiver.

Reflectivity imaging, however, exploits the whole length of the recorded signals to obtain information about the object from non straight paths of propagation of the ultrasonic waves. The method somewhat resembles the B-mode ultrasound in that it uses the backscattered waves as the input data to build the image. It also goes further, not only because it is able to combine B-mode images from all sides of the object, but also use information of the scattering to all sides (not just the backscattering).

The reconstruction algorithm builds the image in the following way: each point in the resulting image accumulates values from the recorded signals, corresponding to the length of the reflection paths, that is, the sum of the paths from the emitter to the reflection point and from the reflection point to the receiver.

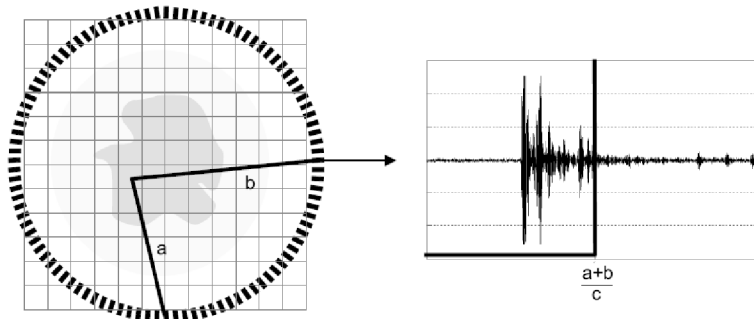


Figure 1-4: Reconstruction principle of reflectivity based on the assumption that the sound speed is constant (or similar enough) inside and outside of the scanned object. (Taken from [65])

The method assumes that the speed of sound is constant in and outside of the scanned object (Figure 1-4). A modification of the method assumes first reconstructing the velocity

map of the object and then using this information for the reflectivity imaging to account for the different speeds of sound.

Although no physical properties are reconstructed in reflectivity imaging, the images usually have a high information value considering the structure of the imaged object. Moreover, the images can be reconstructed with a sub-millimeter resolution.

1.3.4 Algebraic Reconstruction Techniques

Besides the backprojection algorithm there is another category of methods solving the problem of reconstructing images from projections. The algebraic methods are based on discretization of the projection area. The continuous function $f(x, y)$ is approximated by means of its samples $f_{i,k}$ via an interpolation

$$f(x, y) = \sum_{i=1}^I \sum_{k=1}^K f_{i,k} g_{i,k}(x, y) \quad (1.7)$$

The functions $g_{i,k}$ are usually staircase functions (having a constant non-zero value in the area of the pixel i, k), but generally can be any higher order interpolation function.

It is possible to rearrange $f_{i,k}$ into a column vector \mathbf{f} and create a matrix \mathbf{W} of weights with each row corresponding to the intersections of one beam with the scene pixels. Then we can express the set of measured values as the vector

$$\mathbf{W}\mathbf{f} = \mathbf{p} \quad (1.8)$$

This approach has the advantage that the ray-integrals in the projections do not necessarily need to be parallel or even straight! The shape of each ray (beam) is encoded into each row of the weight matrix \mathbf{W} .

To solve for the original image, the system only needs to be inverted

$$\mathbf{f} = \mathbf{W}^{-1}\mathbf{p} \quad (1.9)$$

And so, the problem of reconstructing an image has been transformed into a problem of solving a system of linear equations. Note that the matrix \mathbf{W} does not need to be square (depending on the number of projections) and in that case the resulting image is a least mean square solution (by e.g. pseudoinversion) of the problem.

Because the system of equations is usually too large to be solved by the conventional approaches (the number of elements of \mathbf{W} can reach up to the order 10^8 to 10^{12}), an iterative solution (SART, SIRT, Newton-Kazmarz method [28],[29]) is used.

1.4 The need for calibration

For the reconstruction of the tomographic images it is crucial to know the properties of the imaging system and especially the used transducers. For example in attenuation imaging, the frequency content of the first pulse must be correctly determined in order to truthfully reconstruct the local distribution of attenuation in the object.

The system usually operates at frequencies near the transducers' resonance and the transfer function of the transducers is usually highly variable up or down the spectrum. The frequently used wideband ultrasonic pulses get distorted first in the emitter and then also in the receiver transducer. After such distortions, the exact frequency content of the pulse is hard to determine correctly and some calibration is necessary.

The transducers also usually have a strong angular dependence. Besides a wide main lobe, side lobes can also be present which (if not accounted for in a calibration step) can cause strong artifacts in the reconstructed images.

Both of the above described phenomena (the frequency and angular dependencies of the transducers) are usually known already during design time, and can therefore be built into some internal correction of the system from the beginning. But transducers are subject to aging and these properties change. Especially the overall sensitivity might degrade by several magni-

tudes. Such transducers add a lot of noise to the signals and the reconstruction, without a proper calibration, is again prone to give faulty images full of artifacts.

Finally, new USCT systems consist of thousands of independent transducers and it may not always be possible to build them with their positioning so precise as is needed for the reconstruction of e.g. velocity images. Differences of tenths of millimeters already cause deviations of several meters per second when estimating the speed of sound. In reflectivity images, small positioning errors might cause phase cancelation and again obscure the reconstructed image in artifacts.

The calibration of USCT systems is therefore a very important aspect of image reconstruction which, if applied properly, can lead to significant image quality improvement.

2 State of the art in USCT

This chapter discusses the recent advances in science in the field of ultrasound computer tomography and calibration techniques.

First, a list of present-day attempts to develop a fully functional ultrasound computed tomography system is presented in chapter 2.1. Only a brief overview is devoted to each project. More space is dedicated to the partnering Karlsruhe project (chapter 2.2), in which the author took part.

Chapters 2.3 and 2.4 are over viewing the up-to-date methods and techniques of transducer sensitivity calibration and position calibration. The presented methods are used in current ultrasound computer tomography systems, but also in other technical areas and were taken as a basis in development of the new calibration techniques by the author.

2.1 Ultrasound computed tomography systems

2.1.1 High-Resolution Ultrasonic Transmission Tomography System

A very promising new ultrasound system was described in IEEE Transactions on Medical Imaging in 2005. This “High-Resolution Ultrasonic Transmission Tomography System” (HUTT) was developed in the Department of Biomedical Engineering, University of Southern California, Los Angeles, CA, USA by Jeong et.al. [30].

Contrary to most of the other ultrasound tomography systems, this system uses high-frequency transmitters (center frequency 8 MHz with 50% bandwidth). The transducer elements are only 0.4mm x 0.4mm. The received signals are sampled at 100 MHz in a 14 bit A/D converter. The part of the recorded signal which contains the first-arrival pulse is extracted and processed for multi-band analysis, utilizing the frequency dependent characteristics of the acoustic attenuation.

The images are built by fusing conventional backprojection sinograms, each of which is set up for one of the frequency bands. The fusion is realized by a Local Principal Component Analysis that maps all of the narrow-band 3D sinograms into one, which is then reconstructed using the classical backprojection technique and a Shepp-Logan filter.

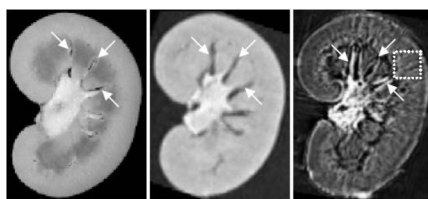


Figure 2-1: Reconstruction of a sheep kidney. The images were coregistered from three modalities: optical (left), MRI (middle) and HUTT (right). (Taken from [30])

2.1.2 The Ring Transducer System for Medical Ultrasound Research

This 2D ultrasound computed tomography system (Figure 2-2) has been developed for experimental studies of scattering and imaging. The ring transducer array (built by Nihon Dempa in Kogyo Co., Ltd., Tokyo, Japan) consists of 2048 rectangular elements with a 2.5-MHz center frequency, a 67% - 6 dB bandwidth, and a 0.23-mm pitch arranged in a 150-mm-diameter ring with a 25-mm elevation. At the center frequency, the element size is $0.30 \lambda \times 42 \lambda$ and the pitch is 0.38λ [73].

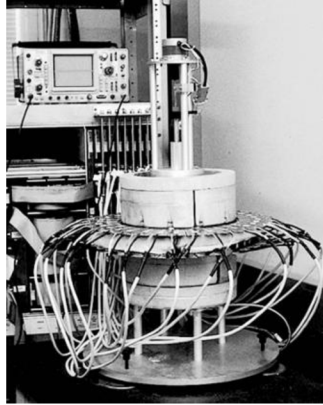


Figure 2-2: Ring transducer system photo. The ring transducer is in the center of the cylindrical apparatus and forms a portion of a cylindrical water tank that is temperature-controlled to $30^{\circ}\text{C} \pm 0.2^{\circ}\text{C}$. The electronics are in the background. A motorized gantry located above the ring permits test objects to be raised or lowered through the plane of the ring. (Taken from [73])

The system has 128 parallel transmit channels, 16 parallel receive channels, a 2048:128 transmit multiplexer, a 2048:16 receive multiplexer, independently programmable transmit waveforms with 8-bit resolution, and receive amplifiers with time variable gain independently programmable over a 40-dB range. Receive signals are sampled at 20 MHz with 12-bit resolution. Arbitrary transmit and receive apertures can be synthesized.

This system also incorporates a calibration mechanism to compensate for unavoidable element-to-element variations in sensitivity and time response and from deviation in element position from an ideal circle. The used algorithm is described in detail in chapter 2.4.3.

2.1.3 A diffraction tomography system

This system has been developed by Andre et. al. (Department of Radiology, Veterans Affairs Medical Center, San Diego, CA) for the purposes of experimenting with ultrasound computed tomography and its applications to breast imaging. Low-power discrete frequency sound in the range of 0.3–1.2 MHz, two cylindrical arrays of 512 and 1024 PZT transducers, and high spatial sampling of the wavefront are used [4].

As for the reconstruction, the system uses a diffraction tomographic reconstruction method. One transducer at a time is activated and allowed to reach steady state at which point the remaining transducers measure the phase and amplitude of the ultrasound signal. The image is formed by inverting the wave equation and calculating a complex scattering potential at all locations in the 2D plane. The wave equation simplifies to an expression with Henkel and Bessel functions because the transducers work only in discrete frequencies.

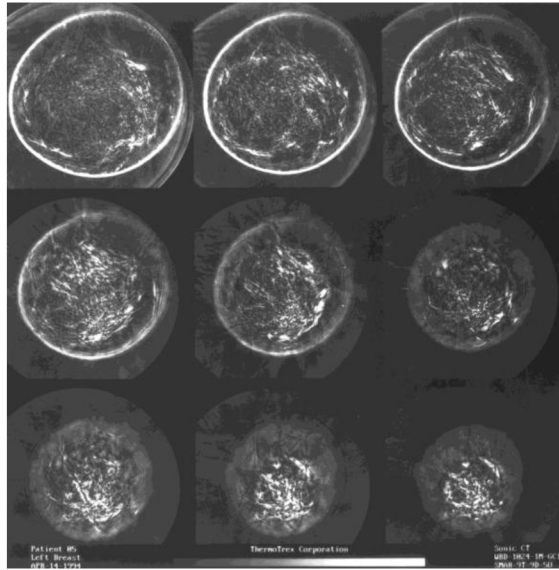


Figure 2-3: Nine sequential image slices through entire breast with ~4-mm overlap from nipple to the chest wall. Magnitude with aberration correction. (Taken from [4])

The team published very promising reconstruction images of in-vivo breast as early 1997 [2][3][4], and for a few following years had no activity. More recently an analysis of patient breast images from a clinical trials series of 25 patients has been published [33]. The study suggests that ultrasound diffraction tomography has the potential for discriminating between different tissue types. The authors also conclude that the image contrast values of malignant lesions provide sufficient discrimination from normal breast tissue to be potentially of diagnostic value.

2.1.4 Computerized Ultrasound Risk Evaluation (CURE) program

The Karmanos Cancer Institute (KCI) in collaboration with Lawrence Livermore National Laboratory (LLNL) has built an ultrasound scanning system designed to simulate virtually any transducer array design [40]. The system has six degrees of freedom and has been optimized for signal-to-noise (SNR), pulse shape, minimization of systematic errors, and automated preprocessing.

As the authors claim, the system is very flexible. In one of the documented experiments, the system comprised of two identical line transducers (0.38 mm wide and 12 mm high) movable in a circular geometry. The relative positions of the two transducers positioned with accuracy 0.05 mm or higher. For each position of the transducer, the receiver was moved around a 320 degree circular path of radius 15 cm. The transmitter emitted a pulse for each position of the receiver for up to 1600 receiver positions (position increments of 0.2 deg). The transmitter position was also moved along the circular path and the firing sequence repeated for each new position of the transmitter [16].

The targets were placed at the center of the ring with the long axis of the cylindrical phantom oriented vertically relative to the plane of the ring. Each data set represents a 2-D slice through the target. The ring plane was translated in the vertical direction allowing for 3-D reconstructions from stacked 2-D planes of data. All scans were performed at 10 mm slice thickness, as determined by the beam width of the transducers. The data sets resulting from the above scans were typically ~ 2 GB per slice. The raw data sets consisted of measured pulse trains, processed to determine the frequency spectrum and arrival time for each pulse. The arrival times were used to construct reflectivity and sound speed images while the pulse spectrum data were used to determine the attenuation [16].

The collaborating groups tried several different reconstruction approaches resulting in a comparison study published in [40]. An example of a reconstructed image can be seen in Figure 2-4.

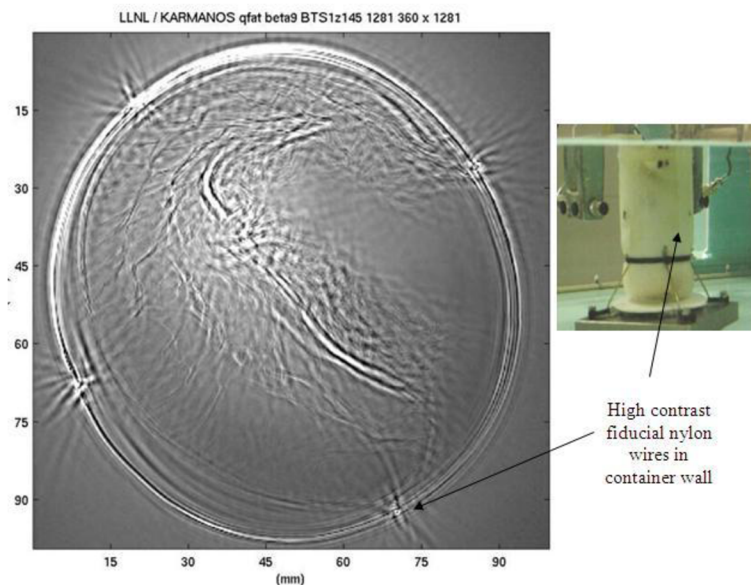


Figure 2-4: Full aperture tomography (FAT) reconstruction of a cadaveric breast placed in formalin and sealed in a 100mm container. The phantom surrounded by the transducer arms of the scanner can be seen on the right. (Taken from [40])

More recently, the group has carried out a study with 19 patients whose mammograms and follow-up ultrasound identified suspicious masses. The CURE exam was interposed between the standard US exam and subsequent biopsy. Biopsy results were therefore available for all 19 patients. Based on the preliminary CURE data the group has utilized six CURE diagnostic criteria for cancer. In the small sample, it appears that women with higher scores are more likely to have cancerous masses [17].

2.1.5 Karlsruhe USCT system

Finally, the USCT system built in the Forschungszentrum Karlsruhe (FZK) will be given a separate chapter as all of the data which the author worked on originated from here.

2.2 Karlsruhe USCT system and previous results

The initiator of the whole project, Dr. Stotzka, developed the first experimental 2D prototype of the USCT system in 2001 [65]. Since then, the topic has been extensively studied in FZK [50][57][66][67] and today a new experimental 3D system is functional [68]. Because of a conceptual difference in the construction of the 2D and the 3D systems a chapter will be devoted to each separately.

2.2.1 The Karlsruhe 2D USCT system

The 2D system developed in FZK was designed to cover a ring around the imaged object by as many transducers as possible. To keep the system reasonably simple, two moving arms are used. Each of the arms carries an ultrasonic probe with 16 transducers and could be circled around a steel ring with 100 fixed positions. In the first probe group only one of the 16 transducer elements is used for transmitting ultrasonic pulse waves. All 16 elements of the second probe group are used for receiving. The individually received signal, so called A-scan,

is recorded by the receiving element each time the sending element is excited by an electrical pulse.

The whole system scan is made in 100 steps. Each step consists in successively firing the emitter element at one position and changing the receiving probe position around the ring while recording the received A-scans. In the next step, the sending element is moved into the next position and the receiving probe is again circled around the ring. At each step 1600 A-scans are recorded, therefore a full system scan consists in 160,000 A-scans.

The ring has a diameter of 12 cm. Each transducer element is 0.2 mm wide and 10 mm high. The array of the 16 elements has a pitch of 0.25 mm. The center frequency of the ultrasonic pulses 2.5 MHz was chosen as a compromise between large absorption at higher frequencies and lower resolution due to larger wavelength at lower frequencies. To achieve very short pulses, the transducers are strongly damped and transmit broadband pulses. The received 200 μ s long signals are digitized with a sampling rate of 50 MHz and signal quantization of 10 bits.



Figure 2-5: Experimental prototype of the 2D USCT system in Forschungszentrum Karlsruhe. The white tank is filled with water as a coupling medium for the examined object. Two ultrasonic probes are mounted on rotated rings to simulate all emitter and receiver positions. (Taken from [65])

2.2.2 The Karlsruhe 3D USCT system

The 3D USCT system, besides adding a new dimension, was designed to overcome some of the difficulties of the 2D system. Mainly the data acquisition time was overwhelming on the 2D system, because the moving probe arms had to be moved manually and each A-scan was individually recorded by a digital oscilloscope. The 3D system on the other hand handles the acquisition automatically with a PC. There are also many more physical transducer elements, which can simultaneously record A-scans.

2.2.2.1 System architecture

The new 3D ultrasound computer tomography system consists of three parts: a tank containing the sensor system, data acquisition hardware and a computer workstation (Figure 2-6). The tank has a diameter of 18 cm and a height of 15 cm. 48 transducer array systems (TAS) are mounted into the tank walls carrying each 32 receiving and 8 emitting elements (Figure 2-7). The transducer elements can be accessed individually. The resulting cylindrical array is rotated in 6 steps to fill the gaps between the transducers. Thus a fully covered cylindrical array can be emulated, resulting in a total of 9216 receiver and 2304 emitter positions [68].

Because of the rotation, the A-scans can be sent from and received at virtually any position on the cylinder, but not all emitter-receiver position combinations are possible. Still the

total number of A-scans produced by a full system scan is approximately 3.5 million. Although this number is higher than the total number of A-scans in the 2D system, there are less A-scans per a z-layer in the 3D system (as there is only one layer in the 2D system).

The received signals and the control signals are gathered in four blocks containing preamplifiers, address generation and control logic.

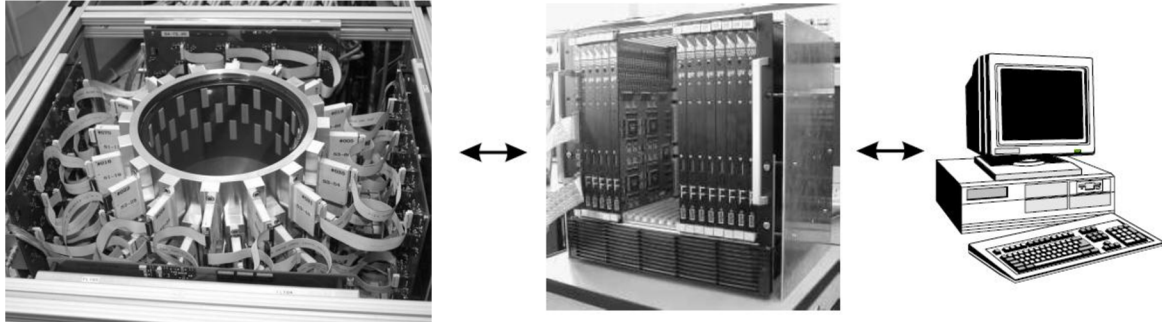


Figure 2-6: Overview of the 3D USCT system in Forschungszentrum Karlsruhe. Left: the cylindrical tank with 48 mounted transducer array systems. Middle: Data acquisition unit with 192 channels. Right: computer system for image reconstruction. (Taken from [69]).

The data acquisition electronics is a modified design of the system for the Auger fluorescence detector [19]. It is based on 9 9HE-card boards connected by a modified VME-bus. One board controls the data acquisition process, the data storage and the transfer to the computer workstation. The other 8 boards are carrying 24 data recording channels each. A channel consists of the analog signal processing, an A/D converter (10 MHz, 12 Bit) and the digital signal processing. The digital processing is based on an array of four FPGAs executing the online data storage, noise reduction and simple data reduction [68].

While one emitting transducer is activated with coded excitation, all receiving transducers receive simultaneously the scattered signals. 192 channels are sampled and recorded in parallel. 48 multiplexing steps are needed to record an A-scan from every receiver. The data is transferred to a computer workstation and the next transducer-emitter is selected. The data storage, the image reconstruction and the visualization of the results are accomplished on the computer workstation [68].

The recorded A-scan signals are sampled at 10MHz and 12bits. A complete scan produces about 20GB of data. Although theoretically it is possible to scan the whole system within a few seconds, it presently takes 10+ hours. This is because each A-scan is a result of averaging about 10 to 50 measurements to gain a higher signal to noise ratio. The measurement also has to be multiplexed in time (only 192 of 1536 receiver element signals are recorded at a time – using all available channels) to allow for the relatively slow process of storing the data on a PC hard drive. In the near future, it is planned to install a new data acquisition unit, which will allow for scan times under 10 minutes.

2.2.2.2 Transducer array systems - TAS

The ultrasonic transducers are grouped into blocks called transducer array systems (TAS). The transducer elements have the mean frequency of about 3 MHz. They are made of a piezzo-ceramics plate, which is structured by a sub-dicing technique [64], to produce an element of 1.4 mm by 1.4 mm. This results in a relatively narrow angular characteristic. The design resulted from a compromise between an ideally omnidirectional characteristic and the need to focus the ultrasonic energy into the center of the USCT tank to get the waves through the examined object.

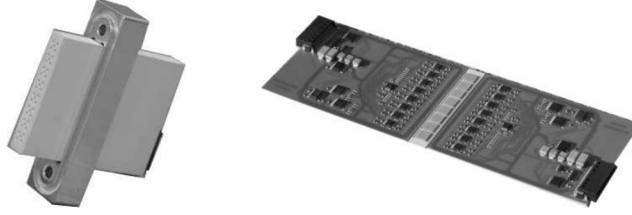


Figure 2-7: The transducer array system (TAS) – folded and sealed (left) and an interior view of an unfolded TAS (right).

The transducer array systems are designed and manufactured in a hybrid laboratory of the FZK. The almost entirely automatic manufacture process guarantees high quality and high reproducibility of the transducer characteristics ($\pm 2\%$) and low costs (~ 100 € per transducer array system including front-end electronics) [68].

The ultrasonic pulses generated by the TASes are controlled by the so called coded excitation pulse – a short electrical signal generated by a D/A converter on the data acquisition boards and programmable by the controlling software. The ultrasonic pulses are therefore controllable in terms of length, frequency, bandwidth, and so on. The power spectrum of the transmitted ultrasonic pulses is of course highly dependent on the transfer functions of the electronics and the ultrasonic transducers.

2.2.3 FZK Reconstruction method (the sum-and-delay algorithm)

The following three imaging modalities are possible using the Karlsruhe USCT: reflectivity imaging, speed of sound imaging, and attenuation imaging. Since the introduction of the 3D system (2004), the group mainly concentrates on the reflectivity imaging, because the transducer array coverage is very sparse and achieves full coverage only by rotating the whole cylinder with both emitter and receiver elements.

The algorithm used by the Karlsruhe team for the reflectivity imaging is a so-called sum-and-delay algorithm [70]. For each point in the image, the amplitude (or some preprocessed version) of the acquired A-scans at the position corresponding to the distance between emitter and receiver, is accumulated

$$f(\vec{x}) = \sum_{j,k} T \left(A_{(j,k)} \left(\frac{a_j + b_k}{c} \right) \right) \quad (2.1)$$

where f denotes the reflectivity image, \vec{x} the coordinates of the reconstructed point, T are pre-processing steps, $A_{(j,k)}$ the A-scan acquired at sending position \vec{x}_j and receiving position \vec{x}_k . c is the speed of sound in water, and a_j and b_k are the distances from the reconstructed point to the emitter and receiver, respectively (also see Figure 1-4). Preprocessing steps T can be also implemented e.g. matched filtering, envelop calculation, deconvolution, etc. Equation (2.1) is valid for constant speed of sound, small attenuation, spherical emittance and Huygens's point scatterers [58].

Using the same assumptions and neglecting noise, the resulting value of each voxel can be given as:

$$f(\vec{x}) = \sum_{j,k} \int_{E_{(i,k)}} R(l) dl = NR(\vec{x}) + \varepsilon_{(I,K)}(\vec{x}) \quad (2.2)$$

where is $R(\vec{x})$ the reflectivity map of the imaged object, $E_{(i,k)}$ is the integral over the surface of the ellipsoid given by the emitter i , the receiver k , and voxel position \vec{x}_k . Then the resulting voxel amplitude $f(\vec{x})$ is the sum of the reflectivity R at \vec{x} magnified by N , the number of applied emitter-receiver combinations, and an error term $\varepsilon_{(I,K)}(\vec{x})$ (I, K indicate the

dependence of ϵ from the geometry and discretization of the aperture). ϵ is the result of multiple scatterers received at the same time instance [58].

To test the imaging capabilities of the 2D system, the team in Karlsruhe built a phantom consisting of several tubes with gelatine, straws, and threads. The smallest structures within the phantom are nylon threads with a diameter of 0.1 mm each, corresponding to approximately 0.2 wavelengths of the emitted ultrasound signal [68].

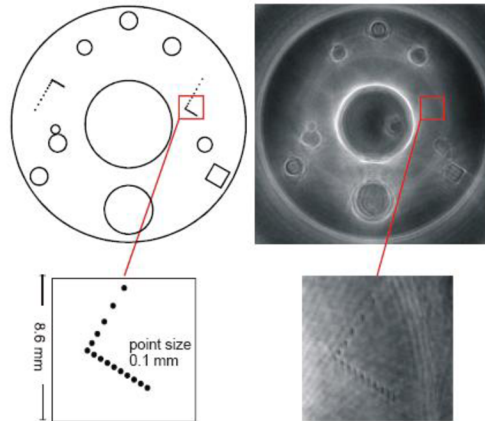


Figure 2-8: Phantom and reconstructed images from Karlsruhe 2D USCT. Left: rough blueprint of the phantom. The smallest structures consist of nylon threads with a diameter of 0.1 mm and a spacing of 0.5 mm. Right: reconstructed cross-section. (Taken from [68])

To mimic the imaging of a real breast, a clinical breast phantom (triple biopsy breast phantom, CIRS, Inc., Norfolk, USA) was imaged with the Karlsruhe 3D USCT system. The phantom contained cancer and cyst mimicking masses of 2 to 10 mm in diameter. For comparison a MR volume of the phantom (1.5T Siemens Magnetom Vision, double breast coil, T1-weighted, 1.37 mm^3 voxel size) was acquired (Figure 2-9, left).

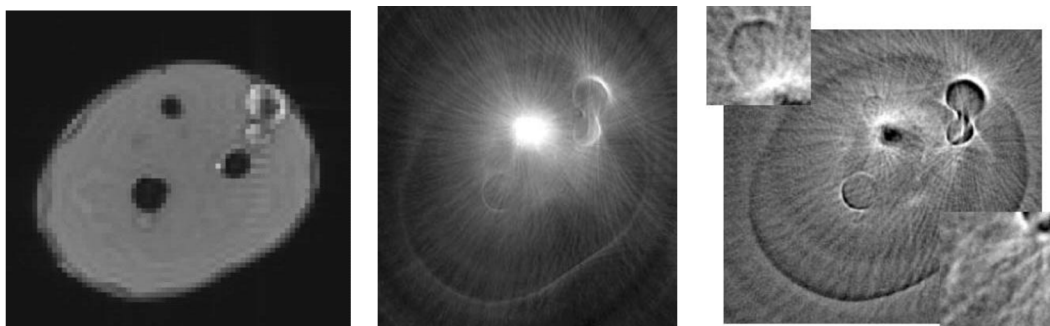


Figure 2-9: Comparison of MRI and Karlsruhe 3D USCT images of a breast phantom. Left: an MR image. Middle: USCT image with artifact reflections from a “cancerous” region with high reflectivity. Right: corrected USCT image with the artifact removed and normalized reflectivity values (the smaller magnifications show the two partly obscured “cysts”). (Taken from [58])

The 3D USCT reflectivity image reconstructions are visible in (Figure 2-9, middle and right). As ultrasound images the tissue borders, the USCT images are expected to be similar to the gradient images of the MRI. The “skin” of the phantom is clearly visible, also one “cyst” (round dark area) and the “cancer” (partly white double circle) structure at the top left is imaged with well defined outlines. A bright blob approximately in the center of the image obscures the other two “cysts”. This artifact is caused by a cluster of strong reflectors (“cancer”)

near the “nipple” of the phantom outside the focal region. For an image based on A-scans where the reflections from this point have been deleted; the bright artifact vanishes and the obscured “cysts” become partly visible.

2.3 Published sensitivity calibration methods

The transducer array elements used in any ultrasonic system can never be manufactured with 100% repeatability and differences in quality are unavoidable. Each transducer can be described with its own radiation pattern – an angle and frequency dependent function describing the emitted pressure field. The transducer to transducer variations in the shape of this function are usually negligible, but the differences in the magnitude of this function can be considerable. If these variations are compensated for, the quality of the reconstructed images can be significantly improved.

Systems with only a small number of ultrasonic transducers can utilize the classical approach of measuring the radiation field using a calibrated hydrophone. The measurement can be done for each element individually yielding a sensitivity parameter or even the whole radiation pattern. The received signals are then multiplied by the corresponding correction factors. Such an approach was used by Andre et.al. in their diffraction tomography system [4].

A different approach to sensitivity calibration was used in the Ring Transducer System for Medical Ultrasound Research (overview of the system can be found in chapter 2.1). The calibration takes advantage of the fact that the individual transducers act as both the emitters and receivers.

The calibration uses a 0.10-mm-diameter metal wire at the approximate center of the ring shaped transducer array, as depicted in Figure 2-10. A single element is used to transmit a pulse and then receive the echo from the wire. This pulse-echo experiment is repeated 10 times for each of the 2048 elements and the repetitions at each element are averaged [73].

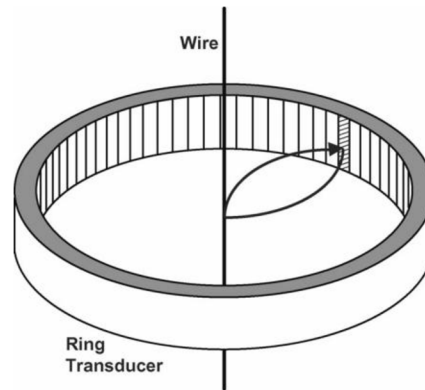


Figure 2-10: Calibration geometry. For calibration, a pulse is transmitted from a single element, and the echo from a wire positioned at the center of the ring is received by the same element. (Taken from [73])

A reference waveform $\bar{s}(t)$, found by averaging all of the time-aligned waveforms, is formed first. The reference waveform is then used with the pulse-echo signal $s_i(t)$, where i is the element number, to compute finite-impulse response compensation filters $r_i(t)$ that match the pulse-echo signal from the wire with the reference waveform. The computation is based on the relation:

$$s_i(t) = e(t) \otimes h_i(t) \otimes h_i(t) \quad (2.3)$$

where $h_i(t)$ is the impulse response of element i , $e(t)$ is the excitation signal applied to the element, and \otimes represents temporal convolution. The relation for the calibration filter $r_i(t)$ applied before transmission and after reception is then defined by:

$$\bar{s}(t) = e(t) \otimes r_i(t) \otimes h_i(t) \otimes h_i(t) \otimes r_i(t) \quad (2.4)$$

in which the pulse-echo response at element i has been set equal to the average signal. Substituting (3) in (4) and solving for the calibration filter at each element yields:

$$R_i(f) = \sqrt{\frac{\bar{S}(f)}{S_i(f)}} \quad (2.5)$$

where all the uppercase symbols denote the temporal Fourier transform. The values of R_i in the system passband are the coefficients of the corresponding finite-impulse-response compensation filter [73].

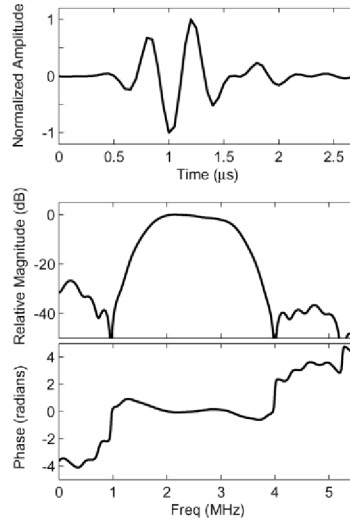


Figure 2-11: Average RF echo waveform (image on top) from a wire target and the corresponding power spectrum (center) and phase (bottom). These are the reference waveform and spectrum used for the computation of the calibration filters. (Taken from [73])

Such an approach elegantly solves not only the scalar sensitivities of individual transducer elements but also gives a temporal compensation filter. On the other hand, the directivity pattern is omitted completely in the calculations and so such a filter is only valid for omnidirectional transducers.

The above described calibration approach shows how an ultrasound system with thousands of transducers can be automatically calibrated without using any additional measuring equipment. Unfortunately, this particular method could not be used in case of the Karlsruhe USCT mainly because of the lack of transducer elements, which are able to both emit and receive.

2.4 Known position calibration methods

The following chapters give an overview of several position calibration techniques, which are used in other technical areas and applications. It is shown and argued why none of these methods are fully suitable for the case of the Karlsruhe USCT position calibration and that therefore a novel method had to be developed.

2.4.1 Global Positioning System (GPS)

The Global Positioning System (GPS), although primarily a military application developed by the US Army, has been promoted for civil uses since the beginning of its development, and has therefore been very well described in numerous scientific and technical publications. The GPS was conceived as a ranging system from known positions of satellites in space to unknown positions on land, at sea, in air and space. The original objectives of the system

were the instantaneous determination of position and velocity and the precise coordination of time. The system consists of three major segments [26]:

- the space segment consisting of satellites orbiting the Earth which broadcast the positioning signals,
- the control segment steering the whole system,
- the user segment including many types of receivers.

Because many aspects, which are dealt with in GPS (satellite orbits, signal encoding, atmospheric effects, relativistic effects, etc.), are not necessary to deal with in the USCT, only the basic mathematical concepts will be discussed here.

Despite the large number of literature sources on GPS the following paragraphs discussing the main concepts are mostly taken from [26] as the author found it as the most comprehensive.

2.4.1.1 Pseudorange equations

The GPS uses pseudoranges (pseudo distances) resulting from receiving and analyzing the broadcast satellite signal. The pseudorange is derived from measuring the travel time of the coded signal from the satellite to the receiver Δt and multiplying it by its velocity c (the speed of light). The clocks of the satellite and the receiver are never perfectly synchronized. Instead of true ranges ρ , pseudoranges R are obtained where the synchronization error $\Delta\delta$ (denoted as clock error) is taken into account (2.6).

$$R_i^j = \rho_i^j + c\Delta\delta_i^j \quad (2.6)$$

where the lower indices refer to the receiver site and the upper indices refer to the satellite number in view of the receiver.

Let us now take a look at the unknowns in equation (2.6). The distance from the satellite to the receiver can be explicitly written as:

$$\rho_i^j = \sqrt{(X^j - X_i)^2 + (Y^j - Y_i)^2 + (Z^j - Z_i)^2} \quad (2.7)$$

where $\{X^j, Y^j, Z^j\}$ is the known position of the satellite (coded in the broadcast signal) and $\{X_i, Y_i, Z_i\}$ is the unknown position of the receiver in given absolute (world) coordinates. The clock error $\Delta\delta_i^j$ is composed of two parts: the unknown bias δ_i of the receiver clock from the universal GPS time and the known bias δ^j of the satellite from the GPS time, which is also encoded in to the broadcast signal.

$$\Delta\delta_i^j = \delta_i - \delta^j \quad (2.8)$$

Consequently each equation (2.6) comprises of four unknowns: the three point coordinates of the receiver unit, and the clock bias. Thus, four of these equations (and therefore four satellites in view of the receiver unit) are always necessary to solve for the four unknowns.

Substituting (2.8) into (2.6) and shifting the satellite clock bias to the left side of the equation yields:

$$R_i^j + c\delta^j = \rho_i^j + c\delta_i, \quad \forall j \quad (2.9)$$

Note that the left side of the equation contains observed or known quantities, while the terms on the right side are unknown.

2.4.1.2 Linearization

Note that the true distance ρ in (2.7) is nonlinear with respect to the unknown position coordinates of the receiver. In order to solve for the unknowns a linearization step is useful.

Let us assume approximate values X_{i0}, Y_{i0}, Z_{i0} for the unknowns, an approximate distance ρ_{i0}^j can be calculated by

$$\rho_{i0}^j = \sqrt{(X^j - X_{i0})^2 + (Y^j - Y_{i0})^2 + (Z^j - Z_{i0})^2} \equiv f(X_{i0}, Y_{i0}, Z_{i0}) \quad (2.10)$$

Using the approximate values, the unknowns X_i, Y_i, Z_i can be decomposed as

$$\begin{aligned} X_i &= X_{i0} + \Delta X_i \\ Y_i &= Y_{i0} + \Delta Y_i \\ Z_i &= Z_{i0} + \Delta Z_i \end{aligned} \quad (2.11)$$

where now $\Delta X_i, \Delta Y_i, \Delta Z_i$ are the new unknowns. This means that the original unknowns have been split into a known part (represented by the approximate values X_{i0}, Y_{i0}, Z_{i0}) and an unknown part (represented by $\Delta X_i, \Delta Y_i, \Delta Z_i$). The advantage of this splitting-up is that the function $f(X_i, Y_i, Z_i)$ is replaced by an equivalent function $f(X_{i0} + \Delta X_i, Y_{i0} + \Delta Y_i, Z_{i0} + \Delta Z_i)$ which can be now expanded into a Taylor series around the approximate point. This leads to

$$\begin{aligned} f(X_i, Y_i, Z_i) &\equiv f(X_{i0} + \Delta X_i, Y_{i0} + \Delta Y_i, Z_{i0} + \Delta Z_i) \\ &= f(X_{i0}, Y_{i0}, Z_{i0}) + \frac{\partial f(X_{i0}, Y_{i0}, Z_{i0})}{\partial X_{i0}} \Delta X_i \\ &\quad + \frac{\partial f(X_{i0}, Y_{i0}, Z_{i0})}{\partial Y_{i0}} \Delta Y_i + \frac{\partial f(X_{i0}, Y_{i0}, Z_{i0})}{\partial Z_{i0}} \Delta Z_i + \dots \end{aligned} \quad (2.12)$$

where the expansion can be truncated after the linear term thanks to the closeness of the estimate point to the exact position; otherwise the unknowns would appear in nonlinear form again. The partial derivatives are obtained from (2.10) by

$$\begin{aligned} \frac{\partial f(X_{i0}, Y_{i0}, Z_{i0})}{\partial X_{i0}} &= -\frac{X^j - X_{i0}}{\rho_{i0}^j} \\ \frac{\partial f(X_{i0}, Y_{i0}, Z_{i0})}{\partial Y_{i0}} &= -\frac{Y^j - Y_{i0}}{\rho_{i0}^j} \\ \frac{\partial f(X_{i0}, Y_{i0}, Z_{i0})}{\partial Z_{i0}} &= -\frac{Z^j - Z_{i0}}{\rho_{i0}^j} \end{aligned} \quad (2.13)$$

and are the components of the unit vector pointing from the satellite towards the approximate site. The substitution of equations (2.10) and (2.13) into (2.12) gives

$$\rho_i^j = \rho_{i0}^j - \frac{X^j - X_{i0}}{\rho_{i0}^j} \Delta X_i - \frac{Y^j - Y_{i0}}{\rho_{i0}^j} \Delta Y_i - \frac{Z^j - Z_{i0}}{\rho_{i0}^j} \Delta Z_i \quad (2.14)$$

where the equivalence of $f(X_i, Y_i, Z_i)$ with ρ_i^j has been used. This equation is now linear with respect to the unknowns $\Delta X_i, \Delta Y_i, \Delta Z_i$.

2.4.1.3 Solving the system of equations

Substituting equation (2.12) into (2.9) yields a linearized pseudorange equation with known values on the left and unknown on the right

$$R_i^j - \rho_{i0}^j + c\delta^j = -\frac{X^j - X_{i0}}{\rho_{i0}^j} \Delta X_i - \frac{Y^j - Y_{i0}}{\rho_{i0}^j} \Delta Y_i - \frac{Z^j - Z_{i0}}{\rho_{i0}^j} \Delta Z_i + c\delta_i \quad (2.15)$$

Because four variables are unknown, four equations have to be set up to have the solution determined. The shorthand notations

$$\begin{aligned}
l^j &= R_i^j - \rho_{i0}^j + c\delta^j \\
a_{X_i}^j &= -\frac{X^j - X_{i0}}{\rho_{i0}^j} \\
a_{Y_i}^j &= -\frac{Y^j - Y_{i0}}{\rho_{i0}^j} \\
a_{Z_i}^j &= -\frac{Z^j - Z_{i0}}{\rho_{i0}^j}
\end{aligned} \tag{2.16}$$

help to simplify the representation of the system of equations. Assuming now four satellites numbered from 1 to 4, then

$$\begin{aligned}
l^1 &= a_{X_i}^1 \Delta X_i + a_{Y_i}^1 \Delta Y_i + a_{Z_i}^1 \Delta Z_i + c\delta_i \\
l^2 &= a_{X_i}^2 \Delta X_i + a_{Y_i}^2 \Delta Y_i + a_{Z_i}^2 \Delta Z_i + c\delta_i \\
l^3 &= a_{X_i}^3 \Delta X_i + a_{Y_i}^3 \Delta Y_i + a_{Z_i}^3 \Delta Z_i + c\delta_i \\
l^4 &= a_{X_i}^4 \Delta X_i + a_{Y_i}^4 \Delta Y_i + a_{Z_i}^4 \Delta Z_i + c\delta_i
\end{aligned} \tag{2.17}$$

is the appropriate system of equations. Note that the superscripts are the satellite numbers and not exponents! Introducing

$$\mathbf{A} = \begin{bmatrix} a_{X_i}^1 & a_{Y_i}^1 & a_{Z_i}^1 & c \\ a_{X_i}^2 & a_{Y_i}^2 & a_{Z_i}^2 & c \\ a_{X_i}^3 & a_{Y_i}^3 & a_{Z_i}^3 & c \\ a_{X_i}^4 & a_{Y_i}^4 & a_{Z_i}^4 & c \end{bmatrix} \quad \mathbf{x} = \begin{bmatrix} \Delta X_i \\ \Delta Y_i \\ \Delta Z_i \\ \delta_i \end{bmatrix} \quad \mathbf{l} = \begin{bmatrix} l^1 \\ l^2 \\ l^3 \\ l^4 \end{bmatrix} \tag{2.18}$$

the set of linear equations can be written in the matrix-vector notation

$$\mathbf{l} = \mathbf{A}\mathbf{x} \tag{2.19}$$

For this first example of a linearized GPS model, the re-substitution of the vector \mathbf{l} and the matrix \mathbf{A} using (2.16) is given explicitly by:

$$\mathbf{l} = \begin{bmatrix} R_i^1 - \rho_{i0}^1 + c\delta^1 \\ R_i^2 - \rho_{i0}^2 + c\delta^2 \\ R_i^3 - \rho_{i0}^3 + c\delta^3 \\ R_i^4 - \rho_{i0}^4 + c\delta^4 \end{bmatrix}$$

$$\mathbf{A} = \begin{bmatrix} -\frac{X^1 - X_{i0}}{\rho_{i0}^1} & -\frac{Y^1 - Y_{i0}}{\rho_{i0}^1} & -\frac{Z^1 - Z_{i0}}{\rho_{i0}^1} & c \\ -\frac{X^2 - X_{i0}}{\rho_{i0}^2} & -\frac{Y^2 - Y_{i0}}{\rho_{i0}^2} & -\frac{Z^2 - Z_{i0}}{\rho_{i0}^2} & c \\ -\frac{X^3 - X_{i0}}{\rho_{i0}^3} & -\frac{Y^3 - Y_{i0}}{\rho_{i0}^3} & -\frac{Z^3 - Z_{i0}}{\rho_{i0}^3} & c \\ -\frac{X^4 - X_{i0}}{\rho_{i0}^4} & -\frac{Y^4 - Y_{i0}}{\rho_{i0}^4} & -\frac{Z^4 - Z_{i0}}{\rho_{i0}^4} & c \end{bmatrix} \tag{2.20}$$

The coordinate differences ΔX_i , ΔY_i , ΔZ_i and the receiver clock error δ_i result from the linear system (2.19)

$$\mathbf{x} = (\mathbf{A}^T \mathbf{A})^{-1} \mathbf{A}^T \mathbf{l} \tag{2.21}$$

(here the pseudoinverse LMS solution is used, so that the matrix \mathbf{A} doesn't have to be square as in the case, when more than four satellites are observable from the receiver site)

The desired point coordinates X_i, Y_i, Z_i are then finally obtained by updating the coordinate estimates with the calculated error values (2.11).

Although it is not usually stressed enough in the GPS literature, one or more linearize-solve-update iteration steps may be needed to reach the desired position accuracy. Note that the above iterative approach is actually an implementation of the Gauss-Newton method [56] to solve the original nonlinear equation system.

First, a vector of estimate values X_{i0}, Y_{i0}, Z_{i0} is set up. Then, from the nonlinear set of equations (2.9), a Jacobian matrix \mathbf{A} is computed. The next step comprises of solving the linearized equation set (2.19). And finally the vector of estimates is updated by the solved vector of error values (2.11). These steps can be iterated until the root-mean-square of the solved error vector falls below a predetermined threshold.

2.4.1.4 Dilution of Precision (DOP)

An important factor in achieving high quality positioning results with GPS (and any other positioning system) is a low dilution of precision (DOP). The DOP is a measure of the relative geometry of the visible satellites and greatly affects the resulting position uncertainty.

A simple example shows the effect of the geometry of two transmitters in a basic 2D positioning system (Figure 2-12). In a) the transmitters form nearly a right angle with respect to the receiver, and the uncertainty of the distance measurements (indicated by the patterned areas) results in a small position uncertainty (low dilution-of-precision). In b) the transmitters form a sharp angle and the position uncertainty of the receiver is considerably larger (high dilution-of-precision).

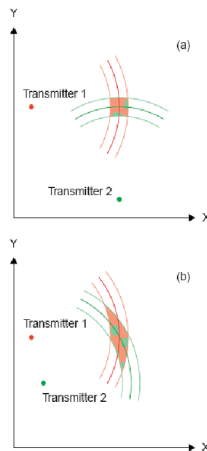


Figure 2-12: DOP in a basic positioning system (taken from [37]).

If we look at how the receiver position is obtained from the measured pseudoranges, we can see that the vector of estimate-error terms x in (2.19) has to be solved by pseudo-inverting the system matrix \mathbf{A}

$$x = (\mathbf{A}^T \mathbf{A})^{-1} \mathbf{A}^T l \quad (2.22)$$

It is assumed that all pseudorange measurements are equally uncertain and that no correlations exist between the errors. Otherwise a more general form can be used:

$$x = (\mathbf{A}^T \mathbf{W} \mathbf{A})^{-1} \mathbf{A}^T \mathbf{W} l \quad (2.23)$$

where \mathbf{W} is a weight matrix reflecting the differences in errors of the measurements and the correlations among them.

This weight matrix is also equal to $\sigma_0^2 C_{\Delta P_C}^{-1}$, in which $C_{\Delta P_C}$ is a covariance matrix of the pseudorange errors and σ_0^2 is known as the prior variance of the unit length. In general, the solution of a nonlinear problem must be achieved by iteration to obtain the result. However, if

the linearization point is sufficiently close to the true solution, then only one iteration is required [37].

If we are asking how accurate can the position and time-delay parameters be calculated for a GPS receiver, we are actually asking how do the pseudorange measurements and model errors affect the estimated parameters in (2.23)? This is given by the covariance law:

$$\mathbf{C}_{\Delta x} = [(\mathbf{A}^T \mathbf{W} \mathbf{A})^{-1} \mathbf{A}^T \mathbf{W}] \mathbf{C}_{\Delta PC} [(\mathbf{A}^T \mathbf{W} \mathbf{A})^{-1} \mathbf{A}^T \mathbf{W}]^T = (\mathbf{A}^T \mathbf{C}_{\Delta PC}^{-1} \mathbf{A})^{-1} \quad (2.24)$$

in which $\mathbf{C}_{\Delta x}$ is the covariance matrix of the parameter estimates.

If we now assume that the measurement and model errors are Gaussian and with the same standard deviation σ for all observations, and that they are uncorrelated, then $\mathbf{C}_{\Delta PC} = \mathbf{I}\sigma^2$, where \mathbf{I} is the identity matrix. In this case equation (2.24) simplifies to:

$$\mathbf{C}_{\Delta x} = (\mathbf{A}^T \mathbf{A})^{-1} \sigma^2 = \mathbf{D}\sigma^2 \quad (2.25)$$

With a value for σ , we can compute the components of $\mathbf{C}_{\Delta x}$ using the above equation. We then can get the measure of the overall quality of the least-squares solution by taking the square root of the sum of the parameter estimate variances:

$$\sigma_G = \sqrt{\sigma_E^2 + \sigma_N^2 + \sigma_U^2 + \sigma_T^2} = \sigma \sqrt{D_{11} + D_{22} + D_{33} + D_{44}} \quad (2.26)$$

in which σ_E^2 , σ_N^2 , and σ_U^2 are the variances of east, north, and up components of the receiver position estimate, and σ_T^2 is the variance of the receiver clock offset estimate.

The above is an estimate of the solution accuracy. It is dependent on the measurement and model error standard deviation (σ) on one hand, and the square-root of the trace of matrix \mathbf{D} on the other. The scaling factor formed from the components of matrix \mathbf{D} is only dependent on the satellite geometry. It is usually greater than one and thus it amplifies the pseudorange error, or dilutes the precision, of the position determination. This scaling factor is therefore usually called the geometrical dilution of precision:

$$\text{DOP} = \sqrt{\text{trace}(\mathbf{D})} \quad (2.27)$$

2.4.1.5 The use of GPS principles in USCT

This chapter covered the principles of the GPS positioning method. As it is, the GPS method cannot be used for anything else than for what it was designed: navigation. The importance for the use in USCT lies in the fact that it is possible to obtain positions of the receiver only by observing the time-of-flight of the signals travelling from the orbiting satellites to the receiver. Also the mathematical apparatus of the dilution of precision proved useful in the novel USCT positioning method, where the author used it to optimize the anchoring (boundary conditions) of the system of equations.

2.4.2 A published GPS modification for an ultrasonic systems

In [41], Yue Li proposed a novel calibration method based on the principles of the GPS positioning. The author needed to calibrate the positions of ultrasonic transducers, which formed a large underwater imaging system. The ultrasonic receivers substituted GPS receivers, and a high-precision positioning device with a hydrophone replaced the GPS satellites. The method was also extended to include the calibration of the speed of sound of the water in which the imaging system was submerged.

The imaging system comprises one powerful ultrasonic transmitter element, which sends ultrasonic waves through a large sparse receiver array. The ultrasonic waves are reflected from the imaged target back towards the receiver array, where the signals are recorded and are sent to a processor for further processing and image forming.

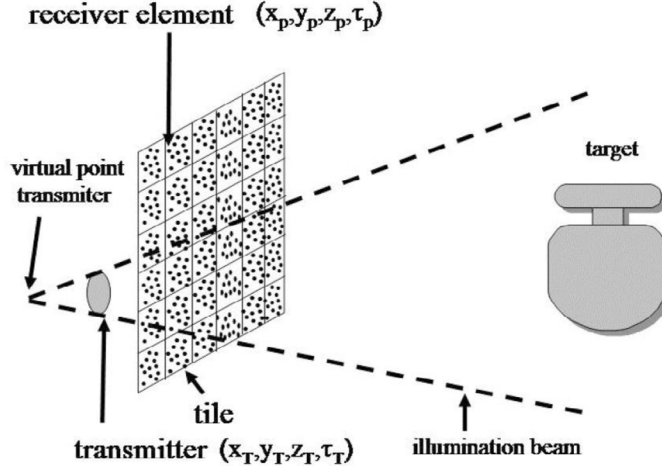


Figure 2-13: The underwater imaging system with a sparse receiver array (taken from [41]).

To achieve the desired imaging resolution of 1mm at the distance of 1m, and with a 3MHz center frequency, the receiving aperture needs to be at least 0.5m x 0.5m. It would of course be impractical to build a full array of this size. The authors decided to build an array with tiles (10 by 10) with smaller sparse sub arrays (0.05m x 0.05m). Each tile contains 32 randomly distributed receiving elements. In the array, there is a total of 3200 elements.

The tiled construction of smaller sparse sub arrays is on one hand practical and efficient, on the other hand it brings difficulties in precise positioning of the receiving transducers which than greatly affects the image quality.

The author developed a method in which the individual receiver elements are calibrated in the same manner as if they were GPS receivers. A high-precision positioning scanner with a hydrophone attached is used to emulate the role of the GPS satellites in view of the receiver. The hydrophone is used to emit ultrasonic pulse waves, which are intercepted by the receivers.

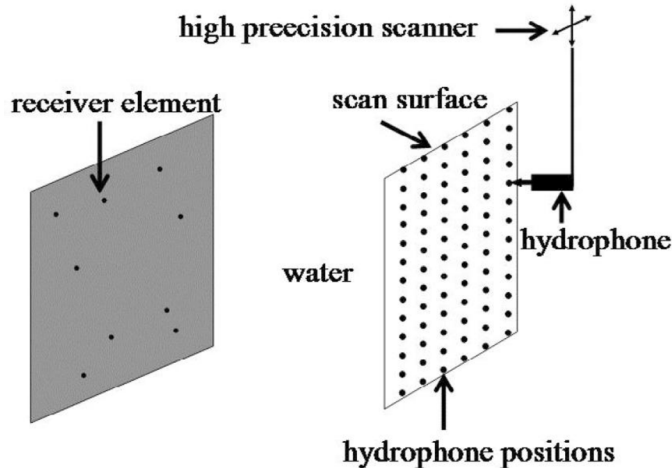


Figure 2-14: Set up for the calibration method with a high/precision hydrophone scanner (taken from [41]).

2.4.2.1 The calibration method

If we consider the case, where there are N_h hydrophone positions, N_e number of elements, then the measured time-of-flight τ_e^h from hydrophone position h to element e can be expressed as:

$$\tau_e^h = t_e^h + \tau_e + \tau^h + d\tau_e^h \quad (2.28)$$

where t_e^h is the actual time-of-flight, τ_e and τ^h are the receiver element and hydrophone time-delays respectively (including the transmission and reception channel delays), and $d\tau_e^h$ is a

Gaussian zero-mean measurement noise. It is assumed that τ_e and t^h are independent of transmission and reception angle. Because the same hydrophone is used for all measurements, t^h is the same for all hydrophone positions.

Equation (2.28) is analogical to the pseudorange equation (2.6). The receiver and hydrophone time-delay components take the place of the clock-error component. The main difference is that (2.28) is expressed in the time-domain, whereas (2.6) is in the spatial domain. The relation between the two is simply the speed of propagation of the waves. Unlike in GPS where the speed of propagation can be assumed constant in all cases (the speed of light), in the underwater imaging application it is an unknown, because the speed of sound differs with temperature (and eventually salinity). That is why the author of this method extended the GPS approach to handle the speed of sound as one of the unknowns.

Equation (2.28) can be formulated for each combination of hydrophone position and receiver element number. A system of these equations can be therefore set up and the unknown positions and time-delays can be solved for. Because the actual time-of-flight t_e^h in equation (2.28) is nonlinear, a linearization step is useful, similarly as it is done in the GPS approach.

As an initial step, position estimates of the receiving elements (x_{e0}, y_{e0}, z_{e0}) and the speed of sound estimate v_0 are chosen, where the actual values are ($x_e=x_{e0}+\Delta x_e, y_e=y_{e0}+\Delta y_e, z_e=z_{e0}+\Delta z_e$) and ($v=v_0+dv$) respectively. Then the term t_e^h in equation (2.28) can be linearized as follows:

$$\begin{aligned} t_e^h &= \frac{r_e^h}{v} = \frac{1}{v} \sqrt{(x_e - x^h)^2 + (y_e - y^h)^2 + (z_e - z^h)^2} \\ &= \frac{1}{v_0 + dv} \sqrt{(x_{e0} + \Delta x_e - x^h)^2 + (y_{e0} + \Delta y_e - y^h)^2 + (z_{e0} + \Delta z_e - z^h)^2} \\ &\approx \frac{r_{e0}^h}{v_0} + \frac{x_{e0} - x^h}{v_0 r_{e0}^h} \Delta x_e + \frac{y_{e0} - y^h}{v_0 r_{e0}^h} \Delta y_e + \frac{z_{e0} - z^h}{v_0 r_{e0}^h} \Delta z_e + \frac{r_{e0}^h}{v_0^2} dv \end{aligned} \quad (2.29)$$

where ($\Delta x_e, \Delta y_e, \Delta z_e$) are the receiver element coordinate error terms, dv is the speed of sound error term, and

$$r_{e0}^h = \sqrt{(x_{e0} - x^h)^2 + (y_{e0} - y^h)^2 + (z_{e0} - z^h)^2} \quad (2.30)$$

is the test distance.

The linearized equation set is obtained by expressing the difference between the measured time-of-flight value and the test time-of-flight value:

$$\Delta t_e^h = \tau_e^h - \left(\frac{r_{e0}^h}{v_0} + \tau_{e0}^h \right) = \frac{x_{e0} - x^h}{v_0 r_{e0}^h} \Delta x_e + \frac{y_{e0} - y^h}{v_0 r_{e0}^h} \Delta y_e + \frac{z_{e0} - z^h}{v_0 r_{e0}^h} \Delta z_e + \frac{r_{e0}^h}{v_0^2} dv + \Delta \tau_e \quad (2.31)$$

$h = 1, 2, 3, \dots, N_h, \quad e = 1, 2, 3, \dots, N_e$

where τ_{e0} is the time-delay test value for element e , and $\Delta \tau_e = \tau_e - \tau_{e0}$.

By solving the above equation set, a set of position, time-delay, and speed of sound error values are obtained. These can be used to update the previous estimates and the whole process can be iterated until the desired accuracy is reached.

This calibration method was perhaps the most inspiring for the author and showed the possibilities of using an established method like GPS being used in a very different environment. Along with the original GPS, it served as a basis for the novel USCT positioning method. The method itself cannot be used for the purposes of the USCT because it makes use of the ‘‘high precision scanner’’ moving the hydrophone to known positions. These known position values are then used in the equation set (2.31) to calculate the unknown positions of the

receiving transducer elements. In USCT however, both the emitting and receiving transducers lie at unknown positions and need to be calibrated.

2.4.3 The RTS calibration approach

This calibration approach was developed by Waag and Fedwa for the Ring Transducer System for Medical Ultrasound Research [73] (overview can be found in chapter 2.1). The method takes advantage of the fact that the transducer elements can be used both as an emitter and a receiver. The calibration is also used to determine the sensitivity of individual elements, and so the main concept of data acquisition has already been described in chapter 2.3.

A time-shift correction for each element is determined by cross correlation of each recorded waveform with a reference waveform $\bar{s}(t)$ (2.4) found by averaging all of the time-aligned waveforms within the range of acceptable sensitivity. Before this step a sinusoidal time-shift bias, caused by the fact that the metal wire is not positioned exactly in the middle of the ring transducer, has to be removed.

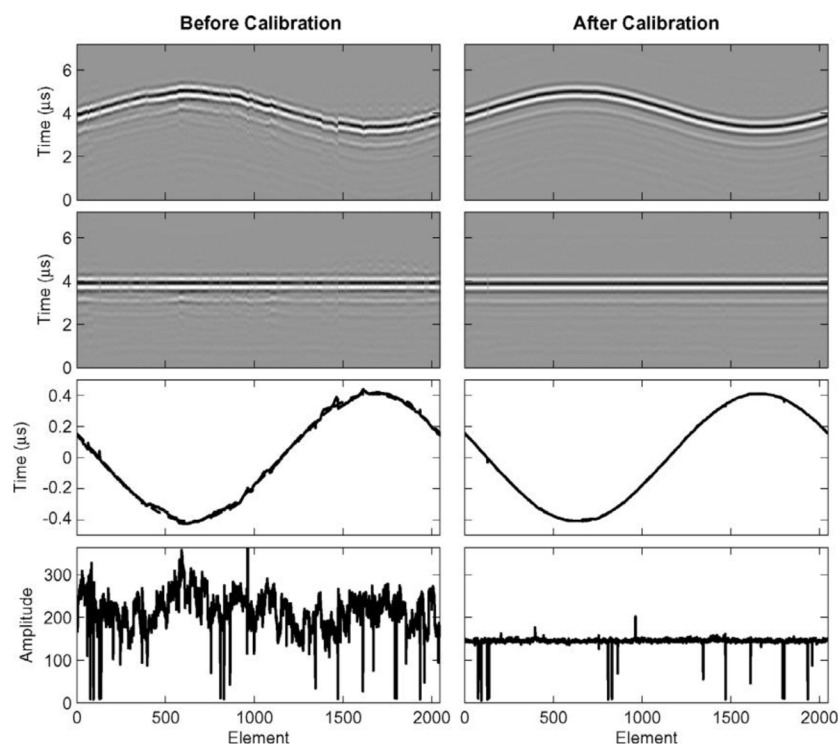


Figure 2-15: Pulse-echo data before and after calibration. In the plotted data, 13 elements tested low and three elements tested high. The grayscale is linear. (Taken from [73])

Although it is very elegant and lightweight, this method completely omits the geometrical calibration and only deals with time-delays. The authors assume that the elements on the ring transducer array form a perfect circle. Positioning deviations may actually be partially compensated for by this technique but the calibration results would only be valid for signals coming from the area around the calibration wire.

The second and more important reason why not to use this calibration technique for the USCT system in Karlsruhe is the fact that each transducer element must provide the functionality to both send and receive. This is not the case in the current Karlsruhe USCT.

2.4.4 Multidimensional scaling

Multidimensional scaling (MDS) is a field of study concerned with embedding a set of points in a low-dimensional space so that the distances between the points resemble as closely

as possible a given set of dissimilarities between objects that the points represent [14]. It has been popularly used to analyze experimental data in physical, biological, and behavioral sciences.

Metric multidimensional scaling (MDS) transforms a distance matrix into a set of coordinates such that the (Euclidean) distances derived from these coordinates approximate as well as possible the original distances. The basic idea of MDS is to transform the distance matrix into a cross-product matrix and then to find its eigen-decomposition which gives a principal component analysis (PCA). Like PCA, MDS can be used with supplementary or illustrative elements, which are projected onto the dimensions after they have been computed [24].

As an example, Figure 2-16 shows a map of the United States computed from the driving distances between major cities published in a road atlas, using MDS. Even though the driving distance between two cities is a poor approximation to their actual distance, the resulting map is accurate [7].

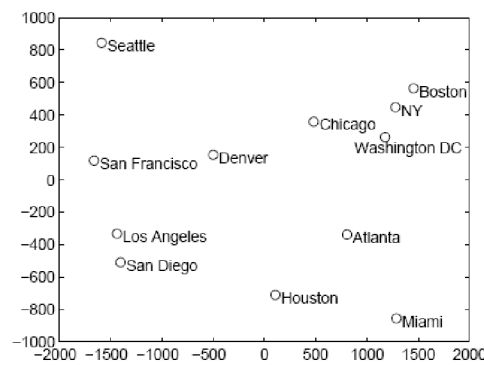


Figure 2-16: A map of cities in USA, built by taking the driving distances from a road atlas and applying the MDS algorithm to it. (Taken from [7])

The algorithm is as follows: we first form a square distance matrix \mathbf{D} , with the elements $d_{i,j}$ being the squares of distance between the i -th and j -th node,

$$d_{i,j} = \delta^2_{ij} = (\vec{x}_i - \vec{x}_j)^T (\vec{x}_i - \vec{x}_j) \quad (2.32)$$

We then can compute the inner product matrix \mathbf{B} :

$$\mathbf{B} = -\frac{1}{2} \mathbf{J} \mathbf{D} \mathbf{J} \quad (2.33)$$

$$\mathbf{J} = \mathbf{I} - \frac{1}{n} \mathbf{E}$$

where \mathbf{I} is the unit matrix, \mathbf{E} is the matrix of all ones, and n is the number of the nodes. Now $\mathbf{B} = \mathbf{X} \mathbf{X}^T$, and because \mathbf{B} is symmetric positive semi-definite it can be decomposed into $\mathbf{B} = \mathbf{V} \mathbf{L} \mathbf{V}^T$, where \mathbf{L} is the diagonal matrix of eigenvalues. We then can compute the matrix of coordinates $\mathbf{X} = \mathbf{V} \mathbf{L}^{1/2}$.

The advantage of this method is that it yields a unique solution, where the geometrical axes are set so that the variation of the transducers' positions is biggest along the first dimension, the second biggest variation is in the second dimension, and so on. We may then translate and rotate the coordinate system to the desired origin and orientation.

This technique could be used to calibrate (find) the positions of transducers in an ultrasound computed tomography system. The distances between the transducers could be computed from the time-of-flight of the ultrasonic signals.

The main problem, when applying this technique for position calibration is usually missing data. In order to run the algorithm, the matrix of distances \mathbf{D} has to be entirely filled.

In the case of the USCT in Forschungszentrum Karlsruhe, the ultrasonic transducer elements are hardwired to operate either as emitters or receivers. They cannot change the operation mode. Thus, the emitter-to-emitter and receiver-to-receiver distances are never recorded.

The problem of missing data is a common issue in different technical areas where the MDS algorithm is being used. It has been successfully solved in areas of molecular design using the formalism of distance geometry [1][38][71]. Unfortunately, the molecular design problems are very different in nature from the USCT problem in that only a certain combination of atom constellations are possible to form a molecule. This limitation is exploited in the matrix completion problem. Using a combinatorial approach, all physically impossible constellations are avoided, and only the few feasible constellations yield the missing distances among atoms.

A different approach to the matrix completion problem was developed for an application in the microphone array calibration field [7][9]. This method requires building a basis of nodes (microphones), where all inter-node distances can be measured. The number of nodes has to be at least $p+1$, where p is the number of dimensions of the resulting space (usually $p = 3$). All other nodes only require having distance measurements available to all of the basis nodes. Other missing distances can be calculated.

Unfortunately this approach also cannot be used for the case of the Karlsruhe USCT, because the required basis of at least 4 nodes (transducers) cannot be formed (we are not able to obtain the emitter-emitter and receiver-receiver distances from the time-of-flight of the ultrasonic signals).

2.4.5 Localization methods in wireless networks

Wireless sensor networks got a lot of attention in the past few years. They hold the promise of new applications in the area of monitoring and control like target tracking, intrusion detection, wildlife habitat monitoring, climate control, and others. Among other problems to be solved in this area of study, the localization of the autonomous nodes (self-organization) is an active area of research [11][39][50].

Although many approaches have been developed, in principle they always try to take advantage of having an infrastructure of so-called beacon or anchor nodes with known locations (and possibly stronger signals) and computing the locations of other nodes relative to these beacon nodes. In some approaches a few nodes are chosen as the anchors in the first phase of the self-localization. Their position is calculated (using Multidimensional scaling or a GPS-like algorithm) relative to other anchors and a base coordinate system is established. The rest of the nodes calculate their own position relative to this coordinate system using only the communication with the anchor nodes.

Compared to other applications, the localization methods used in wireless networks have to satisfy requirements on energy efficiency (little computation and communication) and on the other hand do not require such a high accuracy.

The main premise of these methods is that the nodes are able to communicate between each other and therefore have both the sending and receiving capability. Moreover the nodes are able to broadcast coded messages with their location. This is not the case in the USCT and therefore these methods are not suitable for the USCT calibration.

3 Aims of the dissertation

The field of ultrasonic computed tomography has been explored by various groups of scientists for several decades now. Nevertheless, none of these groups has been able to build a fully functional system, which is able to produce repeatable images in non-laboratory conditions, which is fast enough for real hospital environment, and which is able to deliver high-contrast and high-resolution images usable in practice.

The author had the opportunity to be involved in the Karlsruhe USCT project (described in detail in chapter 2.2). Also this project presents several unsolved problems. As the title of the dissertation suggests, the primary aim of this dissertation is to *develop new calibration methods* for an ultrasonic tomography system. The author intends to contribute to the following areas:

1. **Reconstruction of attenuation images** – although the attenuation image reconstruction is quite a broad area (and not specifically linked with the main topic - calibration), the intention is to use this area as a starting point, get practical experience with the project, and explore the possibilities of improving existing attenuation reconstruction methods developed by project colleagues. The individual goals are:
 - a. Get accustomed with the used hardware, software, and methods
 - b. Make measurements on both the 2D and 3D USCT systems in Karlsruhe using custom-built ultrasonic phantoms
 - c. Improve the existing methods of attenuation reconstruction
2. **Sensitivity calibration** – the currently used image reconstruction methods do not account for sensitivity and directivity differences of the ultrasonic transducers. It is suspected, that the variations in sensitivity may have a big impact on the quality of the reconstructed images. The intention is to create a method for an easy and repeatable calculation of the sensitivity parameters of the Karlsruhe USCT transducers, which could then be used (by other team members) in the existing reconstruction algorithms to compensate for the variations. An “empty measurement” (full scan of the system with only water inside the USCT tank) should be used as the source data for the method. The individual goals are:
 - a. Formulate a sensitivity calibration method which would suite the Karlsruhe USCT system and implement it in Matlab programming environment
 - b. Make appropriate calibration scans using the Karlsruhe USCT system
 - c. Use the sensitivity calibration method on the measured data.
 - d. Make a comparison sensitivity measurement of the Karlsruhe USCT transducer elements using an independent hydrophone
3. **Geometrical calibration** – also in this area it is suspected that minor variations of positions and orientations of the transducers from the assumed geometry considerably degrade the quality of the reconstructed images. Because this is a substantial problem in the Karlsruhe USCT project, the geometrical calibration area will get the *biggest attention* during this dissertation project. The intention is to create a method for calculating the positions and orientations of the ultrasonic transducers. As with the sensitivity calibration, an empty measurement should be used as a source of data for the calibration. The calculated geometrical parameters should then be used (by other team members) in the existing image reconstruction methods. The individual goals are:
 - a. Define a geometrical calibration method suited for the Karlsruhe USCT system and implement it in Matlab programming environment
 - b. Test the method on simulated data
 - c. Make appropriate calibration scans using the Karlsruhe USCT system
 - d. Use the geometrical calibration method on the measured data

4 A Contribution to attenuation image reconstruction

This chapter describes the authors work on the reconstruction techniques of attenuation images. The initial study on reconstructing attenuation images from the real Karlsruhe USCT data using conventional X-ray computed tomography (XCT) methods was published on several local conferences [77][78][79]. A modification of the “rebinning” process is described so that the conventional XCT methods may be applicable to the USCT geometry. An improving modification to a novel reconstruction technique utilizing direct and reflected signals was published on an international conference in Umea, Sweden [80].

4.1 Attenuation coefficient calculation

Ultrasonic attenuation parameters of human tissue are closely related to their type and pathological state [65]. Estimation of these parameters can be therefore used for tissue characterization (i.e. discrimination between benign and malignant structures).

To calculate the attenuation of ultrasonic signals in the Karlsruhe USCT (see chapter 2.2) two sets of data have to be obtained. First, the whole system scan is made with only water inside the USCT tank as a coupling medium. This yields a reference data set of ultrasonic signals only slightly attenuated along the water path from the emitter to the receiver. Second, another system scan is made with the imaged object placed inside the USCT tank. This yields the data set of attenuated signals.

Techniques for estimation of ultrasonic attenuation coefficients have been published in numerous publications e.g. [6], [32], [63]. In principle, there are two approaches applicable to broadband ultrasonic signals: the energy ratio method and the method of log-spectral differences.

In the energy ratio method, the estimated attenuation parameter β is simply defined as

$$\beta = \frac{1}{2} \ln(E_0/E) \quad (4.1)$$

where E_0 is the energy of a signal from the empty measurement set, E is the energy of a signal measured with the object in the USCT tank. This method doesn't take the frequency dependency of the attenuation in to account. In case of a broad band ultrasonic pulse emitted in to a medium, the higher frequency components are attenuated more than the lower frequency components. Thus the attenuation will be underestimated by using this method [63].

The second method, on the other hand, utilizes the frequency shift of the attenuated ultrasonic signal towards the lower frequencies. The power spectrum $P(f)$ of an attenuated signal is:

$$P(f) \cong \left(\prod_m T_m \right)^2 P_0(f) e^{-2\beta(f)} \quad (4.2)$$

where T_m are the transmission coefficients at the interfaces of different mediums (i.e. tissue-water interface), P_0 is the power spectrum of the empty measurement signal, and the exponential part contains the frequency dependant attenuation parameter β . Taking the logarithm of this expression yields:

$$2\beta(f) + b = \ln P_0(f) - \ln P(f) \quad (4.3)$$

where $b = \ln(\prod_m T_m)^2$. The attenuation $\beta(f)$ can be modeled as a function, linearly depending on frequency: $\beta(f) = \alpha_0 |f|$. Equation (4.3) actually states that by subtracting the logarithms of the power spectra, a linear function of frequency is obtained. The attenuation α_0 (the slope of this function) can be then computed by a simple linear fitting.

4.2 The straight beam reconstruction

An image can be reconstructed from the computed attenuation parameters described in the previous chapter. For the initial study, the author chose to implement the backprojection algorithm [35] used mainly in X-ray computed tomography.

The backprojection algorithm assumes data collection along so-called projections. Each projection is a collection of parallel ray-integrals – integrals of the imaged parameter along a thin straight line $P_\nu(t_0) = \int_l f(x, y) dl$ (Figure 4-1). In order to be able to reconstruct the image, a set of projections has to be made (varying the angle ν). The reconstruction itself can be realized by “smearing” the calculated ray integrals along their paths back into the image. The mathematical derivation of this method [35] reveals the necessity to filter the projections before the reconstruction by a ramp filter $F(\omega) = |\omega|$ - a high pass filter. The method is therefore sometimes referred to as the filtered back projection.

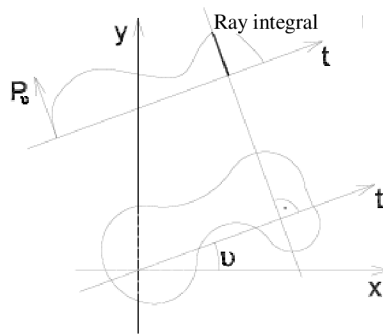


Figure 4-1: Projection and the ray integral.

The filtered back projection can be realized in the original or the spectral domain. It makes use of the slice theorem, which reveals the relationship between the original 2D image and the set of 1D projection spectra: the spectrum of the projection is equivalent to the slice of the 2D spectrum of the original image, which runs through the spectrum center (0,0) at the angle ν [29]. The reconstruction directly in the spectrum domain is rarely used because of the need of interpolation, which is a source of artifacts when using noisy data. More often the reconstruction is realized using the following relation:

$$f(x, y) = \int_0^\pi q_\nu(t) d\nu = \int_0^\pi q(x \cos(\nu) + y \sin(\nu), \nu) d\nu \quad (4.4)$$

where q is the projection spectrum already filtered by the mentioned ramp filter.

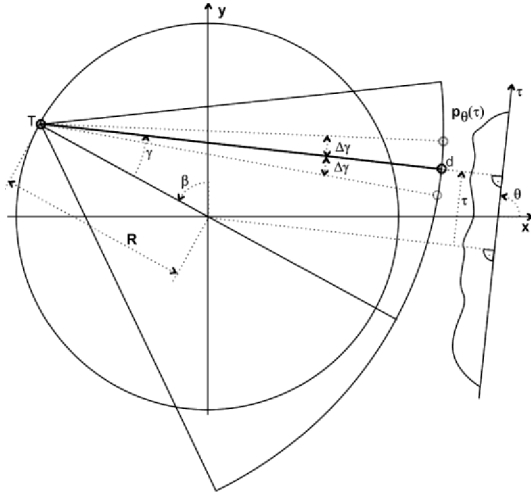


Figure 4-2: X-ray CT geometry (3rd generation): detectors d are positioned equiangularly in respect to the source of radiation T , having $\Delta\gamma$ angle difference

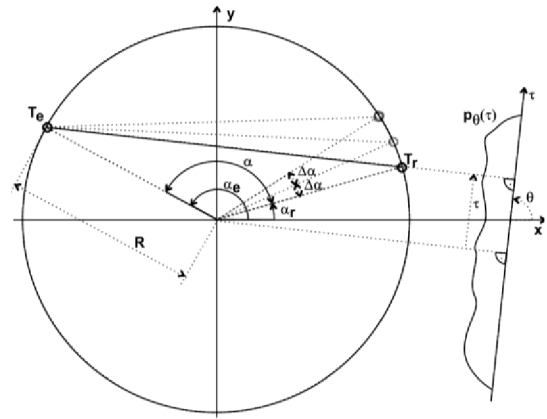


Figure 4-3: The Karlsruhe USCT geometry: receivers T_r are not positioned equiangularly in respect to the emitter T_e .

Equation (4.4) can only be used in the case, when the projections are formed by parallel ray-integrals (1st generation X-ray CT). For the case of the 3rd generation X-ray CT, the acquisition geometry is not parallel but resembles a fan of equiangular rays (Figure 4-2). A process called “rebinning” is used to rearrange the fan-beam ray-integrals data into parallel projections [35].

In the process of rebinning, the desired parallel-beam geometry projections $P_\theta(\tau)$ are formed from the available fan-beam geometry projections $R_\beta(\gamma)$ (Figure 4-2) using the following relations:

$$\tau = R \cdot \sin\gamma \quad (4.5)$$

$$\theta = \gamma + \beta \quad (4.6)$$

The position of the X-ray tube T and detectors d is defined by two angles β and γ . The angle vertices are located at the X-ray tube. R is the radius of the ring on which the tube rotates. τ and θ are two variables of the parallel geometry projections [35].

The transducers of the Karlsruhe 2D USCT (see chapter 2.2.1) are positioned on a fixed ring also in an equiangular geometry. However, this geometry differs from the one used in the 3rd generation X-ray CTs. The difference is in the position of the vertex of the “equiangles”. In case of the USCT the angle vertex is in the center of the ring (Figure 4-3) whereas in case of the X-ray CT the angle vertex lies on the ring (i.e. at the X-ray tube - Figure 4-2). Thus, while the projection fan in such X-ray CT can be considered equiangular, the projection fan in the USCT cannot.

In order to parallelize the projections, the standard rebinning algorithm could be applied to the USCT projections. The resulting parallel projections wouldn’t however be equidistantly spaced and therefore double interpolation would be necessary during the reconstruction.

A set of new rebinning relations (published in [77]) define the relationship between the USCT geometry projections $Q_{\alpha_e}(\alpha_r)$ and parallel beam geometry projections $P_\theta(\tau)$ (Figure 4-3):

$$\tau = R \cdot \cos(\alpha/2) = R \cdot \cos\left(\frac{|\alpha_e - \alpha_r|}{2}\right) \quad (4.7)$$

$$\theta = \alpha_e - \alpha/2 = \frac{\alpha_e + \alpha_r}{2} \quad (4.8)$$

The positions of the emitting transducer T_e and the receiving transmitter T_r are defined by the angles α_e and α_r . Both angle's vertexes are positioned at the center of the USCT ring.

4.3 The reflected beam reconstruction

A recently published method [31], based on log-spectra estimation of the ultrasonic attenuation coefficient, is taking advantage of the possibility to record directly transmitted, reflected, and scattered signals in USCT. Knowing the distances and propagation speeds, it is possible to determine the ultrasonic beam paths along which the signals are attenuated. Each path corresponds to a short segment of the recorded radiofrequency signals. In contrast to other known approaches, where only the first segment is used (corresponding to a direct transmission), here all of the segments are used for attenuation coefficient estimation. The spatial distribution of local attenuation can thus be reconstructed more precisely.

Unfortunately, this approach has a limitation. The method is only valid for a simplified model of the imaged volume, where only a small number of reflectors / scatterers are assumed. When two or more reflector / scatterer responses meet at the same moment at the receiving transducer, they are added together to form the recorded signal. When estimating the attenuation along one of these contributing paths, attenuations along the other paths are not taken into account, which yields an incorrect estimate.

The discrimination of responses from individual reflectors / scatterers is made possible by coherently processing a small neighboring set of the received radiofrequency signals – signals from a sub-array of the receiving transducers (Figure 4-4). The sub-array is treated as a phased array, thus enabling directional discrimination of signals (also known as beam steering). Larger size of the sub-array allows better focusing, unfortunately also corresponds to a wider path along which the attenuation can be estimated, resulting in a deterioration of spatial resolution. It can be shown that an optimal sub-array size depends on the distance from the reflector / scatterer. The farther it is, the larger size of the sub-array is necessary for proper focusing.

After the signals of the sub-array are coherently preprocessed, the corresponding attenuation coefficient can be estimated (e.g. via the log-spectrum method). The attenuation image is then reconstructed using estimated attenuation coefficients along all paths. As for the reconstruction method, only the unfiltered backprojection can be obtained by “smearing” the estimates along the respective ultrasonic beam paths. Filtered backprojection is not possible, because the reflected / refracted beams don't form parallel projections. A better choice is reconstructing the image via an algebraic reconstruction technique (ART) [35], enabling an arbitrary geometry of the integration paths.

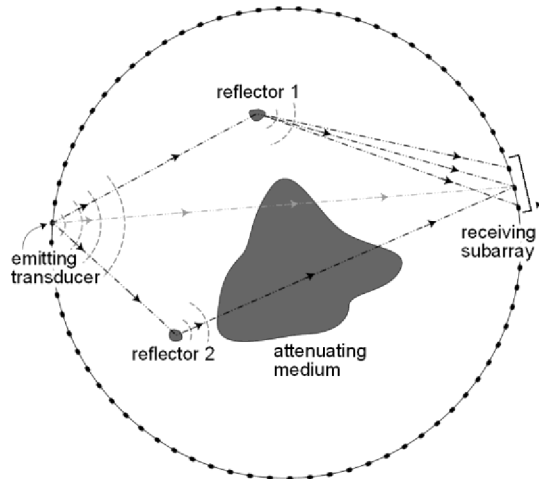


Figure 4-4: The ultrasonic beam paths in a USCT system. The receiving transducers record signals from all directions. Without coherent sub-array processing, the attenuation estimates do not correspond with the real attenuation values along the intended path.

4.4 Reconstruction Results

A scan of an ultrasonic phantom was performed at Forschungszentrum Karlsruhe, Germany. The phantom (Figure 4-5) is composed of a plastic container with a lid. Inside there are four parallel compartments filled with gelatine each of different reflectivity value. Unfortunately, this phantom serves mainly as a reflectivity phantom, and its attenuation values are not known. Nevertheless, we can assume that the attenuation values of the plastic case will differ from the ones of the gelatin or the water, and thus we should be able to distinguish these parts in the reconstructed image.

Figure 4-6 displays the conventional filtered backprojection algorithm (using the newly derived rebinning relations). Figure 4-7 displays the attenuation image after reconstruction using the direct and reflected signals (it is taken from [31] and is displayed for only comparison). Figure 4-8 was reconstructed using the direct and reflected signals and using the coherent processing of the neighboring signals.

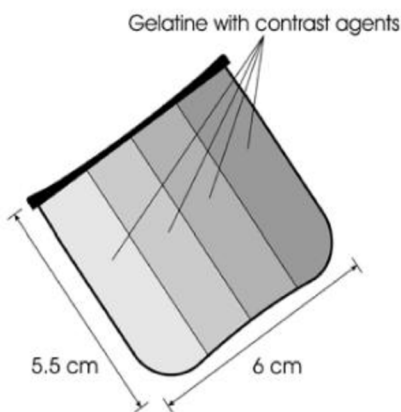


Figure 4-5: The schema of the used phantom

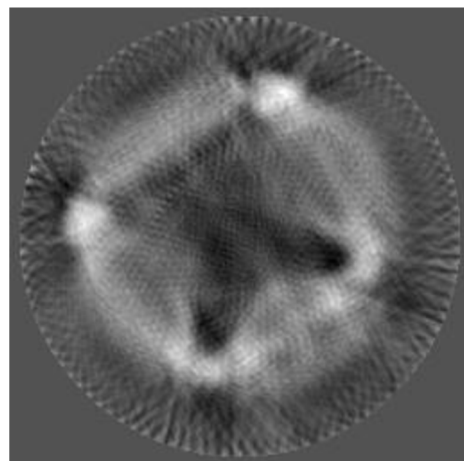


Figure 4-6: Filtered back-projection of direct ultrasonic beams, using a cosine windowed ramp filter

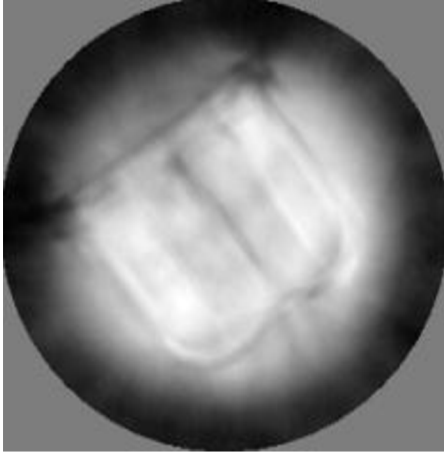


Figure 4-7: Reconstructed attenuation image using direct and reflected ultrasonic beams. (taken from [31])

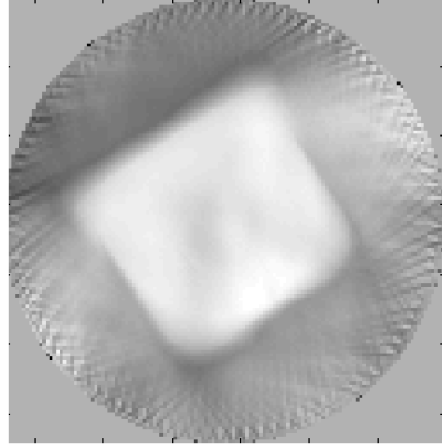


Figure 4-8: Reconstructed attenuation image using direct and reflected ultrasonic beams with coherent processing.

It is hard to evaluate which one of the reconstructions is closest to the ground truth, primarily because the real attenuation values are not known (at this early stage of the project, phantoms with the exact attenuation values were not yet available). But qualitatively, Figure 4-8 show the most resemblance in shape and attenuation values, which are considerably higher inside the phantom.

On the other hand the edges of the phantom are blurred. The loss of detail may be due to the fact that the speed of sound was assumed to be the same both inside and outside of the phantom.

Finally, all the above image reconstructions suffer from the fact that no calibration of the transducer elements was used. Attenuation was calculated based on the log spectra method, but it was assumed that the used transducers are omnidirectional with a flat transfer function across the whole spectrum of frequencies of the used wideband pulse. The exact geometry of the ultrasonic transducer elements were also not precisely known. Miniature differences of element positioning ($\lambda/2$ is in this case circa 0.2 mm) can account for phase cancelation in especially in the new coherent processing method.

5 Novel transducer sensitivity calibration method

Although it was clear from the beginning that some kind of correction will be needed to account for transducer directivity, differences in quality of the transducers, and also for the changing properties of the transducers with time due to aging, the problem has been never dealt with for the Karlsruhe USCT systems (see chapter 2.2)

Because it would be unfeasible to repeatedly measure the individual transducer parameters and directivity characteristics manually (especially for the newer 3D system), the author proposed a novel method, which estimates the transducer parameters automatically without any need of extra measurement equipment and without the necessity to disassemble the system. Using this method, the transducer parameters can be estimated based only on so-called empty measurements, where the USCT tank is filled with plain water.

The work on transducer sensitivity calibration was published in the proceedings of two international conferences in Prague [81] and New York [82].

5.1 The 2D sensitivity calibration method

Because there are some fundamental differences between the 2D and 3D Karlsruhe USCT systems the calibration method is first described and tested for the 2D system and then it is theoretically extended for the 3D case.

5.1.1 The measured signal model

The calibration is based on a series of wide-band measurements with the tank filled only with water (a so called “empty measurement”). The recorded pulses (decomposed via DFT into frequency components) can be modeled as

$$S_{e,r}(f) \cong R_e(f, \vartheta_{e \rightarrow r}) \cdot R_r(f, \vartheta_{e \leftarrow r}) \quad (5.1)$$

where $S_{e,r}(f)$ is the amplitude spectrum of the received signal (using emitter e and receiver r), $R_e(f, \vartheta_{e \rightarrow r})$ is the radiation function of the emitter, $R_r(f, \vartheta_{e \leftarrow r})$ the radiation function of the receiver, f is frequency, $\vartheta_{e \rightarrow r}$ is the emitting angle (towards the receiver), and $\vartheta_{e \leftarrow r}$ is the receiving angle (towards the emitter) – see Figure 5-1. The method assumes excitation of the emitter by a Dirac impulse, having a constant amplitude spectrum well above the high cutoff frequency of the transducers. Taking each emitter–receiver–frequency combination, a system of equations can be constructed and log-linearized:

$$\log(S_{e,r}(f)) = \log(R_e(f, \vartheta_{e \rightarrow r})) + \log(R_r(f, \vartheta_{e \leftarrow r})), \forall e, r \quad (5.2)$$

Solution of this system provides the unknown parameters of the sensors. For N transducers with $N-1$ possible emitting/receiving angles and M frequency bands we are able to build $N \cdot (N-1) \cdot M$ equations with the same number of unknown parameters. Thus, it is theoretically possible to solve for an independent radiation function for each of the used transducers.

Given the limitations of the used Karlsruhe 2D USCT experimental system, the measurements cannot provide a complete equation system. Only two movable ultrasonic probes simulate a ring of ultrasonic transducers surrounding the scanned volume. One of the probes is carrying an emitting transducer element; the other probe is carrying a linear array of 16 receiving transducer elements. Both move on a circular frame in 3.6° increments to simulate 100 emitters and 91×16 receivers (Figure 5-1).

For a certain position of the emitting transducer, the receiving probe is consecutively placed to the rest of the positions on the frame to record the transmitted ultrasonic waves. This

way a “projection” of the scanned volume is made. This process is repeated for each emitting position to record the rest of the projections - similarly as in X-ray tomography.

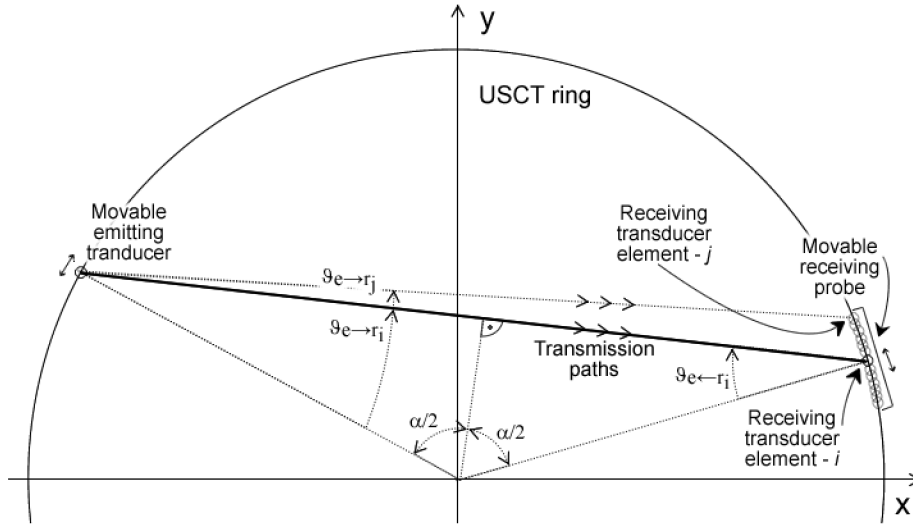


Figure 5-1: Geometry of the tomographic plane. The emitting transducer, receiving transducer and the center of the USCT ring form an equilateral triangle.

5.1.2 The equation system

Because only the empty measurements (USCT tank filled only with water) are used for the calibration, and the same (movable) set of transducers is used to make the whole set of projections, all of the projections should mutually contain the same information. Thus, all projections are linearly dependent, and by adding more projections, the solution gets more robust to noise (in the least mean squares sense).

For the Karlsruhe 2D USCT experimental setup using N_{e-pos} emitter probe positions (projections), 1 emitter transducer element, N_{r-pos} receiver probe positions, N_{r-el} receiver transducer elements, N_{freq} frequency bands, and N_{ang} emitting/receiving angles, we are able to build

$$N_{r-pos} \cdot N_{r-el} \cdot N_{freq} = 91 \cdot 16 \cdot 64 = 93184 \quad (5.3)$$

linearly independent equations, and

$$\begin{aligned} (1 + N_{r-el}) \cdot N_{freq} \cdot N_{ang} &= \\ &= (1 + 16) \cdot 64 \cdot (16 \cdot 91) = 1584128 \end{aligned} \quad (5.4)$$

unknowns. As can be seen from these calculations, the system is greatly underdetermined and some simplifying assumptions are necessary to reduce the number of unknowns.

5.1.3 Stabilizing the system

We can assume that all elements have identical radiation functions, because they are all of equal geometry and manufactured equally. The minor differences independent on direction and frequency caused by fatigue and material flaws may be represented by an individual multiplicative constant. We can call this constant *efficiency* (when the transducer is in emitting mode) or *sensitivity* (for the receiving mode), both supposedly equal (or rather linearly coupled). Thus, the radiation function of each transducer can be modeled by a product of a common 2D directivity function $D(f, \vartheta)$ and an individual sensitivity s (or efficiency e):

$$R(f, \vartheta) = s \cdot D(f, \vartheta) \quad (5.5)$$

Since there is only one transducer element, which is gradually moved to all of the emitting positions, its efficiency contributes equally to every measurement. The efficiency parameter is inseparable from the magnitude of the directivity function. If one is multiplied by any number and the other is divided by the same number, the product stays the same, thus allowing an infinite number of solutions – the system is ill-posed.

The efficiency parameter is not solvable in this case and must be constrained to a certain predefined value, in order to make the system solvable, e.g.:

$$\log(e) = 0, \quad (5.6)$$

i.e. the efficiency e of the emitting transducer is equal to one.

By separating the receiver radiation function into two unknown entities, the sensitivity and the directivity function, we reduce the number of unknowns dramatically to:

$$\begin{aligned} 1 + N_{r-el} + N_{freq} \cdot N_{ang} &= \\ &= 1 + 16 + 64 \cdot (16 \cdot 91) = 93201. \end{aligned} \quad (5.7)$$

Although this is a considerable amount, the equation set is still ill-formed. Because each equation contains only one sensitivity parameter (belonging to only one of the 16 receiver elements), there is no relation in the equation set between the different receiver sensitivities. The equation set is actually formed by separate subsets of equations, each belonging to just one of the receiver elements. All equations within this one subset are linearly dependent, having the inseparable pair: sensitivity and directivity function (as previously discussed for the case of the emitter). Luckily, if we don't insist on obtaining the absolute values of the transducer parameters, a relative solution can be defined by adding a suitable constraint to the system, e.g.:

$$\sum_{r-elements} \log(s_r) = 0 \quad (5.8)$$

or in other words: the product of sensitivities s of all of the receiver elements will be equal to one. This equation makes the needed relation between the separate subsets of equations.

It is important to note that by introducing this constraint, we can never get the absolute values of sensitivities, but we are able to solve the important mutual relations.

To further decrease the number of unknowns, we can assume that the geometrical symmetry of each transducer element leads to a mirror symmetry of the directional characteristic in the image plane. Taking into account the scanning geometry (Figure 5-1):

$$D(f, \vartheta_{e \rightarrow r}) = D(f, \vartheta_{e \leftarrow r}) = D(f, \vartheta_{e \leftrightarrow r}). \quad (5.9)$$

Therefore, only half of the directional coefficients need to be calculated and the number of unknowns finally decreases below the number of equations:

$$\begin{aligned} 1 + N_{r-el} + N_{freq} \cdot N_{ang} &= \\ &= 1 + 16 + 64 \cdot (16 \cdot 46) = 47121 \end{aligned} \quad (5.10)$$

To make the system even more overdetermined we can make one final simplification. It is reasonable to assume a smooth change in the shape of the 2D directivity function along the angular axis. Then we can neglect the slight variation of the directivity function in the range of the 16 receiving elements (in a certain receiving and emitting arrangement) - see Figure 5-1:

$$D(f, \vartheta_{e \leftrightarrow r-el_1}) = D(f, \vartheta_{e \leftrightarrow r-el_2}) = \dots = D(f, \vartheta_{e \leftrightarrow r}). \quad (5.11)$$

With this approximation, the number of unknowns further decreases significantly to:

$$\begin{aligned} 1 + N_{r-el} + N_{freq} \cdot N_{ang} &= \\ &= 1 + 16 + 64 \cdot 46 = 2961 \end{aligned} \quad (5.12)$$

Utilizing the above-mentioned assumptions in the log-linearized transmission signal model eq. (5.2), we arrive at the final equation system:

$$\log(S_{e,r}(f)) = \log(e) + \log(s) + 2 \cdot \log(D(f, \vartheta_{e \leftrightarrow r})), \forall e, r \quad (5.13)$$

5.1.4 Sensitivity calibration results based on experimental data

The proposed method was tested on the experimental 2D USCT system developed in Forschungszentrum Karlsruhe, Germany (see chapter 2.2.1).

Using data of the measurements in this geometry we have constructed a system of over 280 000 equations (using only 3 projections) with nearly 3 000 unknowns. The unknowns were solved for in the means of minimum square error using the QR decomposition method [46]. Figure 5-2 displays an example of the common directivity function obtained this way. The set of the relative efficiency coefficients for the receiving sensors is shown in Table 1.

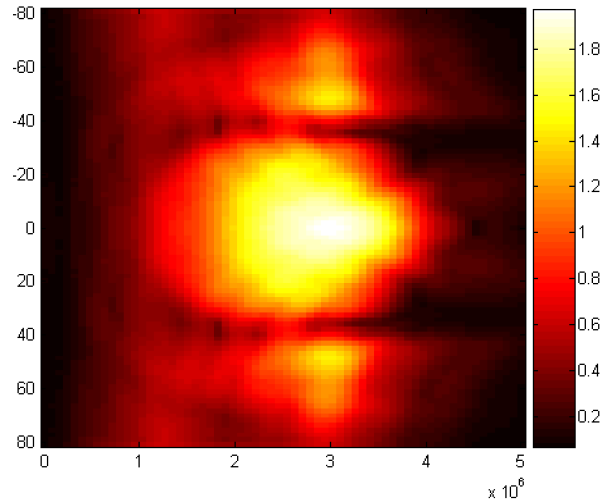


Figure 5-2: Obtained directivity function: vertical axis - emitting angle (degrees), horizontal axis - frequency (MHz)

Table 1: Calculated relative efficiencies of the receiving sensors														
Sensor number	1	6	3	8	5	10	7	12	9	14	11	16	13	15
Relative sensitivity	0.75	0.95	1.15	0.97	0.99	0.89	1.04	0.95	0.99	1.06	0.98	1.09	1.11	1.15

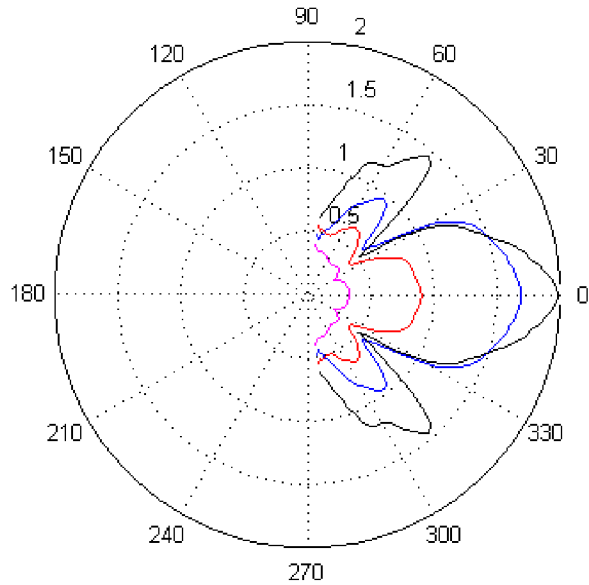


Figure 5-3: Angle dependency of the directivity function for different frequencies.

In Figure 5-3 we can see normalized directivity patterns for different frequency bands (vertical slices of the 2D directivity function plotted in polar coordinates), whereas in Figure 5-4, spectral transfer functions for different emitting/receiving angles (horizontal slices of the 2D radiation function) are depicted.

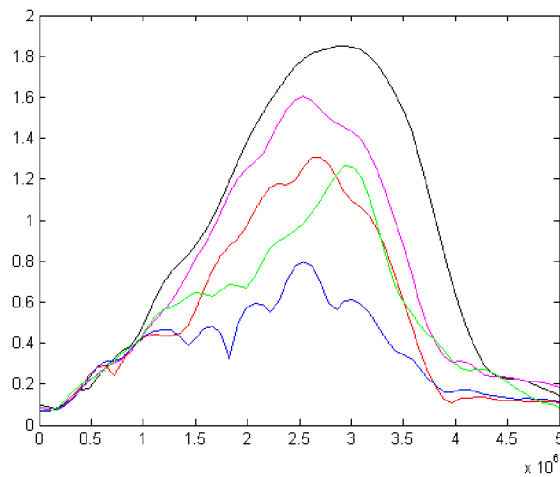


Figure 5-4: Frequency dependency of the directivity function at different angles. Horizontal axis: frequency (MHz).

5.1.4.1 Verification via hydrophone measurement

In order to verify the calculated results a set of measurements of the used transducers was performed. The emitted pressure field was measured with a hydrophone, along several semi arcs (in 5-degree steps) around the transducer at various distances [49]. The values were normalized with respect to the highest peak of the received pulse. These values were then compared with the calculated values of the directivity function along the center frequency – cca. 2.9 MHz - (also normalized to the highest value). As can be seen in Figure 5-5, these angular profiles show a reasonable correlation.

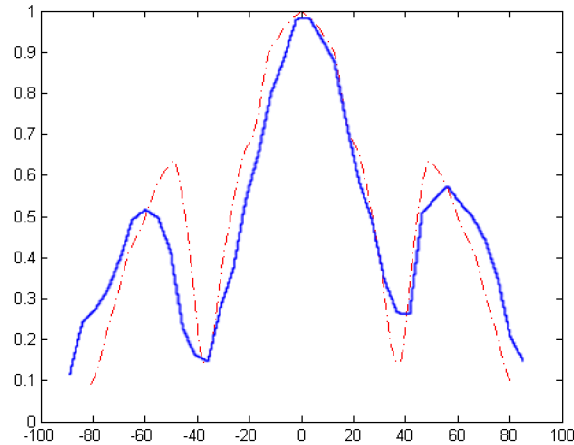


Figure 5-5: Comparison of angular characteristics. Solid - the pressure amplitude of the emitted field measured with a hydrophone. Dashed - computed directivity profile around the center frequency of the transducer.

5.1.4.2 Comparison with wave-equation based simulation

Although the measured and calibrated directivity pattern are well correlated, the calculated characteristics contain substantial side-lobes while theoretically only a single main lobe should be present taking into account the small concrete geometrical dimensions of the transducers. In order to try to resolve this problem, a completely independent approach was applied to directional characteristics computation, which enables in principle to take into account not only possibly uneven distribution of both amplitude and phase on the transducer surface but namely also a coupling between neighboring transducers leading to attenuated and phase shifted contributions to the radiated field [83].

This approach was based on Helmholtz wave equation and was solved in the Matlab computing environment using the Partial Differential Equation (PDE) Toolbox. The finite element method (using circa 235,000 nodes and 465,000 elements) was used to evaluate the radiation function.

The results of the wave-equation approach are shown in Figure 5-6. Although the theoretical single-transducer moving-piston model results in the expected single main lobe angular characteristic, it was found that if the neighboring transducers are allowed to oscillate due to some electromechanical coupling with phase shifts, the angular characteristic start to behave in a similar way as was calculated by the proposed calibration method and measured by hydrophone.

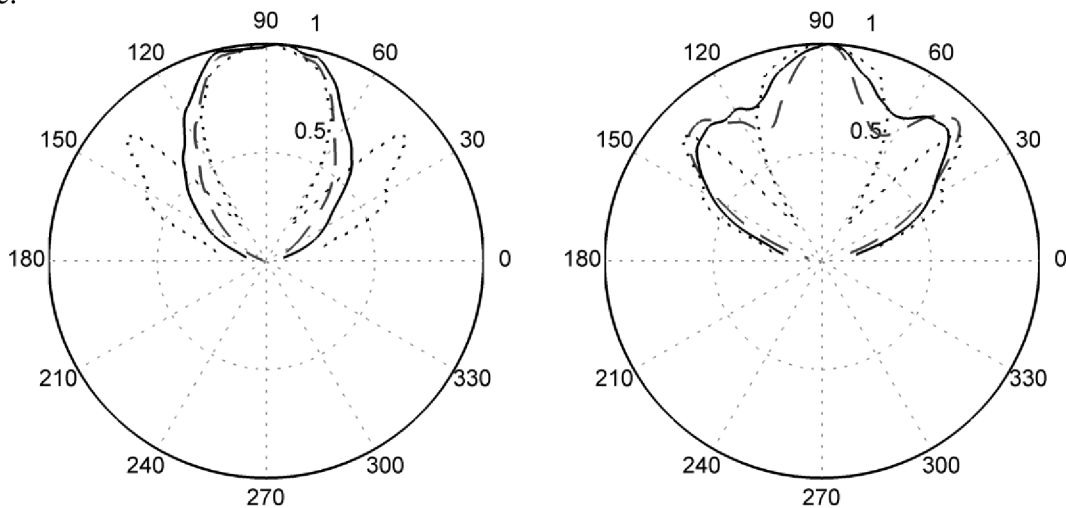


Figure 5-6: Comparison of angular characteristics. The wave equation result in solid line, distance-corrected

wave-equation result in dashed line, and the presented calibration method result in dotted line. Left graph shows the wave-equation results for the single transducer solution. The right graph shows the multiple transducer solution with electromechanical crosstalk allowed.

5.2 Theoretical extension to 3D

The calibration method proposed to the 2D system can be extended for the 3D USCT system newly built in the FZK Karlsruhe (see chapter 2.2.2). The main differences between the two systems are:

- the sending and receiving transducers are not in a relative motion any more
- there are many (not only one) sending transducer elements
- the electrical signal sent to the input of the sending transducer is not a single impulse but a controlled shaped oscillating pulse with limited frequency content.

Due to these changes, the whole concept of the 2D calibration (5.1) has to be altered.

The 3D transducer sensitivity calibration is built on a more detailed model. Account had to be taken for the changing distances between the emitters and receivers in a cylindrical geometry of the USCT and also for the individual conversions from electrical signals to ultrasonic signals and back.

The model of the signal spectrum is the following:

$$S_{out} = S_{in} \cdot T_{ee} \cdot T_e \cdot T_w \cdot T_r \cdot T_{re} \quad (5.14)$$

where:

$S_{out} = S_{out}(i,j,k)$... spectrum of the output pulse (recorded signal)

$S_{in} = S_{in}(i,j,k)$... spectrum of the input pulse

$T_{ee} = T_{ee}(i,k)$... the transfer function of the emitter electronics,

$T_e = T_e(\nu_{i \rightarrow j}, \varphi_{i \rightarrow j}, i, k)$... the transfer functions of the emitting transducer elements (in the direction of the receiver),

$T_w = T_w(d_{i,j}, k)$... the transfer function of the water path,

$T_r = T_r(\nu_{i \leftarrow j}, \varphi_{i \leftarrow j}, j, k)$... the transfer functions of the receiving transducer elements (in the direction of the emitter), and

$T_{re} = T_{re}(j,k)$... the transfer function of the receiver electronics

and

i ... is the number of the emitter element

j ... is the number of the receiver element

k ... is the order of the DFT frequency component

$d_{i,j} = |\vec{r}_e(i) - \vec{r}_r(j)| = \sqrt{(x_e - x_r)^2 + (y_e - y_r)^2 + (z_e - z_r)^2}$... is the distance between emitter and receiver (length of the signal path)

$\nu_{i \rightarrow j}$... is the azimuth angle of transmission (on the emitter side)

$\nu_{i \leftarrow j}$... is the azimuth angle of reception (on the receiver side)

$\varphi_{i \rightarrow j}$... is the elevation angle of transmission (on the emitter side)

$\varphi_{i \leftarrow j}$... is the elevation angle of reception (on the receiver side)

We can now use the same linearization scheme as in the 2D calibration to obtain a system of linear equations:

$$\log(S_{out}) = \log(S_{in}) + \log(T_{ee}) + \log(T_e) + \log(T_w) + \log(T_r) + \log(T_{re}) \quad (5.15)$$

If we go back to the nonlinear form of the recorded pulse spectrum model (5.14), we can see that the product of the two transfer functions for a particular emitter-receiver combination is inseparable. The emitter emits ultrasonic waves at this angle only to this

single receiver. And vice versa, the receiver receives ultrasonic waves at this angle only from this particular emitter. Therefore, using only the information from the empty measurement, we are not able to solve for all of the unknowns.

A simplification can be made (just as was done for the 2D calibration) by assuming that the angular characteristic of the transducers is symmetrical (along both the azimuth and elevation axis) and that the angular characteristic will be the same for all transducers except for a multiplicative constant: sensitivity and efficiency for receivers and emitters respectively.

Because of the symmetry of the USCT geometry, for a particular emitter-receiver combination both the azimuth and the elevation angles are the same on the emitting and receiving sides, except for a change in their sign:

$$\begin{aligned} v_{i \rightarrow j} &\cong (180 - |\psi_{e,r}|)/2 = |\arctg(y_r/x_r) - \arctg(y_e/x_e)| \\ v_{j \leftarrow i} &\cong -(180 - |\psi_{e,r}|)/2 = -|\arctg(y_r/x_r) - \arctg(y_e/x_e)| \\ v_{i \rightarrow j} &\cong -v_{i \leftarrow j} \end{aligned} \quad (5.16)$$

and

$$\varphi_{i \rightarrow j} \cong -\varphi_{i \leftarrow j} \quad (5.17)$$

Let us define a common 3D radiation function:

$$R(v_{i \rightarrow j}, \varphi_{i \rightarrow j}, k) = R(v_{i \leftarrow j}, \varphi_{i \leftarrow j}, k) = R(v_{i \leftrightarrow j}, \varphi_{i \leftrightarrow j}, k) \quad (5.18)$$

which is symmetrical along both angular axes. Then the emitter and receiver transfer functions can be written as products of the radiation function and an individual efficiency or sensitivity for the particular transducer:

$$\begin{aligned} T_e(i, v_{i \rightarrow j}, k) &\cong e_i \cdot R(v_{i \leftrightarrow j}, \varphi_{i \leftrightarrow j}, k) \\ T_r(j, v_{i \leftarrow j}, k) &\cong s_j \cdot R(v_{i \leftrightarrow j}, \varphi_{i \leftrightarrow j}, k) \end{aligned} \quad (5.19)$$

Substituting the above relations into (5.14), we once more run into the same problem of inseparability of the efficiency and transfer function of the emitter electronics on one side: $T_{ee}(i, k) \cdot e_i$, and sensitivity and transfer function of the receiver electronics on the other side: $T_{re}(j, k) \cdot s_j$. Both always appear together and are therefore inseparable. We can again simplify and define a modified electronics transfer functions

$$\begin{aligned} T_{ee}(i, k) \cdot e(i) &\cong T'_{ee}(i, k) \\ T_{re}(j, k) \cdot s(j) &\cong T'_{re}(j, k) \end{aligned} \quad (5.20)$$

which include the efficiency or sensitivity parameters.

The transfer function of the water path can be substituted by

$$T_w = e^{-\beta_w f d} \quad (5.21)$$

where β_w is the ultrasonic attenuation parameter of water, f is the frequency, and d is the emitter – receiver distance (e here denotes the base of the natural logarithm, not the efficiency).

Putting this all together, we can write the following equations to model the recorded pulse spectrum:

$$\begin{aligned} S_{out}(i, j, k) &= S_{in} \cdot T'_{ee}(i, k) \cdot R(v_{i \leftrightarrow j}, \varphi_{i \leftrightarrow j}, k) \cdot e^{-\beta_w f d} \cdot R(v_{i \leftrightarrow j}, \varphi_{i \leftrightarrow j}, k) \cdot T'_{re}(j, k) \\ S_{out}(i, j, k) &= S_{in} \cdot e^{-\beta_w f d} \cdot R^2(v_{i \leftrightarrow j}, \varphi_{i \leftrightarrow j}, k) \cdot T'_{ee}(i, k) \cdot T'_{re}(j, k) \end{aligned} \quad (5.22)$$

$$\log(S_{out}(i, j, k)) = \log(S_{in}) - \beta_w f d_{ij} + 2 \cdot \log(R(v_{i \leftrightarrow j}, k)) + \log(T'_{ee}(i, k)) + \log(T'_{re}(j, k))$$

Unfortunately, the lack of time did not permit the author to implement and test the proposed extension of the method to 3D. It was decided to be more beneficial for the project to concentrate on the novel position calibration method described in the next section.

6 Novel transducer position calibration method

This section focuses on a novel calibration method for the transducer positions. The theoretical principles are described, as well as the numerical analysis and tests carried out on real data. First, the method is theoretically described in 6.1. An essential principle – anchoring – necessary for the calibration method to work properly is described in 6.2. In 6.3, the method is numerically evaluated for convergence and accuracy. Chapter 6.5 focuses on the calibration of the experimental 3D USCT developed in Forschungszentrum Karlsruhe. A new pulse detection technique as well as other additions and modifications to the calibration procedure necessary for the calibration to work with the real data are described. The impact of the calibration on the reconstructed images is shown in the concluding chapter 7.1.3.

The calibration method and results were presented on the international conferences in Lyon [84], Riga [85], and Vancouver [86].

6.1 Formulation of the position calibration method

The algorithm used for the position calibration is based on the principles used in the global positioning system (GPS) navigation [26] similarly as it was done for an underwater ultrasound imaging system (UUIS) [46]. Ultrasonic transmitters and receivers in USCT can replace the satellite transmitters and mobile receiver units in GPS. However, unlike in GPS or UUIS, none of the positions of the emitters or receivers in USCT are assumed to be known and all are the to-be-calibrated unknowns. The method is capable of calibrating the positions of all ultrasonic transducers and their individual time delays at once. Contrary to UUIS, no calibration phantoms are necessary.

For the USCT calibration, a so-called empty measurement has to be made. In such a measurement, the tank is filled only with water. Each emitter is excited to produce an ultrasonic pulse wave, which travels through the water and reaches all receiving transducers. Each of the receivers records an A-scan signal (Figure 6-1). The complete measurement consists of consecutively firing all emitters (one emitter at a time).

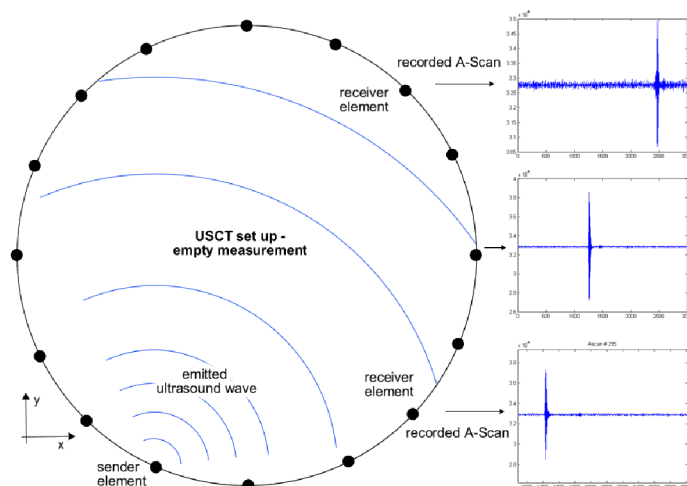


Figure 6-1: The USCT system (a simplified schematic view from the top)

In each A-scan one or more pulses can be detected. The first one corresponds to the direct path of the ultrasound wave from the emitter to the receiver, whereas later pulses correspond to paths including reflections from the tank walls or the water surface.

The calibration method calculates the transducer positions and time-delays introduced by the electronics processing the signals on both the transmission and reception sides. The calculations are based on *time-of-arrival* (TOA) measurements of the direct pulse for each available emitter-receiver combination.

The next two sub-chapters describe the calibration method mathematically. The definition of the TOA is an important aspect, which has a great effect on the calibration accuracy, as will be shown below. In 6.1.1, the TOAs are defined conventionally (as in GPS) as functions of the individual transducer positions. In 6.1.2, advantage is taken of the fact that the transducers surrounding the USCT tank are grouped into several transducer array systems (or TAS, see chapter 2.2.2) within which the positions of the transducers are known. The TOAs are then defined as functions of positions and orientations of the whole TASes.

6.1.1 The ITE (individual transducer element) approach

Let us first introduce some necessary notation: Let $S = \{s_i, i = 1 \dots M\}$ and $R = \{r_i, i = 1 \dots N\}$ be two disjoint sets of the active emitters and receivers respectively (the letter s was chosen to comply with other Karlsruhe documentation – the German word for emitter is “sender”). Further, let $P = \{(s, r)_k, k = 1 \dots Q\}$ be a set of pairs (s, r) , $s \in S, r \in R$ such that for each pair $(s, r) \in P$ we can detect the direct pulse in the corresponding A-scan and obtain a *measured time-of-arrival* value $MTOA_{sr}$.

Next, let $\mathbf{x}_s = [x_s, y_s, z_s, \tau_s]$ and $\mathbf{x}_r = [x_r, y_r, z_r, \tau_r]$ be the vectors of the unknown emitter and receiver position coordinates (of the elements’ surface centers) and time-delays. We can now define the *computed time-of-arrival* $CTOA$ as a function dependent on the individual transducer element parameters:

$$CTOA_{sr}(\mathbf{x}_s, \mathbf{x}_r) = \frac{\sqrt{(x_s - x_r)^2 + (y_s - y_r)^2 + (z_s - z_r)^2}}{v} + \tau_s + \tau_r \quad (6.1)$$

where v is the ultrasound velocity.

The above equation is very similar to the so-called pseudorange equation used in GPS [26], where the time delay components are analogical to the satellites’ and receivers’ clocks offsets. There is a major difference, though, in the fact that in the USCT, neither the emitter nor the receiver positions and delays are assumed to be known. The only known parameter is the speed of sound in water v , which (in a controlled environment) can be very accurately calculated if the temperature is known [6].

Taking the emitter-receiver pairs from the set P , we have two comparable vectors - $\mathbf{CTOA}_P = [CTOA_{s,r}]$ as the vector of the computed time-of-arrival values for all the emitter-receiver pairs $(s, r) \in P$ and $\mathbf{MTOA}_P = [MTOA_{s,r}]$ as the vector of the experimentally measured values of time-of-arrival. The task can be now formulated as follows: *Find the vector $\mathbf{x} = [x_s, x_r], (s, r) \in P$ of unknown positions and delay parameters of all the emitters in S and receivers in R such that the norm of difference between \mathbf{CTOA}_P and \mathbf{MTOA}_P is minimized.*

In other words, minimize a residual F_P :

$$\begin{aligned} \min_{\mathbf{x}} F_P(\mathbf{x}) &= \min_{\mathbf{x}} \left\{ \frac{1}{2} \|\mathbf{CTOA}_P - \mathbf{MTOA}_P\|^2 \right\} \\ &= \min_{\mathbf{x}} \left\{ \frac{1}{2} \sum_{(s,r) \in P} (CTOA_{sr} - MTOA_{sr})^2 \right\} \end{aligned} \quad (6.2)$$

where the minimization runs in the vector space of unknown parameters \mathbf{x} , which influences \mathbf{CTOA}_P .

Apparently, the task can be regarded as a non-linear least-squares problem, where the functional F_P depends on $4M + 4N$ variables, where $M = |S|$ is number of emitters, $N = |R|$ is

number of receivers (each having coordinates in 3D space and a time-delay parameter). Therefore, we can apply the Gauss-Newton iteration, which minimizes a functional F iteratively, solving in each step a linearized system

$$\mathbf{J}(\mathbf{x}^k)^T \mathbf{J}(\mathbf{x}^k) \Delta \mathbf{x}^k = -\mathbf{J}(\mathbf{x}^k)^T \mathbf{f}(\mathbf{x}^k) \quad (6.3)$$

where k is the iteration number, $\mathbf{J}(\mathbf{x}^k)$ is the Jacobian matrix of the functional F at \mathbf{x}^k , \mathbf{f}^k is the actual value of the residual, and $\Delta \mathbf{x}^k$ is the correction vector used for the calculation of the new estimate of the parameter vector \mathbf{x} :

$$\mathbf{x}^{k+1} = \mathbf{x}^k + \Delta \mathbf{x}^k \quad (6.4)$$

In our setting, the quantity \mathbf{MTOA}_P is fixed during the process of minimization whereas \mathbf{CTOA}_P changes as we approach to more precise value of the parameter vector \mathbf{x} . The initial value of \mathbf{CTOA}_P^0 is then computed using the initial estimates of the position and delay parameters determined from the roughly known physical dimensions of the setup.

To be able to use the Gauss-Newton method, we need to formulate the vector \mathbf{f}^k of residuals

$$\mathbf{f}_P^k = [\mathbf{f}_{sr}^k] = \mathbf{MTOA}_P - \mathbf{CTOA}_P^k \quad (6.5)$$

and the matrix \mathbf{J}^k , the elements of which are the partial derivatives of the residuals:

$$\mathbf{J}^k = (\mathbf{J}_{i,j}^k) = \left(\frac{\partial \mathbf{f}_i^k}{\partial x_j} \right) \quad (6.6)$$

where the index $i = 1 \dots MN$ spans the number of emitter-receiver pairs, and the index $j = 1 \dots 4M+4N$ spans the number of estimated parameters. One row of the matrix contains the partial derivatives of a particular emitter-receiver pair residual f_{sr} with respect to all of the emitter and receiver parameters in \mathbf{x} . However the only nonzero partial derivatives of f_{sr} are the ones with respect to the x_s, y_s, z_s, τ_s and x_r, y_r, z_r, τ_r parameters of the corresponding emitter-receiver pair:

$$\begin{aligned} \frac{\partial f_{sr}^k}{\partial x_s} &= \frac{x_s^k - x_r^k}{vd_{sr}^k}, & \frac{\partial f_{sr}^k}{\partial y_s} &= \frac{y_s^k - y_r^k}{vd_{sr}^k}, & \frac{\partial f_{sr}^k}{\partial z_s} &= \frac{z_s^k - z_r^k}{vd_{sr}^k}, & \frac{\partial f_{sr}^k}{\partial \tau_s} &= 1, \\ \frac{\partial f_{sr}^k}{\partial x_r} &= \frac{-(x_s^k - x_r^k)}{vd_{sr}^k}, & \frac{\partial f_{sr}^k}{\partial y_r} &= \frac{-(y_s^k - y_r^k)}{vd_{sr}^k}, & \frac{\partial f_{sr}^k}{\partial z_r} &= \frac{-(z_s^k - z_r^k)}{vd_{sr}^k}, & \frac{\partial f_{sr}^k}{\partial \tau_r} &= 1 \end{aligned} \quad (6.7)$$

where $d_{sr}^k = \sqrt{(x_s^k - x_r^k)^2 + (y_s^k - y_r^k)^2 + (z_s^k - z_r^k)^2}$ is the emitter-receiver distance estimate.

Summarizing, the k -th equation in the equation system (6.3) have the following form:

$$\begin{aligned} \frac{x_s^k - x_r^k}{vd_{sr}^k} \Delta x_s^k + \frac{y_s^k - y_r^k}{vd_{sr}^k} \Delta y_s^k + \frac{z_s^k - z_r^k}{vd_{sr}^k} \Delta x_s^k + \Delta \tau_s^k + \\ - \frac{x_s^k - x_r^k}{vd_{sr}^k} \Delta x_r^k - \frac{y_s^k - y_r^k}{vd_{sr}^k} \Delta y_r^k - \frac{z_s^k - z_r^k}{vd_{sr}^k} \Delta z_s^k + \Delta \tau_s^k = \mathbf{MTOA}_{sr} - \mathbf{CTOA}_{sr}^k \end{aligned} \quad (6.8)$$

An example of the linearized system (6.3) in the matrix form for a simplified 2D setup (only the x and y position coordinates are being calibrated) is shown in Equation (6.9) (see next page).

To cope with the presence of noise in measurements, we require the number of the measured time-of-arrival values $Q = |P| = MN$ to be significantly larger than the number of unknown variables $V = 4M + 4N$, i.e. $MN \gg 4M + 4N$. This requirement is more than accomplished in the current Karlsruhe 3D USCT set up as $Q = 384 \cdot 1536 = 589,824$ and $V = 4 \cdot 384 + 4 \cdot 1536 = 7,680$. This means, the system (6.3) is over-determined.

An alternative to the Gauss-Newton method, the Levenberg-Marquardt method, is more suited for strong nonlinearities in the minimization function and is discussed in chapter 6.2.

All the empty elements of the system matrix are zero and the reader can see that the matrix is very sparse. Figure 6-2 displays the sparsity pattern of the system matrix for the ITE approach. The left side of the matrix contains only emitter parameters while the right side only the receiver parameters. The displayed system matrix is of a greatly reduced size (about 140 unknowns and 500 equations). It is not possible to present the sparsity pattern for a full size Karlsruhe USCT system matrix in the same way (each colored pixel representing a nonzero cell). The full size USCT system matrix would need to be 7,680 pixels wide (the number of unknowns) and 589,824 pixels high (the number of equations) image to represent all the matrix elements. This would result in a circa 4.5 giga-pixel image, which is not feasible to present in print.

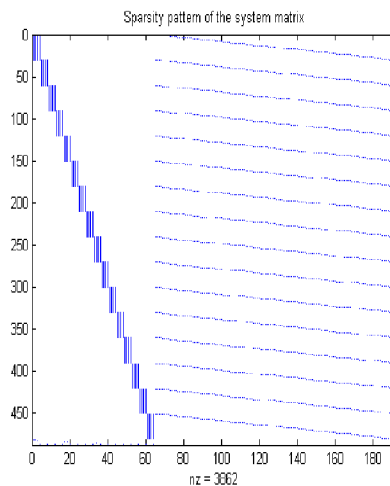


Figure 6-2: Sparsity pattern of the system matrix.

Also not feasible is to store the full system matrix into a standard computer's memory. The matrix would have to occupy about 72GB of RAM memory if stored in a standard double-precision format. The solution is to store only the nonzero elements of the matrix (supported for example by the Matlab's "sparse" format). As there are only 8 nonzero elements per row, the memory requirements significantly drop below about 100MB, which is well within the capabilities of modern PCs.

6.1.2 The TAS (transducer array system) approach

In order to achieve greater accuracy and make the calibration less prone to TOA detection errors, we can use additional information about positions of the transducers within a transducer array system (TAS - for technical details on the TAS see chapter 2.2). Because each TAS is manufactured in the same way (including a precise sawing technique, [68]) we can assume that all transducer elements in a TAS lie on a plane in known positions. We can reformulate the calibration problem to involve the *positions and orientations of TASes* rather than the individual positions of the separate transducer elements.

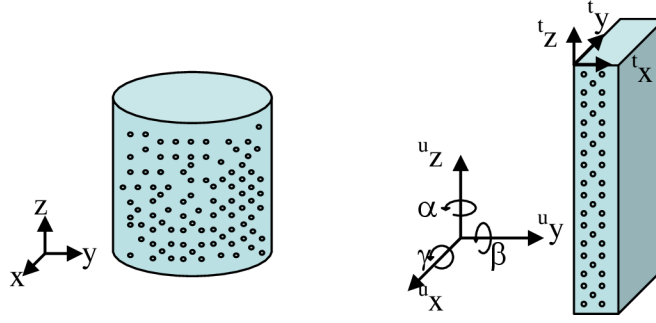


Figure 6-3: In the ITE approach we seek to find the positions of individual transducer elements on the USCT cylinder, whereas in the TAS approach we seek the positions and orientations of the TAS casings.

To express the relationship of the transducer positions in the USCT (world) coordinate system $\{^u x, ^u y, ^u z\}$ and the TAS coordinate system $\{^t x, ^t y, ^t z\}$ (with the origin in the center of the TAS surface) the x-y-z fixed-angle parameterization scheme, described in [13], was adopted. The coordinate transformation is done by first rotating the TAS by γ around the $^u x$ axis, then by β around the $^u y$ axis, and last by α around the $^u z$ axis. Finally, the whole TAS is translated by $\{x, y, z\}$. Using the above scheme, the transformation of each point from the TAS coordinate system to the USCT coordinate system can be expressed as a multiplication of a position vector by a homogeneous rotation-translation matrix:

$$\begin{bmatrix} ^u x \\ ^u y \\ ^u z \\ 1 \end{bmatrix} = \begin{bmatrix} \cos(\alpha)\cos(\beta) & \cos(\alpha)\sin(\beta)\sin(\gamma) - \sin(\alpha)\cos(\gamma) & \cos(\alpha)\sin(\beta)\cos(\gamma) + \sin(\alpha)\sin(\gamma) & x \\ \sin(\alpha)\cos(\beta) & \sin(\alpha)\sin(\beta)\sin(\gamma) + \cos(\alpha)\cos(\gamma) & \sin(\alpha)\sin(\beta)\cos(\gamma) - \cos(\alpha)\sin(\gamma) & y \\ -\sin(\beta) & \cos(\beta)\sin(\gamma) & \cos(\beta)\cos(\gamma) & z \\ 0 & 0 & 0 & 1 \end{bmatrix} \begin{bmatrix} ^t x \\ ^t y \\ ^t z \\ 1 \end{bmatrix} \quad (6.10)$$

The above relations can be used to redefine the computed time-of-arrival $CTOA_{sr}$ in (6.1) as a function of the positions and orientations of TASes rather than individual transducer elements:

$$\begin{aligned} CTOA_{sr} &= \sqrt{d_x^2 + d_y^2 + d_z^2}/v + \tau_s + \tau_r \\ d_x &= \cos(\alpha_{st})\cos(\beta_{st})x_{se} + (\cos(\alpha_{st})\sin(\beta_{st})\cos(\gamma_{st}) + \sin(\alpha_{st})\sin(\gamma_{st}))z_{se} + x_{st} \\ &\quad - \cos(\alpha_{rt})\cos(\beta_{rt})x_{re} - (\cos(\alpha_{rt})\sin(\beta_{rt})\cos(\gamma_{rt}) + \sin(\alpha_{rt})\sin(\gamma_{rt}))z_{re} - x_{rt} \\ d_y &= \sin(\alpha_{st})\cos(\beta_{st})x_{se} + (\sin(\alpha_{st})\sin(\beta_{st})\cos(\gamma_{st}) - \cos(\alpha_{st})\sin(\gamma_{st}))z_{se} + y_{st} \\ &\quad - \sin(\alpha_{rt})\cos(\beta_{rt})x_{re} - (\sin(\alpha_{rt})\sin(\beta_{rt})\cos(\gamma_{rt}) - \cos(\alpha_{rt})\sin(\gamma_{rt}))z_{re} - y_{rt} \\ d_z &= -\sin(\beta_{st})x_{se} + \cos(\alpha_{st})\cos(\gamma_{st})z_{se} + z_{st} + \sin(\beta_{rt})x_{re} - \cos(\beta_{rt})\cos(\gamma_{rt})z_{re} - z_{rt} \end{aligned} \quad (6.11)$$

where all variables with the subscript “st” denote emitter TAS parameters (the TAS holding the emitter transducer element), subscript “rt” denotes receiver TAS parameters (all in the USCT coordinate system). The subscripts “se” and “re” denote emitter element and receiver element parameters in the TAS coordinate systems.

As in the ITE approach, we have vectors of the computed and measured time-of-arrival values for each emitter-receiver pair $CTOA_p$ and $MTOA_p$, except that now, $CTOA_p = CTOA_p(\mathbf{x})$ is a function of the newly defined vector $\mathbf{x} = [\mathbf{x}_t, \boldsymbol{\tau}_s, \boldsymbol{\tau}_r]$ of all the TAS parameters $x_T = [x_t, y_t, z_t, \alpha_t, \beta_t, \gamma_t], t \in T$ and all emitter and receiver time delays $\boldsymbol{\tau}_S = [\tau_s], s \in S$ and $\boldsymbol{\tau}_R = [\tau_r], r \in R$. We can now again define the calibration problem as: *Find the vector \mathbf{x} such that the norm of difference between $CTOA_p$ and $MTOA_p$ is minimized.* The definition of the to-be-minimized residual (6.2) remains the same.

Because $CTOA_{sr}$ in (6.11) is a nonlinear function of the unknown TAS parameters, the Gauss-Newton method (6.3) and (6.4) is again used to solve the nonlinear system of equations. While the definition of the residual (6.5) remains the same as in the ITE approach, the elements of the Jacobian matrix (6.6) will be different than in (6.7). The only non-zero elements

of the Jacobian in one row (corresponding to a particular emitter-receiver pair) are the partial derivatives of the residual f_{sr} with respect to the parameters of the corresponding emitter and receiver TASes, and the emitter and receiver element time-delay parameters:

$$\begin{aligned}
\frac{\partial f_{sr}^k}{\partial \alpha_{st}^k} &= \left(D_x^k (-\sin(\alpha_{st}^k) \cos(\beta_{st}^k) x_{se} + (-\sin(\alpha_{st}^k) \sin(\beta_{st}^k) \cos(\gamma_{st}^k) + \cos(\alpha_{st}^k) \sin(\gamma_{st}^k)) z_{se}) \right. \\
&\quad + D_y^k (\cos(\alpha_{st}^k) \cos(\beta_{st}^k) x_{se} \\
&\quad \left. + (\cos(\alpha_{st}^k) \sin(\beta_{st}^k) \cos(\gamma_{st}^k) + \sin(\alpha_{st}^k) \sin(\gamma_{st}^k)) z_{se} \right) / R^{kv} \\
\frac{\partial f_{sr}^k}{\partial \beta_{st}^k} &= \left(D_x^k (-\cos(\alpha_{st}^k) \sin(\beta_{st}^k) x_{se} + \cos(\alpha_{st}^k) \cos(\beta_{st}^k) \cos(\gamma_{st,0}^k) z_{se}) \right. \\
&\quad + D_y^k (-\sin(\alpha_{st}^k) \sin(\beta_{st}^k) x_{se} + \sin(\alpha_{st}^k) \cos(\beta_{st}^k) \cos(\gamma_{st}^k) z_{se}) \\
&\quad \left. + D_z^k (-\cos(\beta_{st}^k) x_{se} - \sin(\beta_{st}^k) \cos(\gamma_{st}^k) z_{se}) \right) / R^{kv} \\
\frac{\partial f_{sr}^k}{\partial \gamma_{st}^k} &= \left(D_x^k (-\cos(\alpha_{st}^k) \sin(\beta_{st}^k) \sin(\gamma_{st}^k) + \sin(\alpha_{st}^k) \cos(\gamma_{st}^k)) z_{se} \right. \\
&\quad + D_y^k (-\sin(\alpha_{st}^k) \sin(\beta_{st}^k) \sin(\gamma_{st}^k) + \cos(\alpha_{st}^k) \cos(\gamma_{st}^k)) z_{se} \\
&\quad \left. + D_z^k \cos(\beta_{st}^k) \sin(\gamma_{st}^k) z_{se} \right) R^{kv} \\
\frac{\partial f_{sr}^k}{\partial x_{st}^k} &= D_x^k / R^{kv}, \quad \frac{\partial f_{sr}^k}{\partial y_{st}^k} = D_y^k / R^{kv}, \quad \frac{\partial f_{sr}^k}{\partial z_{st}^k} = D_z^k / R^{kv}, \quad \frac{\partial f_{sr}^k}{\partial \tau_s^k} = 1,
\end{aligned} \tag{6.12}$$

and

$$\begin{aligned}
\frac{\partial f_{sr}^k}{\partial \alpha_{rt}^k} &= D_x^k (\sin(\alpha_{rt}^k) \cos(\beta_{rt}^k) x_{re} - (-\sin(\alpha_{rt}^k) \sin(\beta_{rt}^k) \cos(\gamma_{rt}^k) + \cos(\alpha_{rt}^k) \sin(\gamma_{rt}^k)) z_{re}) \\
&\quad + \left(D_y^k (-\cos(\alpha_{rt}^k) \cos(\beta_{rt}^k) x_{re} \right. \\
&\quad \left. - (\cos(\alpha_{rt}^k) \sin(\beta_{rt}^k) \cos(\gamma_{rt}^k) + \sin(\alpha_{rt}^k) \sin(\gamma_{rt}^k)) z_{re} \right) / R^{kv} \\
\frac{\partial f_{sr}^k}{\partial \beta_{rt}^k} &= \left(D_x^k (\cos(\alpha_{rt}^k) \sin(\beta_{rt}^k) x_{re} - \cos(\alpha_{rt}^k) \cos(\beta_{rt}^k) \cos(\gamma_{rt}^k) z_{re}) \right. \\
&\quad + D_y^k (\sin(\alpha_{rt}^k) \sin(\beta_{rt}^k) x_{re} - \sin(\alpha_{rt}^k) \cos(\beta_{rt}^k) \cos(\gamma_{rt}^k) z_{re}) \\
&\quad \left. + D_z^k (\cos(\beta_{rt}^k) x_{re} + \sin(\beta_{rt}^k) \cos(\gamma_{rt}^k) z_{re}) \right) / R^{kv} \\
\frac{\partial f_{sr}^k}{\partial \gamma_{rt}^k} &= \left(-D_x^k (-\cos(\alpha_{rt}^k) \sin(\beta_{rt}^k) \sin(\gamma_{rt}^k) + \sin(\alpha_{rt}^k) \cos(\gamma_{rt}^k)) z_{re} \right. \\
&\quad + D_y^k (-\sin(\alpha_{rt}^k) \sin(\beta_{rt}^k) \sin(\gamma_{rt}^k) - \cos(\alpha_{rt}^k) \cos(\gamma_{rt}^k)) z_{re} \\
&\quad \left. + D_z^k \cos(\beta_{rt}^k) \sin(\gamma_{rt}^k) z_{re} \right) / R^{kv} \\
\frac{\partial f_{sr}^k}{\partial x_{rt}^k} &= -D_x^k / R^{kv}, \quad \frac{\partial f_{sr}^k}{\partial y_{rt}^k} = -D_y^k / R^{kv}, \quad \frac{\partial f_{sr}^k}{\partial z_{rt}^k} = -D_z^k / R^{kv}, \quad \frac{\partial f_{sr}^k}{\partial \tau_r^k} = 1
\end{aligned} \tag{6.13}$$

where the D_x^k, D_y^k, D_z^k, R^k are defined as follows:

$$\begin{aligned}
D_x^k &= \cos(\alpha_{st}^k) \cos(\beta_{st}^k) x_{se} + (\cos(\alpha_{st}^k) \sin(\beta_{st}^k) \cos(\gamma_{st}^k) + \sin(\alpha_{st}^k) \sin(\gamma_{st}^k)) z_{se} + x_{st}^k \\
&\quad - \cos(\alpha_{rt}^k) \cos(\beta_{rt}^k) x_{re} - (\cos(\alpha_{rt}^k) \sin(\beta_{rt}^k) \cos(\gamma_{rt}^k) + \sin(\alpha_{rt}^k) \sin(\gamma_{rt}^k)) z_{re} - x_{rt}^k \\
D_y^k &= \sin(\alpha_{st}^k) \cos(\beta_{st}^k) x_{se} + (\sin(\alpha_{st}^k) \sin(\beta_{st}^k) \cos(\gamma_{st}^k) - \cos(\alpha_{st}^k) \sin(\gamma_{st}^k)) z_{se} + y_{st}^k \\
&\quad - \sin(\alpha_{rt}^k) \cos(\beta_{rt}^k) x_{re} - (\sin(\alpha_{rt}^k) \sin(\beta_{rt}^k) \cos(\gamma_{rt}^k) - \cos(\alpha_{rt}^k) \sin(\gamma_{rt}^k)) z_{re} - y_{rt}^k \\
D_z^k &= -\sin(\beta_{st}^k) x_{se} + \cos(\beta_{st}^k) \cos(\gamma_{st}^k) z_{se} + z_{st}^k + \sin(\beta_{rt}^k) x_{re} - \cos(\beta_{rt}^k) \cos(\gamma_{rt}^k) z_{re} - z_{rt}^k \\
R^k &= \sqrt{(D_x^k)^2 + (D_y^k)^2 + (D_z^k)^2}
\end{aligned} \tag{6.14}$$

In each iteration of the Gauss-Newton method, these rather lengthy equations are used to calculate the Jacobian \mathbf{J} , which is then used in (6.3) thus defining the linearized equation

system for Δx . The vector of the estimated parameters is then updated in (6.4). After convergence, the needed positions of the individual transducer elements can be calculated based on the calibrated TAS positions and orientations (6.10).

The number of emitter-receiver pairs in the TAS approach is the same as in the ITE approach and therefore the number of equations remains unchanged. However, the number of variables is: $V = 6U + M + N$, where U, M, N are the numbers of TASes, emitters, and receivers respectively. In the current Karlsruhe USCT set up there are 48 TASes in 3 layers (16 in each layer), thus $V = 6 \cdot 48 + 384 + 1536 = 2,208$.

Compared to the ITE approach, where $V = 7,680$, the TAS approach significantly reduces the number of unknowns while maintaining the same number of equations. This means the calibration solution is much less prone to errors due to noisy data.

In Figure 6-4 a sparsity pattern of the system matrix is displayed for TAS approach (again only a limited system matrix for about 500 equations solving a 2D system is shown). If compared against the system matrix for the same 2D calibration problem Figure 6-2, we can see that the matrix is not as wide (has less columns) because there is much less unknowns. The TAS system matrix is still very sparse – there are only 14 nonzero elements per row. Similar requirements for storing the matrix in a sparse format and using fast algorithms optimized for calculating with sparse matrices apply as in the ITE approach.

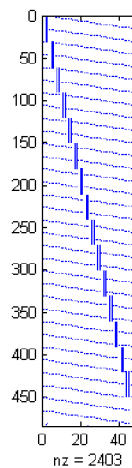


Figure 6-4: Sparsity pattern of the system matrix using the TAS approach.

6.2 Anchoring

In order to obtain a unique solution of the nonlinear calibration problem by either of the two approaches (ITE or TAS), we have to introduce some constraints. With the calibration, we are seeking the positions and individual time-delays of the transducers based only on the time-of-flight measurements. No information is provided on the position and orientation of the USCT transducers relative to a particular coordinate system, in contrast to the GPS case, where a reference coordinate system is defined by the known positions and time-delays of the satellites.

Consequently, the USCT equation system matrix is rank deficient (the rank is always 7 less than the full rank – one for each degree of freedom (three translational degrees, three rotational degrees, and one time degree) and even though the system of equations is heavily over-determined, it has an infinite number of solutions.

6.2.1 Position anchoring

To obtain a single solution, we can constrain the system of equations by introducing virtual “anchors” – reference points, defining the coordinate system of the solution.

In the conceptually simpler ITE case, we can for example anchor the emitter element #1 to the origin of the coordinate system: $s_1: \{0,0,0\}$ by setting the x , y , and z coordinates of s_1 to zero in the initial estimate \mathbf{x}^k , $k = 0$. To insure that the position of s_1 is not altered by the least squares solution, we must add an equation, one for each coordinate, expressing the stability of the solution with respect to each error component of s_1 : $\Delta x_{s1} = 0$, $\Delta y_{s1} = 0$, $\Delta z_{s1} = 0$. This leads to adding 3 rows to the Jacobian matrix with all components equal to zero except those matching x , y and z error components of s_1 . The corresponding residual values need to be set to zero.

The three anchors of the s_1 transducer constrain the three translational degrees of freedom of the coordinate system. The three rotational degrees of freedom can be constrained by anchoring other transducers, but only to the extent not constraining their mutual distances. Thus we can anchor only two out of the three coordinates of the transducer $s_2: \{x_{const}, y_{const}, z\}$. This way, the distance between s_1 and s_2 can still be adjusted by solving the least squares problem. To constrain the coordinate system completely, we need to anchor the z coordinate of yet another transducer $s_3: \{x, y, z_{const}\}$.

In the case of the TAS approach we have more options. It is for example sufficient to anchor only one of the TASes, fixing all of its position and orientation parameters (x , y , z , α , β , γ). This anchors all of the 6 spatial degrees of freedom. Alternatively, it is also possible to anchor two or more TASes with a combination of α , β , γ , x , y , and z anchors.

6.2.1.1 Dilution of precision (DOP)

Although it may not be so obvious, the specific combination of x , y , and z (and α , β , γ) parameters and the transducer element positions (the TAS positions) which are chosen to anchor the system greatly influences the overall calibration accuracy. The positions and types of anchors in the novel USCT calibration method play a similar role as the relative positions of the satellites in the GPS positioning method. We can use the so-called dilution of precision (DOP) (see chapter 2.4.1) to evaluate the influence of a specific anchor combination on the accuracy of the calibration, just as is done in GPS. The DOP describes how accurate the calibration will be, given a noisy measurement of the TOAs. It is a scaling factor, which relates the variance of the input variables (the TOA errors) to the variance of the output variables (transducer position and time-delay errors). In order to achieve the lowest possible DOP (and therefore the highest possible calibration accuracy) a numerical study was carried out.

The study consisted in finding the minimum DOP over all possible anchor combinations. In case of the USCT calibration, where more than one transducer is being calibrated (as opposed to the GPS) the DOP is different for each transducer. To evaluate an overall DOP, a mean value of all calibrated transducers' DOPs was chosen as the minimization criterion. The mean dilution-of-precision *MDOP* is defined as

$$MDOP = \sum_i^N \frac{1}{N} DOP_i = \sum_i^N \frac{1}{N} \sqrt{\text{trace}({}^{ii}D)} \quad (6.15)$$

for all calibrated transducers $i \in \{1 \dots N\}$. The ${}^{ii}D$ is a *submatrix* of D (as defined in (2.25)) such that each ${}^{ii}D$ corresponds only to the calibrated parameters of transducer i .

$$D = J^T J = \begin{bmatrix} {}^{11}D & {}^{12}D & \dots & {}^{1N}D \\ {}^{21}D & {}^{22}D & & \\ \vdots & & \ddots & \\ {}^{N1}D & & & {}^{NN}D \end{bmatrix} \quad (6.16)$$

6.2.1.2 Minimizing the DOP for a 2D USCT

First the effects of anchoring on the dilution-of-precision were studied on a simple 2D USCT model. The modeled USCT had 16 emitters and 32 receivers positioned on a circa 20 cm circle. This corresponds to one layer of transducers in the Karlsruhe 3D USCT system developed (see chapter 2.2). In a two-dimensional USCT only the x and y coordinates are the to-be-calibrated parameters. Therefore only three degrees of freedom (two position and one rotation) have to be anchored. The *MDOP* was computed for all combinations of three x and y anchors (x,y,y and x,x,y combinations). Note that each of the three anchors was moved individually to different transducers and therefore the first two {x,y} anchors are not necessarily anchoring the same transducer (as suggested in the previous paragraphs). Actually the optimal anchor combination was found to be:

- x-anchor: emitter-number 5
- y1-anchor: emitter-number 1
- y2-anchor: emitter-number 9

and the optimum *MDOP* = 212,354. A graph showing the dependency of the MDOP on the anchor positions is shown in Figure 6-5 and a scatter plot in Figure 6-6 show the locations of the optimum x and y anchors.

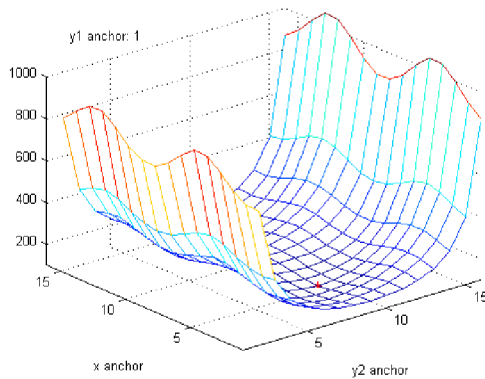


Figure 6-5: Mean dilution-of-precision (*MDOP*) as a function of x and y anchors of different emitter elements (for the ITE approach).

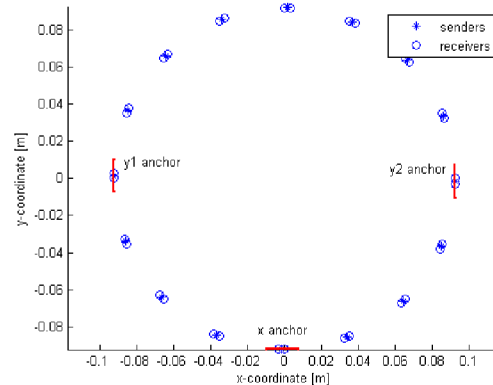


Figure 6-6: Transducer positions of a simulated 2D USCT. The red lines indicate positions of the optimally anchored transducers (for the ITE approach).

A similar search for an optimum anchor combination was done for the TAS approach. First each of the 16 TASes could be individually anchored with α , x, and y anchors. As can be seen in Figure 6-7 the *MDOP* has a number of global minima. Interesting may be that the position of the α anchor doesn't influence the *MDOP*. One of the optimum combinations is:

- α -anchor: TAS-number 1
- x-anchor: TAS-number 1
- y-anchor: TAS-number 5

and the optimum *MDOP* = 80.223 which is considerably lower than the optimal *MDOP* for the ITE approach. *This indicates that the TAS approach will perform much better than the ITE approach when dealing with noisy data.* A scatter plot showing the positions of the optimum anchors is again shown on Figure 6-8.

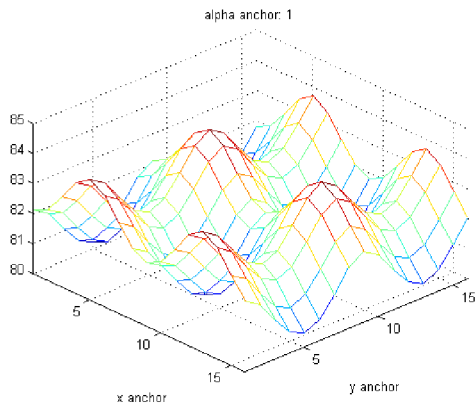


Figure 6-7: Mean dilution-of-precision as a function of x and y anchors (for the TAS approach, α -x-y anchor combination). The position of the α anchor doesn't influence the *MDOP* of different emitter elements.

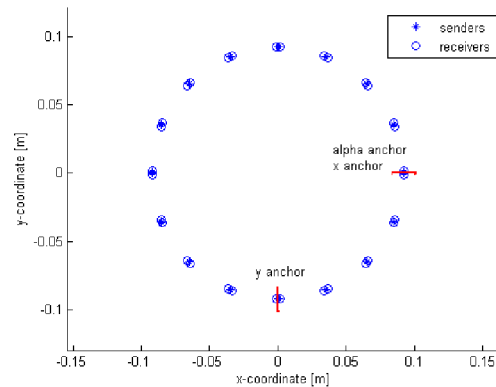


Figure 6-8: Transducer positions of a simulated 2D USCT. The red lines indicate positions of the optimally anchored transducers (for the TAS approach, α -x-y anchor combination).

Similarly a second search has been carried out for the TAS approach, only now each of the 16 TASes could be individually anchored with an x, anchor and two y anchors. The optimum anchor combination was found to be

x-anchor: TAS-number 1

y1-anchor: TAS-number 1

y2-anchor: TAS-number 5

with the minimum *MDOP* = 56.2934. This anchor combination is therefore the one with that will perform the best with noisy data. An *MDOP* function and the scatter plot corresponding to the optimum anchors is again shown in Figure 6-9 and Figure 6-10.

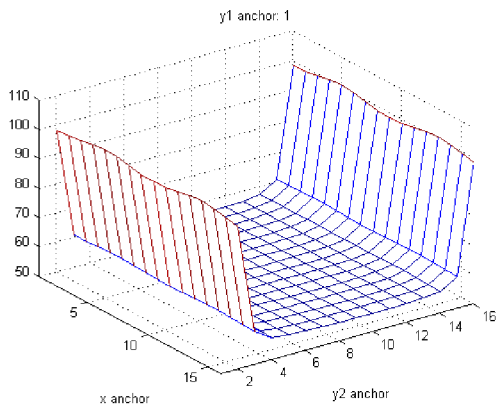


Figure 6-9: Mean dilution-of-precision (*MDOP*) as a function of x and y anchors (for the TAS approach and the x-y-y anchor combination).

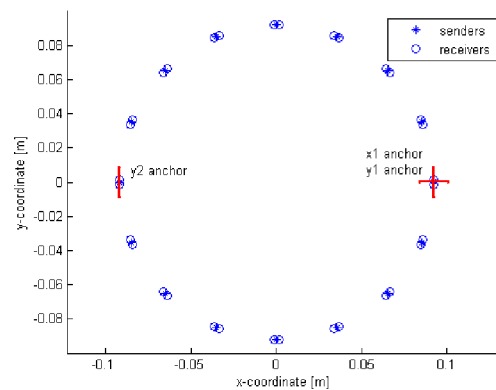


Figure 6-10: Transducer positions of a simulated 2D USCT. The red lines indicate positions of the optimally anchored transducers (for the TAS approach, x-y-y anchor combination).

6.2.1.3 Minimizing the DOP for a 3D USCT

The effects of anchoring on the dilution-of-precision were also studied for a 3D USCT case. Because the total number of possible anchor combinations in the Karlsruhe 3D system $N \approx 5 \cdot 10^{19}$ almost reaches the number of stars in our universe, it would take much too long to

calculate a DOP for each one of them and choose an optimum anchor combination. Also the DOP is a function in the discrete space of transducer positions so a usual optimization can't be used. Instead a more elegant method – a genetic algorithm search [45][46] - was used to minimize the DOP. Although a global minimum is not guaranteed with the genetic algorithm methods, they are proven to converge to a sub-optimum, which is sufficient; it allows a great reduction of computation time.

The modeled 3D USCT had 40 transducers per TAS and 16 TASes in 3 layers in a cylindrical geometry corresponding to the Karlsruhe 3D USCT system. In a 3D system, all six degrees of freedom (3 positions and 3 orientation) have to be anchored. We are therefore seeking a combination of six anchors {x, y, and z} or { α , β , γ , x, y, and z} for the ITE or the TAS approaches respectively.

The genetic algorithm search was performed in Matlab using the Genetic Algorithm and Direct Search Toolbox. The anchors and their positions were encoded into a 42 bit long binary chromosome. The evolving population had 42 individuals ([46] recommends to use about as many individuals as there are bits in the chromosome). The individuals (anchoring combinations) in the initial generation were created as random binary vectors of length 42.

For each individual of the first generation the DOP was calculated and stored. Then, the individuals were sorted by their DOP values from smallest to largest to form a “fitness list”. The individuals higher in this list were more probable to become parents of the individuals in the next generation (children). The children were created by swapping parts of the chromosome of selected individuals (so called “crossover” process). Also random binary noise was added to the children to create mutation children. Two “elite individuals” from the first generation (ones with the smallest DOPs) were copied without any changes into the next generation. This way, the best individuals were guaranteed to be passed into the new generation.

3D USCT - ITE approach anchoring:

First, the genetic algorithm was used to search for the optimum anchor combination of the ITE approach. The results are shown in Figure 6-11. The DOP as a function of all six anchors for the 3D USCT probably has a similar shape as in Figure 6-5 for the 2D USCT – a wide valley with steep slopes on the sides. Inside this valley, the function is almost flat with an insignificant global minimum. That's why a near optimum anchor combination was already present in the randomly created first generation. The genetic algorithm quickly optimized the individuals in a few subsequent generations.

To finalize the optimization, a local stepwise search was performed on the result of the genetic algorithm search. The anchor positions of the best anchor combination were altered in each direction (up or down one layer, or left or right one column of transducers). If a new optimum was reached, the search continued from this new anchor combination. The search stopped when the local minimum was reached.

The optimum 3D anchor combination for the ITE approach is as follows:

Anchor	Emitter layer	Emitter number
x_1	8	12
y_1	1	8
z_1	8	10
x_2	1	4
y_2	8	1
z_2	1	2

The anchors are visualized in figure Figure 6-12. The optimum mean dilution of precision after performing the GA search and the local search got as low as MDOP = 11.4035.

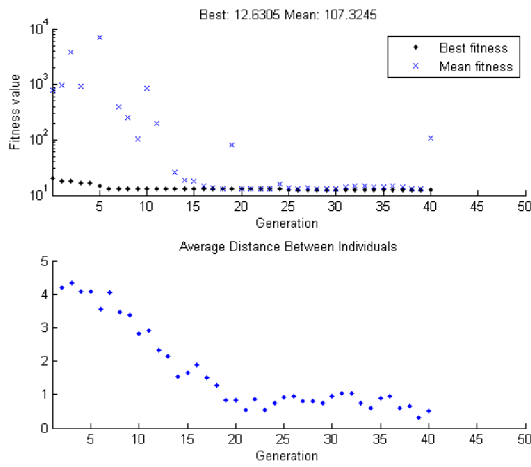


Figure 6-11: The genetic algorithm search (for the ITE approach) for the optimum anchor combination. The upper graph shows the best and mean MDOP (mean dilution-of-precision) values through-out the generations. The lower graph shows the average distance (number of differing bits in the chromosome) between individuals for each generation.

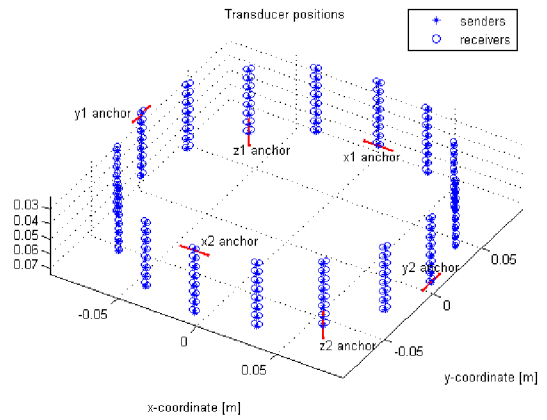


Figure 6-12: Transducer positions of a simulated 3D USCT. The red lines indicate positions of the optimally anchored transducers (for the ITE approach).

3D USCT - TAS approach x - y - z - α - β - γ anchoring:

The same GA search and a finalizing local optimization has been carried out also for the 3D TAS approach. The six anchors were chosen to be in the x , y and z directions and the α , β , γ angles. The optimum anchor combination was found to be:

Anchor	TAS layer	TAS number
x	2	16
y	3	5
z	1	2
α	1	2
β	1	11
γ	1	11

with the MDOP = 9.5521. The GA search curve and the final optimum anchors are visualized in Figure 6-13 and Figure 6-14.

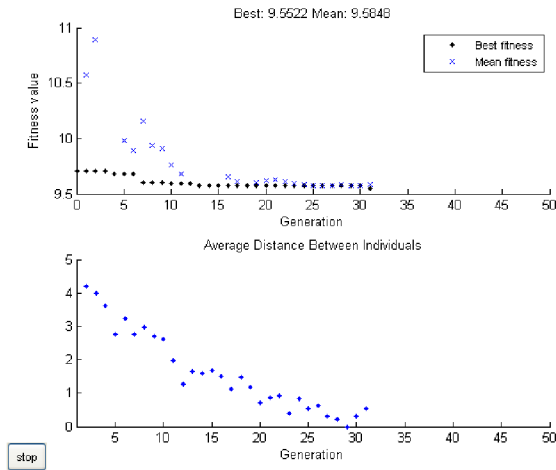


Figure 6-13: The genetic algorithm search (for the TAS approach, x - y - z - α - β - γ anchoring) for the optimum anchor combination. The upper graph shows the best and mean MDOP (mean dilution-of-precision) values through-out the generations. The lower graph shows the average distance (number of differing bits in the chromosome) between individuals for each generation.

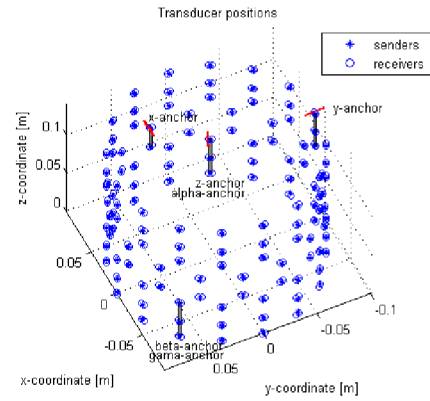


Figure 6-14: Transducer positions of a simulated 3D USCT. The red lines indicate positions of the optimally anchored transducers (for the TAS approach, x - y - z - α - β - γ anchoring).

3D USCT - TAS approach x - y - z - x - y - z anchoring:

And finally the GA search and final local optimization was performed for the 3D TAS approach with x - y - z - x - y - z anchoring. The optimum anchor combination

Anchor	TAS layer	TAS number
x_1	1	4
y_1	2	1
z_1	1	5
x_2	3	5
y_2	2	9
z_2	1	13

yielded an MDOP = 9.6169. The GA search and optimum anchors are visualized in Figure 6-15 and Figure 6-16.

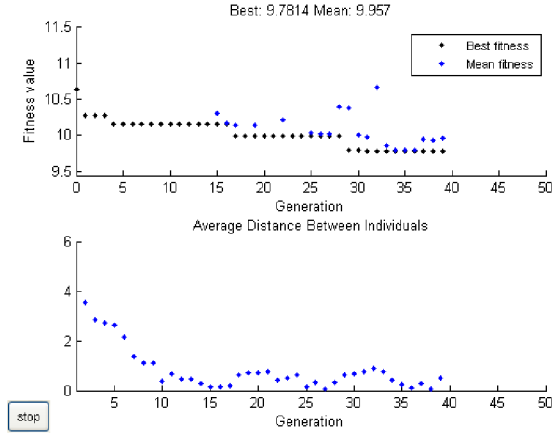


Figure 6-15: The genetic algorithm search (for the TAS approach, x-y-z-x-y-z anchoring) for the optimum anchor combination. The upper graph shows the best and mean MDOP (mean dilution-of-precision) values throughout the generations. The lower graph shows the average distance (number of differing bits in the chromosome) between individuals for each generation.

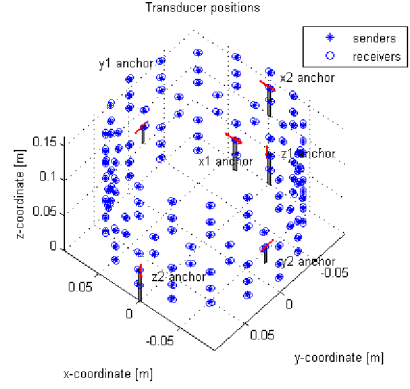


Figure 6-16: Transducer positions of a simulated 3D USCT. The red lines indicate positions of the optimally anchored transducers (for the TAS approach, x-y-z-x-y-z anchoring).

To summarize the position anchoring analysis: it was found that by choosing the right combination of anchors, the possible inaccuracy of the calibration results (quantified in the dilution of precision) can be significantly suppressed for the ITE approach. In the case of the TAS approach, the dilution of precision is not as highly dependent on the correct choice of anchored transducers. The mean dilution-of-precision of the anchored system can reach a minimum of about $MDOP = 10$ for both the ITE and TAS approaches.

6.2.2 Time-delay anchoring

We face a similar problem with the variability of the time-delay parameters. Both $CTOA_{sr}$ definitions (6.1) and (6.11) (for the ITE and TAS respectively) contain a sum of two time delay parameters: the errors of the respective delay and the respective receiver delay. This sum is inseparable: an arbitrary time constant t_{arb} may be added to all emitter delays and subtracted from all receiver delays without influencing the solution of the equation system. The system thus is still rank deficient.

We cannot proceed analogically to the previous case and anchor the delay of one transducer, for example set $\tau_{s1} = 0$, as this would introduce a systematic error. However, we can “anchor” the sum of all emitter delay errors to a constant value, e.g. zero:

$$\sum_i \Delta\tau_{s_i} = 0 \quad (6.17)$$

this way constraining the unlimited number of solutions to only a single one. Although we constrain the system to one solution, the solved delay values will be biased by an unknown quantity t_{arb} :

$$\begin{aligned} \tau_{s_i, \text{solved}} &= \tau_{s_i, \text{true}} + t_{arb}, & \forall i \\ \tau_{r_j, \text{solved}} &= \tau_{r_j, \text{true}} - t_{arb}, & \forall j \end{aligned} \quad (6.18)$$

The solved delay parameters (biased by t_{arb}) can reach physically impossible (negative) values. However, in any single measurement, the TOA of a pulse depends on a sum of the emitter and receiver delays, where t_{arb} vanishes. Thus the sum of an emitter and a receiver delay can be recovered. Even though we are not able to obtain correct values of individual delays

by this calibration approach, but merely the correct emitter-receiver delays sums, it is sufficient, because they always appear in pairs.

6.2.3 The rank deficiency test

A simple verification of the anchoring concept can be made by singular value decomposition, calculating the rank of an equation system – the number of linearly independent equations. The rank can be estimated as the number of singular values of the system matrix, which are larger than some tolerance value (proportional to the machine precision) [46]. The singular values of the Jacobian matrix with and without anchors were plotted in Figure 6-17. We clearly see that the smallest singular values were raised significantly by the inclusion of the anchoring equations to the system – the full column rank was reached.

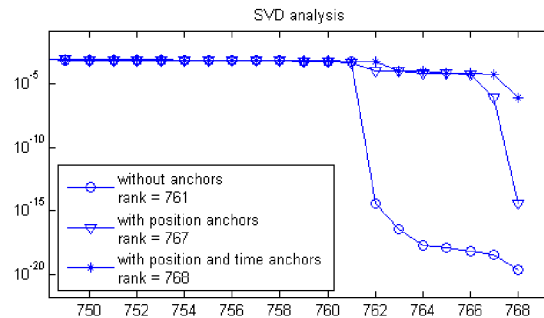


Figure 6-17: SVD analysis of the Jacobian matrix (with 768 columns) matrix with and without anchoring. The singular values were sorted in descending order. The vertical axis is logarithmic and only the last few (smallest) singular values are shown (x-axis is zoomed). With both position and time anchoring, the matrix has a full column rank.

6.3 Numerical analysis and testing

In order to evaluate the method, a simulation study has been carried out based on a virtual model of the 3D USCT system. 64 emitters and 128 receivers in 16 TASes were taken into consideration (about 1/10 of the actual numbers in the Karlsruhe 3D system). This resulted in $N_{un} = (64 + 128) \cdot 4 = 768$ unknown parameters (3 position coordinates and 1 delay per transducer) for the ITE approach and $N_{un} = (64 + 128) + 16(3+3) = 288$ unknown parameters (1 delay per transducer and 3 position and 3 orientation unknowns per TAS) for the TAS approach. The number of simulated TOA measurements was the same for both ITE and TAS approaches $N_{eq} = 64 \cdot 128 = 8192$. The simulations were carried out in Matlab. To solve the equation system (5), the QR-decomposition with pivoting (implemented in the Matlab's backslash operator) was used.

This USCT simulation was used to analyze the convergence properties and the noise sensitivity of the calibration method. Following are the detailed descriptions of the used procedures and outcomes.

6.3.1 Convergence analysis

The typical size of the *region of convergence* was evaluated first. The initial estimate values were derived from the set of simulated ground truth positions and delay values by adding stochastic errors of various magnitudes; then the Gauss-Newton method (6.3) and (6.4) iterated 30 times. Normally a criterion would be established to stop the iterations after the solution has got sufficiently close to the ground truth. In this case it is however also interesting to see the shape of the convergence curve and how close to the ground truth is it possible to

get. The calibration results (root-mean-square differences between the ground-truth positions and outcome of the calibration) for noiseless measurements can be seen in Figure 6-18 for both the ITE and the TAS approaches. The convergence region is surprisingly large – in the magnitude of the diameter of the USCT system (20 cm). Thus, in the absence of noise, a large error in the initial estimate is acceptable.

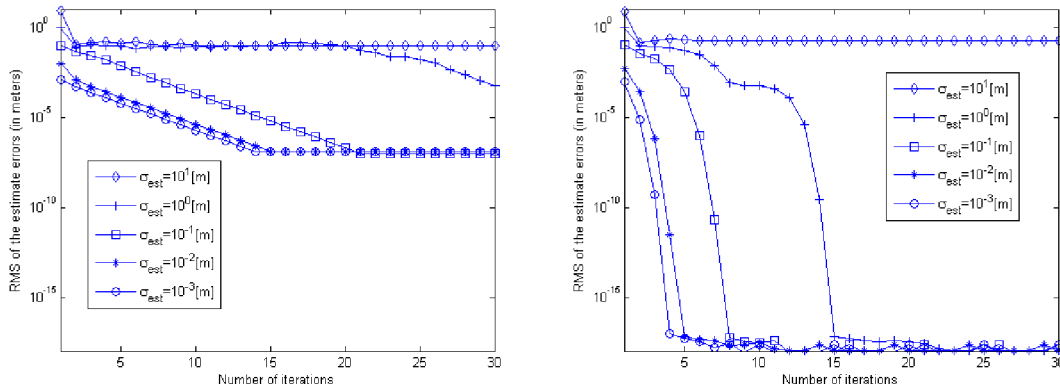


Figure 6-18: Convergence comparison. The plots show the calibration accuracy of the ITE (left graph) and TAS (right graph) calibration approaches. The RMS of the ground-truth errors are plotted for different starting estimates. The standard deviation of the initial estimates is given in the legend (in meters). No measurement noise was assumed. The error RMS is on the vertical axis; the horizontal axis gives the number of iterations.

A rather large difference in the *speed of convergence* and in the *achieved accuracy* between the ITE and TAS approaches can be observed in Figure 6-18. The TAS calibration approach (right graph) converges much faster than the ITE approach (left graph). Also the achieved accuracy of the estimates is much better using the TAS approach.

With simulated noiseless TOA measurements, the accuracy of each calibration approach is limited only by the (im)precision of the used data type (Matlab’s double-precision floating point). Still, the ITE approach cannot achieve accuracy better than about 10^{-7} [m]; on the other hand the TAS approach reaches accuracy of 10^{-18} [m] or better. The reason for this significant difference between the ITE and TAS approach is revealed by the condition number analysis (6.3.2).

To visualize the calibration performance for the ITE and TAS approaches, “error-grams” were created, which graphically provide information about the distribution of TOA errors – differences between estimated and measured time-of-arrivals (Figure 6-19). Note that the ITE calibration is more sensitive to errors on longer emitter-receiver distances. These errors are corrected more throughout the calibration. The TAS calibration approach is on the other hand equally sensitive to long and short distances. Also note that the color scale was adjusted for each image to show the whole dynamic range within an image.

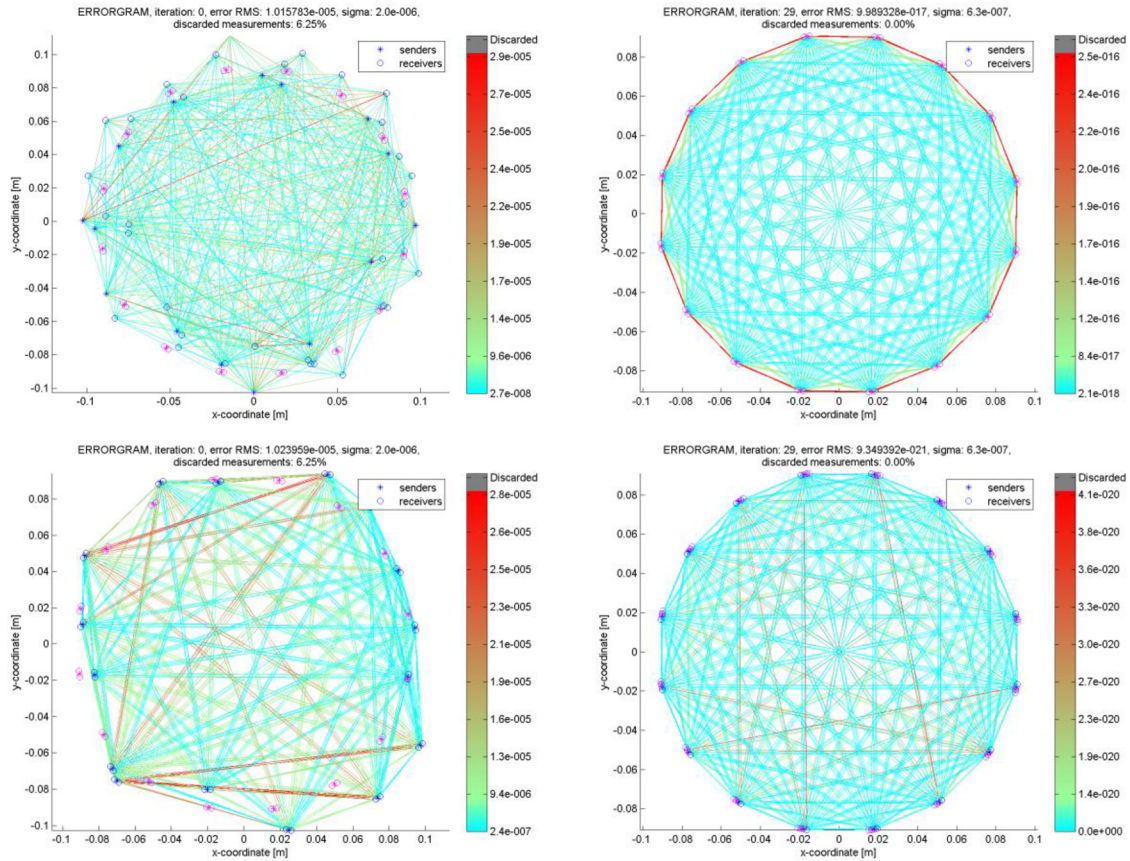


Figure 6-19: Errorgrams, graphically showing the differences between the estimated and measured time-of-arrivals for individual emitter-receiver combinations. Before (top-left) and after (top-right) calibration for the ITE approach and before (bottom-left) and after (bottom-right) calibration for the TAS approach.

6.3.2 Condition number analysis

The condition number of a matrix indicates the sensitivity of a linear equation system solution to errors in the data [46]. A condition number close to 1 indicates a well-conditioned system matrix and a “well-posed” problem. The higher the condition number, the more sensitive the solution is to noise in the data. For high condition numbers, the problem of solving the equation system becomes “ill-posed”.

For the ITE calibration approach, the condition number is dependent on the transducer element positions. If the elements are rather randomly distributed in the space, the position calibration is a well-conditioned problem. On the other hand, if - for example - all of the emitter transducers would lie in a line, the position calibration in the directions perpendicular to the line would be impossible, and the problem would be ill-posed. The cylindrical geometry of the USCT is unfortunately closer to the second case: if the transducer elements lie symmetrically on a perfect cylinder, the condition number is very high. The further we get from this perfect geometry, the lower the condition number gets, and the more well-posed the problem becomes. In contrast, the TAS approach doesn’t show such a behavior. The condition number, although fairly high, stays virtually constant independently on the USCT cylindrical symmetry distortion.

To demonstrate this behavior, the condition number was calculated for different initial position error values for both the ITE and the TAS approaches. The initial position estimates were randomly distributed around the perfect cylindrical (ground truth) positions, with the typical magnitude of the estimate error ranging from one centimeter to one hundredth of a

micrometer in random directions. For each error magnitude value, the initial position estimates were randomly generated one hundred times. Then the system matrix was set up and the condition number was calculated for each of those one hundred random realizations. A mean condition number versus initial error magnitude was then plotted in Figure 6-20

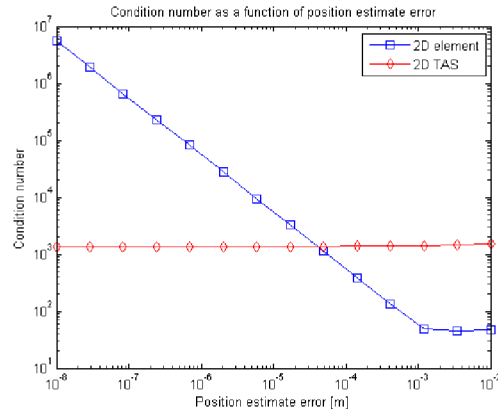


Figure 6-20: System matrix condition number as a function of position estimate error for the ITE and TAS approaches.

The above graph shows that in the ITE approach, the closer are the estimates to the actual transducer positions (lying on the perfect cylinder), the higher is the condition number. In each Gauss-Newton iteration, the position estimates are updated by calculating the estimate error. As this error gets smaller, the system matrix becomes more and more ill-conditioned. That is the main reason why the speed of convergence is slower than in the TAS approach, where the condition number stays constant.

6.3.3 Noise effect analysis

In the previous paragraphs we examined the behavior of both calibration approaches in absence of measurement noise or inaccuracies. Such noise, however, must be expected in a real USCT setup especially in the measurement of the time-of-arrival of a pulse.

The recorded A-Scan, in which the pulse is being detected, is itself noisy due to imperfections of the used equipment. This A-Scan noise prevents us to determine the TOA of a pulse precisely. Moreover, the pulse detection algorithm (to be discussed in 6.5.1) is also inaccurate to a certain extent. Also the speed of sound, calculated from the measured temperature of the water in the USCT tank, is not exact. Besides the inaccuracies of the thermometer and the error of the formula to calculate the speed of sound from the measured temperature, the temperature inside the tank is not fully homogeneous (this topic is discussed in greater detail in chapter 6.5.2).

All these sources of error cause that the calibration method performs somewhat worse than under ideal conditions. The following paragraphs analyze how both the calibration approaches perform in simulated noisy conditions.

To evaluate how the calibration method performs in the presence of noise, the same mathematical model was used for the convergence analysis. The time-of-arrivals of the simulated pulses were calculated according to (6.1) for each emitter-receiver pair. Normal distribution random noise with a preset standard deviation was added to the simulated TOA values. The initial position and delay estimates were again randomly distributed around the ground truth values.

To see the effect of the noise level on the calibration method, the standard deviation of the TOA noise was preset to 5 values ranging from $\sigma_{\text{noise}} = 10^{-9}$ s to $\sigma_{\text{noise}} = 10^{-5}$ s. The calibra-

tion process ran 100 times (with 100 stochastically diversified input data) for each of these preset σ_{noise} values.

The results – median RMS values of calibration errors versus number of iterations - can be seen in Figure 6-21 for both the ITE and TAS calibration approaches. As one can see, the TAS approach performs much better: it converges faster to estimates which are closer to the ground truth

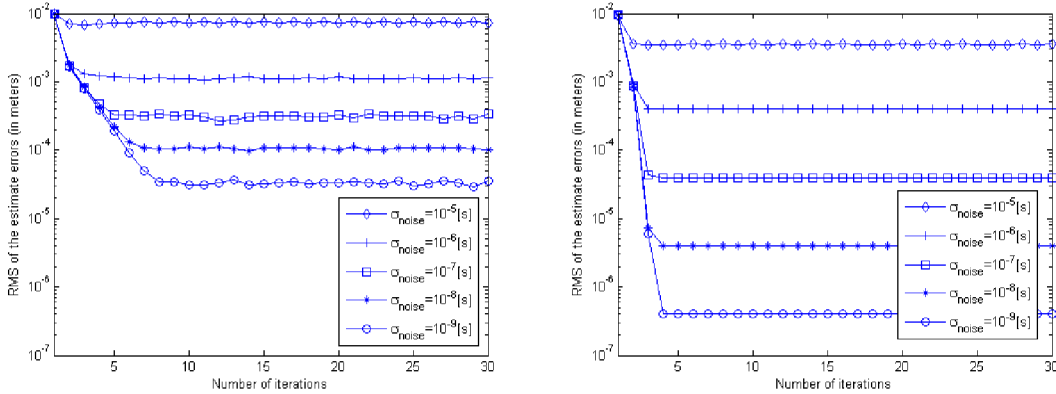


Figure 6-21: Noise effects analysis for the ITE (left) and TAS (right) approaches. The two plots show the calibration accuracy (median RMS of the estimate errors) for different levels (standard deviations) of measurement noise (pulse detection inaccuracies) versus number of iterations. The typical error of the initial estimate was set to 10^{-2} m.

To show the dependency of the calibration accuracy on the TOA noise level, a pair of graphs was plotted in Figure 6-22 - the solid lines show the 95th percentile of the estimate error RMS values after the calibration. They therefore show the expected 95% accuracy of the calibration results in the presence of noise. It can be seen that in order to satisfy the needs of the USCT image reconstruction, requiring transducer position accuracy within a tenth of a millimeter, the pulses must be detected with an error under 10^{-9} s for the ITE approach which is not practically achievable as it corresponds to about 0.003 of the period (at 2.7 MHz). On the other hand, for the TAS approach it is sufficient to detect pulses within $2 \cdot 10^{-7}$ s, i.e. about 2/3 of the period of the corresponding to the used ultrasound wavelength. This precision is more likely achievable in the current USCT setup.

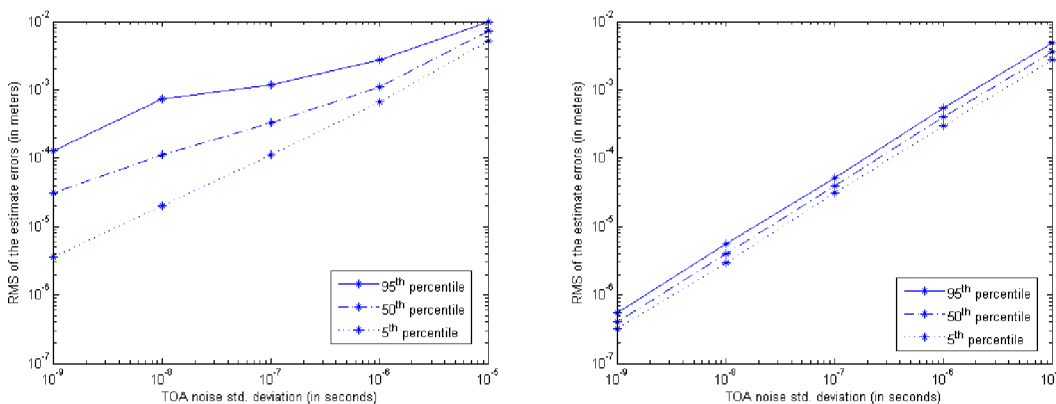


Figure 6-22: Dependency of the calibration accuracy on the TOA noise strength for the ITE (left) and TAS (right) approaches.

The outcome of the simulated USCT calibration (the TAS approach) can be seen in Figure 6-23, where the positions of individual transducers are shown in 3D plots. It can be seen that the calibrated transducers are equally distributed on the surfaces of the TASes forming a cylindrical outline of the USCT tank, as it was modeled in the simulation (only every second TAS from the top TAS layer of the Karlsruhe USCT was part of the model). The first estimate had an RMS error of $\sigma = 10^{-2}$ m, and the measurement noise standard deviation was $\sigma = 10^{-7}$ s. Although the fit of the calibrated transducer positions to the ground-truth is not perfect, the differences are too small (compared to the overall dimensions) to be seen.

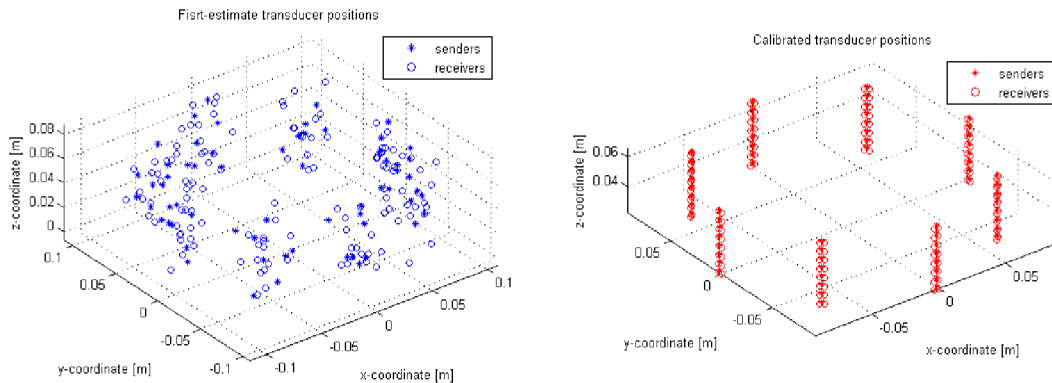


Figure 6-23: Two 3D scatter plots with positions of individual transducers before (left) and after (right) the calibration.

6.4 Alternative solutions to the calibration problem

This chapter gives a few alternative possibilities on how to solve the system of equations yielding the calibrated transducer positions (chapters 6.4.1 and 6.4.2). It also shows how the model of the time-of-arrival can be changed in order to reduce or extend the number of unknowns and their meaning (chapters 6.4.3 and 6.4.4). Finally, it is shown how it is possible to extend the calibration quality by incorporating a calibration phantom in the future (chapter 6.4.5).

6.4.1 The Levenberg-Marquardt algorithm

The Levenberg-Marquardt algorithm (LMA) is an alternative to the Gauss-Newton algorithm (GNA) used in the previous chapters as a method to solve the set of nonlinear equations. The LMA interpolates between the GNA and the method of gradient descent. It is more robust than the GNA which means that in many cases it finds a solution even if the initial estimate is far off from the correct values. On the other hand, for well-behaved functions and reasonable starting parameters, the LMA tends to be somewhat slower than the GNA [53][56][76].

The previously described calibration problem (6.2) can be solved using the LMA method just by converting the equation (6.3) to the following form:

$$(J(x^k)^T J(x^k) + \lambda I) \Delta x^k = -J(x^k)^T f(x^k) \quad (6.19)$$

where \mathbf{I} is the identity matrix and λ is a non-negative damping factor, which is adjusted in each iteration.

If reduction of the residual F_P in (6.2) is rapid, a smaller λ value can be used bringing the algorithm closer to the GNA, whereas if an iteration gives insufficient residual reduction, the λ can be increased providing a step closer to the gradient descent direction. A similar

damping factor appears in Tikhonov regularization, which is used to solve linear ill-posed problems [76].

The choice of the λ - parameter value is the most problematic aspect of this method. In particular, if λ is too high the algorithm tends to suffer from the undesirable properties of the gradient descent method.

The absolute value of any choice depends on how well-scaled the initial problem is. Marquardt himself recommended starting with a reasonable value λ_0 and a factor $\nu > 1$. Initially setting $\lambda = \lambda_0$ and computing the residual sum of squares $S(\mathbf{p})$ after one step from the starting point with the damping factor of $\lambda = \lambda_0$ and secondly with λ/ν . If both of these are worse than the initial point then the damping is increased by successive multiplication by ν until a better point is found with a new damping factor of $\lambda\nu^k$ for some k [56].

If use of the damping factor λ/ν results in a reduction of squared residual then this is taken as the new value of λ (and the corresponding new estimate is accepted). The process then continues. If using λ/ν resulted in a worse residual, but using λ resulted in a better residual, λ is left unchanged and the new estimate is taken as the value obtained with λ as damping factor [56].

6.4.2 The weighted least squares approach

As a modification of the above-described GNA or LMA methods, we have the possibility to give different weights to the equations in the equation set. This is particularly interesting for calibrations using real data.

When dealing with real data, some measurements might have higher quality than others. For example, the time-of-arrival of the first pulse can be detected with much less accuracy in a noisy A-scan than in a an A-scan with a high signal to noise ration. Such a measurement can then be assigned a bigger weight and have a greater influence on the overall result.

Algebra gives us a tool to make such a change. It can be done by calculating the weighted least squares solution, rather than just the plain least squares. The weighted least squares is a preferred choice whenever the uncertainties of the measurements differ. A matrix \mathbf{W} can be constructed, with the main diagonal values $w_{i,i} = 1/\sigma_i^2$ equal to the reciprocal of the measurement variance. The GNA solution (6.3) then becomes

$$\mathbf{J}(\mathbf{x}^k)^T \mathbf{W} \mathbf{J}(\mathbf{x}^k) \Delta \mathbf{x}^k = -\mathbf{J}(\mathbf{x}^k)^T \mathbf{W} \mathbf{f}(\mathbf{x}^k) \quad (6.20)$$

and the LMA solution

$$(\mathbf{J}(\mathbf{x}^k)^T \mathbf{W} \mathbf{J}(\mathbf{x}^k) + \lambda \mathbf{I}) \Delta \mathbf{x}^k = -\mathbf{J}(\mathbf{x}^k)^T \mathbf{W} \mathbf{f}(\mathbf{x}^k) \quad (6.21)$$

It must be noted that the variance of the measurement is usually not known and the weight has to be somehow estimated.

6.4.3 Solution based on a common time-delay parameter

A possible modification to the model of the time-of-arrival of the first pulse in an A-scan is to omit the individual transducer time-delay parameters and leave only one time-delay, common to all transducers. This way the number of unknowns reduces significantly and the system becomes more stable to solve even in the case of very noisy measurements.

In such case the original model of the time-of-arrival (6.1) becomes

$$\text{CTOA}_{\text{sr}}(x_s, x_r) = \frac{\sqrt{(x_s - x_r)^2 + (y_s - y_r)^2 + (z_s - z_r)^2}}{\nu} + 2\tau \quad (6.22)$$

where $\tau = \tau_s = \tau_r$. The multiplication of the time delay by two is caused by the fact that the time-delay is applied twice, once on the emitting side and once on the receiving side.

Instead of having $4M + 4N$ unknowns, where $M = |S|$ is number of emitters, $N = |R|$ is number of receivers (each having coordinates in 3D space and a time-delay parameter) we now have $3M + 3N + 1$ unknowns. The number of equations remains the same.

It is of course a question if the model is still valid after such a simplification and it depends on the actual system and the used transducer properties. The simplification should only be used if it is clear, that the variation of the time-delay parameters among transducers is not significant.

6.4.4 Solution based on angle-dependent common time-delay

This modification of the TOA model extends the one described in the previous chapter. Rather than having a scalar common time-delay parameter, the parameter can be angle dependent

$$\text{CTOA}_{sr}(x_s, x_r) = \frac{\sqrt{(x_s - x_r)^2 + (y_s - y_r)^2 + (z_s - z_r)^2}}{v} + \tau(u_{s \rightarrow r}, \phi_{s \rightarrow r}) + \tau(u_{s \leftarrow r}, \phi_{s \leftarrow r}) \quad (6.23)$$

where $u_{s \rightarrow r}$ and $u_{s \leftarrow r}$ are the emitting and receiving azimuth angles of and $\phi_{s \rightarrow r}$ and $\phi_{s \leftarrow r}$ are the emitting and receiving elevation angles.

The common time-delay is now a function of two variables: the azimuth and elevation angles. Although we cannot solve for an arbitrary unknown continuous function in an equation set, we can sample the function and solve for the scalar samples

$$\text{CTOA}_{sr}(x_s, x_r) = \frac{\sqrt{(x_s - x_r)^2 + (y_s - y_r)^2 + (z_s - z_r)^2}}{v} + \tau_{s \rightarrow r} + \tau_{s \leftarrow r} \quad (6.24)$$

If the circular symmetry of the USCT system and the geometrical symmetry of the used transducers allow it, it is then possible to simplify the model assuming that the time-delay function is also symmetrical $\tau_{s \rightarrow r} = \tau_{s \leftarrow r} = \tau_{s \leftrightarrow r}$, and the model becomes

$$\text{CTOA}_{sr}(x_s, x_r) = \frac{\sqrt{(x_s - x_r)^2 + (y_s - y_r)^2 + (z_s - z_r)^2}}{v} + 2\tau_{s \leftrightarrow r} \quad (6.25)$$

Although the angle-dependency of the time-delay is not easily justifiable as a valid attribute in the TOA model it outperformed other models when dealing with the Karlsruhe USCT data (see chapter 6.5.3).

6.4.5 Theoretical extension to a thread-phantom-based calibration

To achieve greater accuracy of the calibration, a phantom consisting of several thin threads can be inserted inside the USCT tank during the measurement of the calibration data. In such case, the recorded A-scans will also contain extra pulses corresponding to the reflection / scattering of the ultrasonic waves on these threads. The time-of-arrival of these pulses can then be used as additional information about the position of the transducers. To correctly utilize this new information, we either have to exactly know the positions of the threads, or (and this is the preferred option) we can solve for the position parameters of the threads just as we solve for the position parameters of the transducers.

The theory of this alternative method of calibration has been fully developed. The phantom was built and several scans were made using the Karlsruhe USCT system. It was unfortunately impossible to implement the method into the calibration software and use it due to the limited time of the doctoral study program.

6.4.5.1 2D thread reflections

In two dimensions, the use of additional pulses' time-of-arrivals obtained from the reflection / scattering of the ultrasonic waves from the threads is a rather straightforward problem. Let us assume a theoretical setup, where we have one emitter element and one receiver

element positioned somewhere on a circular frame of a two-dimensional USCT device. A single-string phantom is crossing the 2D USCT plane exactly in one point (Figure 6-24).

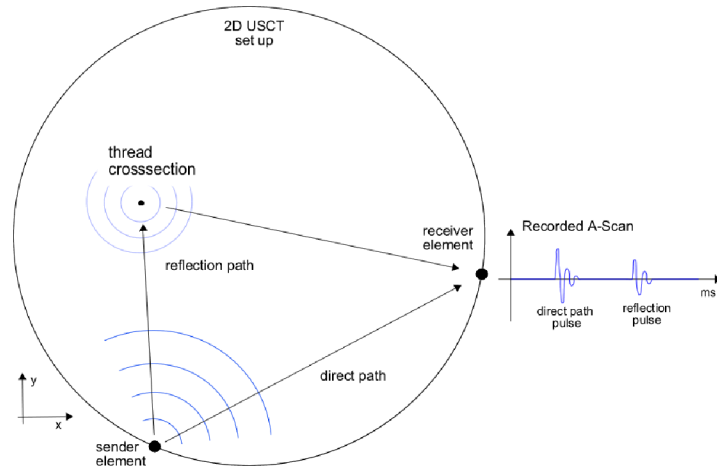


Figure 6-24: 2D USCT set up with a string phantom

An ultrasonic wave emitted from the emitter element will first reach the receiver through a direct path. A pulse will be recorded in the A-scan. After some time the wave reflected from the string will also arrive at the receiver and a second pulse will be recorded. The computed time-of-arrival (CTOA_{sr}) of the first pulse can be expressed by equation (6.1), (for the 2D case the z -axis components need not to be considered) whereas the CTOA of the second pulse can be expressed by the following:

$$CTOA_{\text{thread}}(x_s, x_t, x_r) = \frac{\sqrt{(x_s - x_t)^2 + (y_s - y_t)^2}}{v} + \frac{\sqrt{(x_t - x_r)^2 + (y_t - y_r)^2}}{v} + \tau_s + \tau_r \quad (6.26)$$

where the index t denotes the thread position. As we can see, in this type of equation we have two new unknowns (the x and y coordinates of the thread). There are also not one but two square roots which have to be linearized in the same way as in chapter 6.1.1.

Now let us assume a 2D USCT system with many emitters and receivers and multiple threads crossing the 2D imaging plane. To calibrate the positions of individual transducers, we can set up a system of equations (6.3) and add “reflection path equations” based on (6.26). For each additional thread we gain up to $N_s N_r$ equations (N_s being the number of emitters and N_r the number of receivers), while having to solve only for additional two new unknowns – the x and y coordinates of the thread cross-section. Thus, each thread almost doubles the ratio of equations to unknowns and makes the solution of the system of equations less prone to errors in the measurement data.

Adding many threads also has a disadvantage. Multiple scatterings (which are not accounted for in the model) will occur more frequently. Also the 2D plane becomes more crowded and so situations where a thread would occlude a direct path from an emitter to a receiver would also be more frequent. Even if a thread is not perfectly aligned with an emitter and a receiver, the reflection path is only slightly longer than the direct path and so the two recorded pulses overlap each other. In such situations it is hard to detect the TOAs and distinguish these pulses.

Note that the above text doesn’t deal with possible reflections from other parts of the thread outside of the 2D USCT plane. The thread here is degraded to a mere point, which is an oversimplification. The next paragraphs discuss the situation in a full 3D view.

6.4.5.2 3D thread reflections

In three dimensions the situation becomes more complicated. We have one more dimension to solve the problem in. A line in 3D, with which we can approximate the thread, has

not only 3 position parameters (x,y,z) but also 3 orientation parameters (α,β,γ) . We therefore have to solve for 6 unknowns with each thread inserted into the USCT system.

A much bigger complication comes in determining the point of reflection on the thread for a particular emitter-receiver combination. It is actually the whole length of the thread which produces a mix of reflected and scattered ultrasonic waves when the emitter illuminates the 3D tank with a pulse wave (Figure 6-25).

We can simplify the situation by limiting our selves only to the laws of geometrical optics. In such case a receiver would record a single reflection pulse, with the reflection point in such a part of the thread where the angle of reflection would be equal to the angle of incidence. We can surely assume that such a specular reflection is present, but we cannot omit other diffuse reflections and scatterings from other parts of the thread.

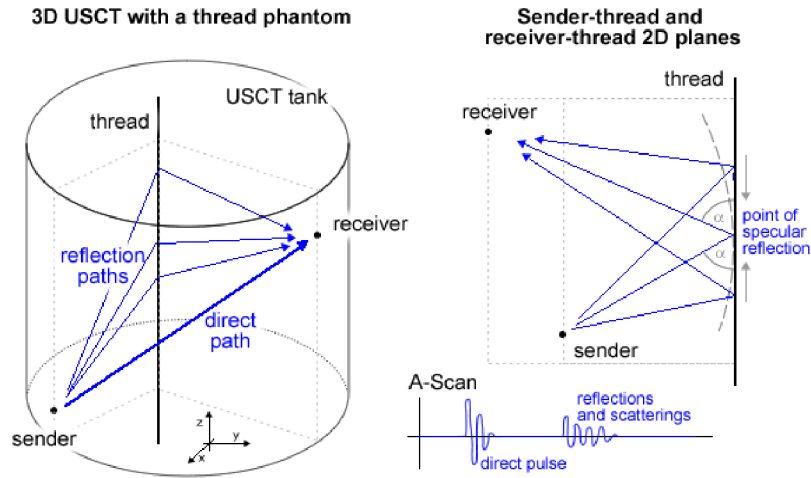


Figure 6-25: 3D USCT set up with a thread phantom

In an A-scan recorded with a thread inside the USCT system, we will find besides the direct path pulse also a series of reflections and scatterings from the thread. To consistently detect a specific TOA, we can detect the TOA of the first pulse in this series of reflection/scattering pulses. The first reflection will always be the one with the shortest path of travel. It happens so, that the shortest reflection path is actually the specular reflection path [55] and so we can assume that we will be able to detect a relatively strong pulse in the beginning of the series.

Now we need to face the problem of finding the reflection point on the thread. As was said earlier, the thread can be geometrically described as a line which has the following parametrical formulation:

$$x_1 = x_0 + at, \quad y_1 = y_0 + bt, \quad z_1 = z_0 + ct \quad (6.27)$$

By changing the parameter t , we obtain the positions of individual points which are located on the line. The length of the reflection path is

$$L = \sqrt{(x_s - x_1)^2 + (y_s - y_1)^2 + (z_s - z_1)^2} + \sqrt{(x_r - x_1)^2 + (y_r - y_1)^2 + (z_r - z_1)^2} \quad (6.28)$$

and with the parameterized line equations (6.27):

$$L = \sqrt{(x_s - x_0 - at)^2 + (y_s - y_0 - bt)^2 + (z_s - z_0 - ct)^2} + \sqrt{(x_r - x_0 - at)^2 + (y_r - y_0 - bt)^2 + (z_r - z_0 - ct)^2} \quad (6.29)$$

we obtain a formulation of the length of a path from an emitter to some point of a line and to a receiver.

We now want to find such a point on the line which will minimize the distance L . Thus we can minimize L with respect to t :

$$\frac{dL}{dt} = 0 \quad (6.30)$$

We proceed by expressing the left side of the equation above

$$\begin{aligned} \frac{dL}{dt} = & \frac{t(a^2 + b^2 + c^2) - a(x_s - x_0) - b(y_s - y_0) - c(z_s - z_0)}{\sqrt{(x_s - x_0 - at)^2 + (y_s - y_0 - bt)^2 + (z_s - z_0 - ct)^2}} \\ & + \frac{t(a^2 + b^2 + c^2) - a(x_r - x_0) - b(y_r - y_0) - c(z_r - z_0)}{\sqrt{(x_r - x_0 - at)^2 + (y_r - y_0 - bt)^2 + (z_r - z_0 - ct)^2}} \end{aligned} \quad (6.31)$$

In order to simplify the notation, we can introduce this notation:

$$\begin{aligned} \alpha &= a^2 + b^2 + c^2 \\ \beta_s &= a(x_s - x_0) + b(y_s - y_0) + c(z_s - z_0) \\ \beta_r &= a(x_r - x_0) + b(y_r - y_0) + c(z_r - z_0) \\ \gamma_s &= (x_s - x_0)^2 + (y_s - y_0)^2 + (z_s - z_0)^2 \\ \gamma_r &= (x_r - x_0)^2 + (y_r - y_0)^2 + (z_r - z_0)^2 \end{aligned} \quad (6.32)$$

We can now use equations (6.31) and (6.32) in (6.30). By putting one of the fractions of (6.31) to the other side and taking the square of the whole equation we arrive at:

$$\frac{t^2\alpha^2 - 2t\alpha\beta_s + \beta_s^2}{t^2\alpha - 2t\beta_s + \gamma_s} = \frac{t^2\alpha^2 - 2t\alpha\beta_r + \beta_r^2}{t^2\alpha - 2t\beta_r + \gamma_r} \quad (6.33)$$

We can now eliminate some terms by expanding the fractions and putting all parts to one side of the equation:

$$\begin{aligned} t^2\alpha[\alpha(\gamma_r - \gamma_s) + \beta_s^2 - \beta_r^2] - 2t[\alpha(\beta_s\gamma_r - \beta_r\gamma_s) + \beta_r\beta_s^2 - \beta_r^2\beta_s] + \beta_s^2\gamma_r \\ - \beta_r^2\gamma_s = 0 \end{aligned} \quad (6.34)$$

The roots of the quadratic equation above are:

$$t_{1,2} = \frac{\alpha(\beta_s\gamma_r - \beta_r\gamma_s) + \beta_r\beta_s(\beta_s - \beta_r) \pm (\beta_s - \beta_r)\sqrt{(\alpha\gamma_r - \beta_r^2)(\alpha\gamma_s - \beta_s^2)}}{\alpha[\alpha(\gamma_r - \gamma_s) + \beta_s^2 - \beta_r^2]} \quad (6.35)$$

Because in (6.33) we took the square of the equation to perform further simplifications, only one of the roots in (6.35) yields a value that meets the minimization criterion. To find out which one of the roots is the correct solution a numerical check has to be preformed.

6.4.5.3 Expressing the TOA equations

We have expressed the parameter t , which gives us the reflection point on the thread. Now we need to use (6.35) in an equation expressing the $CTOA$ of the reflection pulse. For the ITE approach:

$$CTOA_{\text{thread}} = L/v + \tau_s + \tau_r \quad (6.36)$$

where L is the distance of the reflection path as a function of emitter and receiver positions, the thread position and orientation derived in (6.29).

In the presence of strings in the 3D USCT system, we can obtain a measured-time-of-arrival of the reflection pulse $MTOA_{\text{thread}}$ for an emitter-thread-receiver triplet. Let us now define $T = \{t_i, i = 0 \dots V\}$ a set of threads present in the 3D USCT system. Similarly as in 5.1.1

we can organize two comparable vectors of measured and computed time-of-arrival values for *all pulses* (direct and reflected) $MTOA_A$ and $CTOA_A$, where $A = \{(s, t, r)_k, k = 1 \dots W\}$ is a set of triplets $(s, t, r), s \in S, r \in R, t \in T$ such that for each triplet $(s, t, r) \in A$ we can detect the pulse (direct or reflected) in the corresponding A-scan.

The task can again be expressed as: *Find the vector $x = [x_s, x_r, x_t], (s, t, r) \in A$ of unknown positions and delay parameters of all the emitters in S , and receivers in R , and position parameters of all threads in T such that the normed difference between $CTOA_A$ and $MTOA_A$ is minimal.* In other words, minimize a residual F_A :

$$\begin{aligned} \min F_A(x) &= \min \left\{ \frac{1}{2} \|CTOA_A - MTOA_A\|^2 \right\} \\ &= \min \left\{ \frac{1}{2} \sum_{(s,t,r) \in A} (CTOA_{str} - MTOA_{str})^2 \right\} \end{aligned} \quad (6.37)$$

where the minimization runs over the vector of unknown parameters x which is taken as the argument of $CTOA_A$. Note that the definition of the set of threads counts the thread indices from 0. Let the 0th thread in the TOA expressions represent the direct pulses.

We now can use the Gauss-Newton method again to solve the above nonlinear minimization problem.

6.4.5.4 Phantom description

A string phantom was built in the FZK labs based on the authors design. The phantom consists of two circular plastic plates, which are attachable to the bottom and top of the Karlsruhe 3D USCT cylinder tank. When attached to the USCT tank, the plates lie parallel to the cylinder top and bottom bases. In between the plates, one can stretch up to five threads running parallel to the cylinder axis. The threads can only be attached into fixed positions, determined by identical holes drilled into the top and bottom plates. This ensures repeatable measuring results. A technical drawing of the two plastic plates along with string holes can be seen in Figure 6-26.

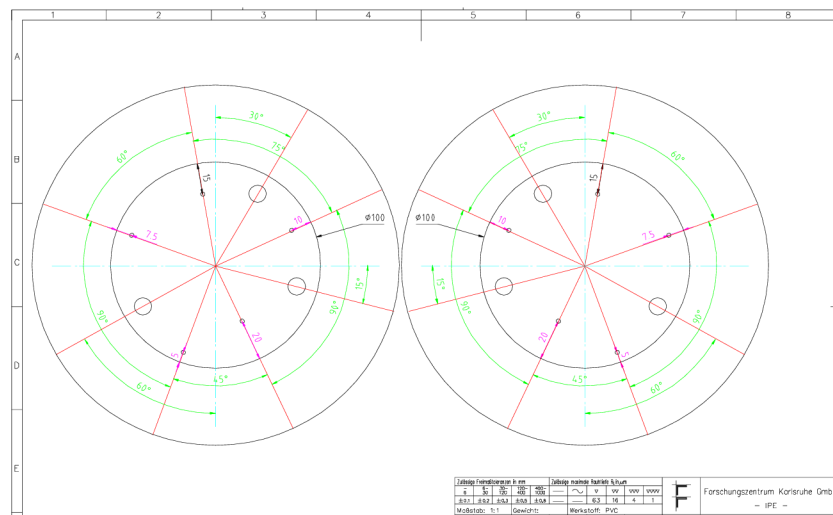


Figure 6-26: Technical drawing of the string phantom top and bottom plates. The largest circles show the size of the USCT tank. The medium circles determine the outline of the plastic plates. Inside these plates are three holes through which the top and bottom plates can be attached and fixed by metal rods during the installation of the phantom into the USCT tank (these rods are taken out of the tank before measurement begins). The small five holes show positions of the threads.

The positions of the threads were intentionally designed not to be symmetrical (with respect to the USCT tank axis). The nonsymmetrical design should limit the cases where the reflected pulses from more than one thread arrive to the receiver element at the same time or very close to each other. In this case it would be very hard to distinguish which recorded pulse corresponds to which reflection path.

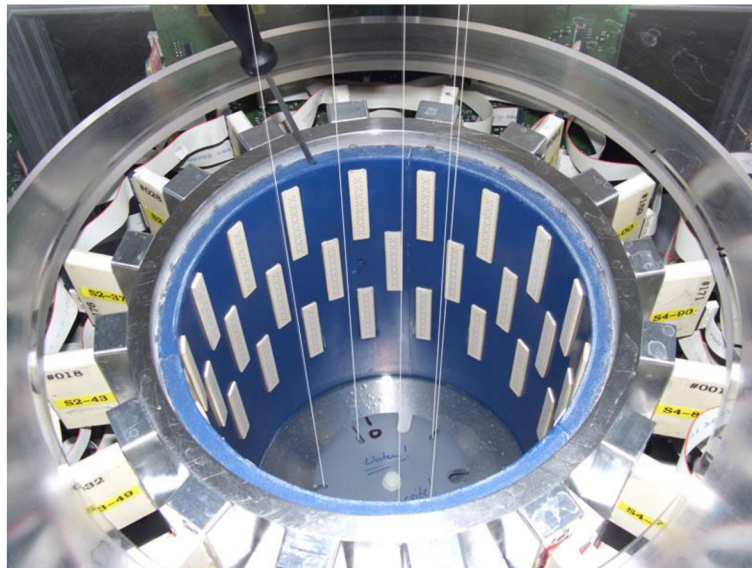


Figure 6-27: Photo of the thread phantom inside the Karlsruhe USCT tank and ready for measurement. Because the original transparent threads are hard to see, white lines were added into the image in their place.

6.5 Position calibration of the Karlsruhe 3D USCT system

To test the proposed position calibration method on real data, several full system scans were made using the Karlsruhe 3D USCT experimental device. For the calibration itself, only an empty scan was needed.

The scanning took about 16 hours. Each A-scan was recorded 32 times and averaged to achieve a better signal-to-noise ratio. The input signal to excite the emitters was the (in Karlsruhe USCT) usually used short pulse with a center frequency at 2.4 MHz and a bandwidth about 2 MHz (see Figure 6-28). To compensate for the possible errors caused by time-variation of the water temperature, the temperature was automatically recorded during the whole period of scanning.

Before the calibration could be applied, the recorded raw data had to be processed to yield the time-of-arrival values – the input of the calibration method. This process was found to be a large topic on its own.

6.5.1 Extracting the TOA from A-scans

So far, the described calibration method worked directly with TOA values, and the process of detecting the time-of-arrival of the ultrasonic pulses has not yet been dealt with. The measured A-scans are fairly noisy signals with several noticeable pulses of various amplitudes and shapes. The following paragraphs show that the problem of extracting the TOA values from the measured A-scans can be split in to two: *pulse detection* and *pulse selection*.

The pulse detection deals with identifying pulses in the A-scan and extracting pulse parameters from the recorded signal: the time-of-arrival, amplitude, and possibly others, e.g. center frequency, bandwidth, etc. Even though the used ultrasonic transducers are smaller than the pulse wavelength, they exhibit a strong angular dependency with one main and two side

lobes (see chapter 3). The angular dependency of the transducers are responsible for both changing the pulse amplitude and pulse shape (different frequency content). Therefore a simple correlation technique is not possible.

The pulse selection on the other hand deals with choosing one of many detected pulses. The objective is to choose the pulse which corresponds to the direct wave path from emitter to receiver. Even in the case of an empty measurement (the cylindrical container is filled only with water as a coupling medium) we can see multiple pulses in one A-scan. Besides the direct path pulse, the receiver element also records waves reflected and scattered from the walls of the container, other transducers, and the water surface. All of these secondary waves arrive later than the one corresponding to the direct path. Other pulses detected by the pulse detection algorithm can originate from mechanical or electrical crosstalk between receivers within one TAS, or simply from false positive detection of background noise.

6.5.1.1 Pulse detection

The pulse detection algorithm used for the Karlsruhe 3D USCT application needs to be very fast since the amount of data per system scan is about 20GB. A simple yet very effective approach is described.

The recorded A-scan is first preprocessed by a de-noising filter. Then by applying the Hilbert transform we obtain a complex analytical signal. By taking the amplitude of this complex signal we can extract an envelope of the filtered A-scan. Next, a smoothing low-pass filter is applied on the envelope to filter out fast changes due to remaining noise. Last, a simple peak detection algorithm is used to find all the peaks in the smoothed envelope signal. The position and the height of these peaks correspond to the TOA and amplitude of the recorded pulses. The above process is graphically represented in Figure 6-28.

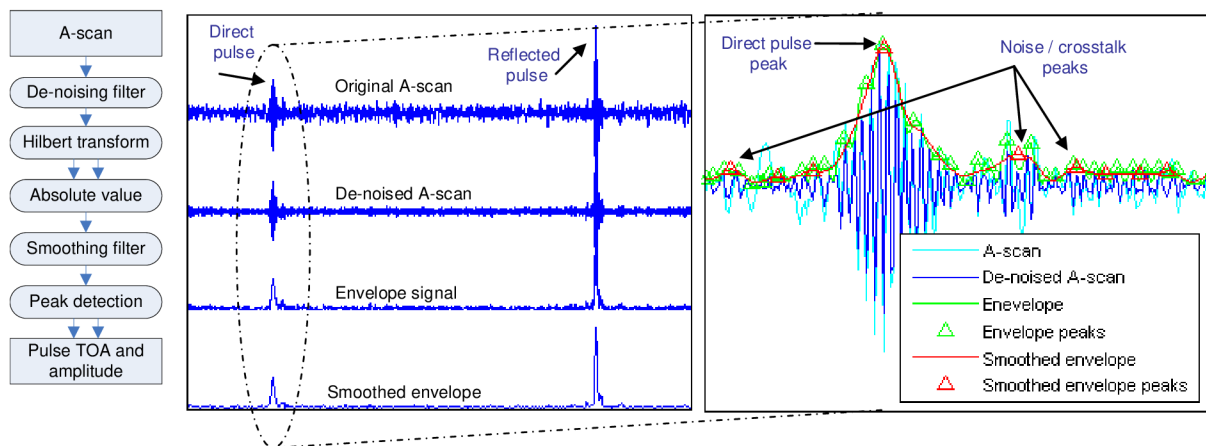


Figure 6-28: The pulse detection algorithm.

The de-noising A-scan filter design was based on the observed differences between the spectrum of the “coded excitation pulse” (input signal used to excite the emitter transducer elements – see chapter 2.2.2) and the spectrum of the recorded A-scans. The usually used coded excitation has a center frequency at 2.4 MHz and a bandwidth about 2 MHz. Figure 6-29 shows the differences in both time-domain and frequency-domain. As can be seen, the recorded signal contains mostly low-frequency noise up to about 1.5 MHz.

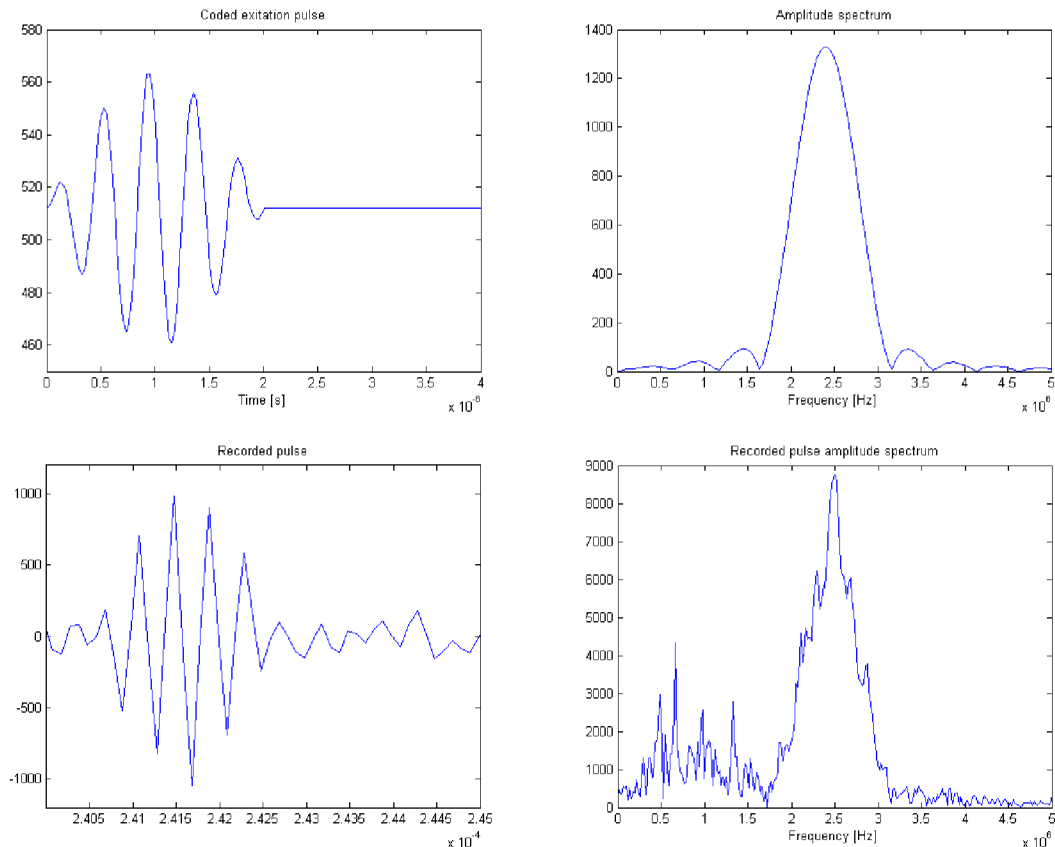


Figure 6-29: The above images show the usually used coded excitation pulse (top-left) and its single-sided amplitude spectrum (top-right). Below them are the recorded pulse and its single-sided amplitude spectrum. Both spectra were calculated after removing the DC component in the signals. Note that the coded excitation pulse is sampled at 40 MHz whereas the A-scans are recorded at 10 MHz.

The de-noising filter was designed to suppress the low-frequency noise introduced by the system. To obtain a sharp transition between the stop and pass bands and to keep the filter down to a reasonable order and thus fast computation, an elliptic IIR filter was used. The downside of the IIR filters is their nonlinear phase characteristic which would change the pulse shape and therefore also the position of the envelope peak. We can cope with this phenomenon by double filtration: first filter the A-scan from left to right, then use the filter from right to left. The phase shifts introduced by the first filtering are zeroed out during the second filtration. This way the A-scan (after being filtered twice) will have a zero-phase shift for all frequencies.

The filter was designed in Matlab's SPTool utility. It is a high-pass elliptic IIR filter of order 8. The lowest pass frequency was set to 1.4 MHz, the stop difference between the pass-band and stop-band is 80 dB or more. Because of the double filtration, the effect of the magnitude response will be squared and any ripples in the pass-band will be pronounced. To minimize this effect the filter was designed to have the maximum variation in the pass-band below 1dB.

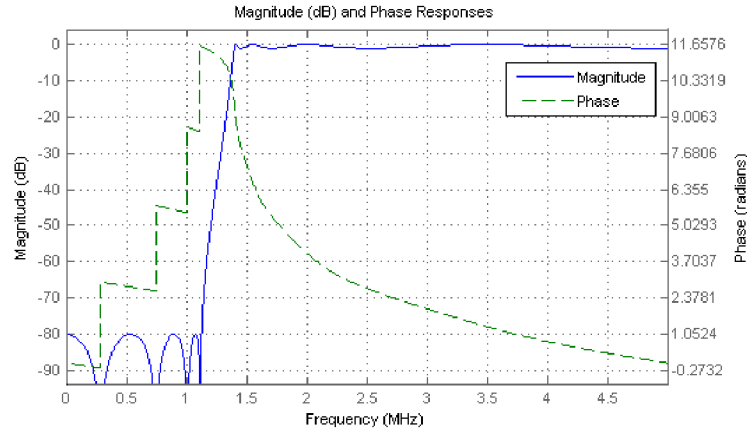


Figure 6-30:

The envelope of the de-noised A-scan is calculated via the Hilbert transform. The signal is first transformed into the Fourier spectrum. After setting the negative-frequency components to zero, the spectrum is transformed back into time-domain. By this procedure a complex analytical signal is created. Now by taking the amplitude of the complex signal, we obtain the envelope of the A-scan.

The smoothing filter was designed as a low-pass Butterworth filter of order 8 with the cut-off frequency at 0.7 MHz. The cut-off frequency was determined experimentally to produce smooth enough envelope signal while maintaining the shape of the pulses. The magnitude and phase response can be seen in Figure 6-31. The filter is again intended to be used by the double filtration process described above. The pass-band magnitude variations were again designed not to exceed 1dB. The nonlinearities of the phase can again be neglected.

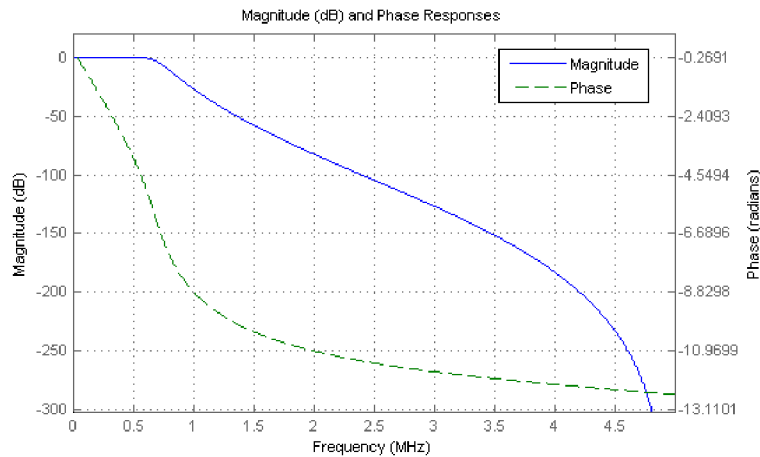


Figure 6-31:

6.5.1.2 Pulse selection

There are several possibilities on how to select the detected pulses ranging from very basic ones e.g. selecting the first detected pulse, to more sophisticated ones which take into account the properties of the pulses or the difference between the expected and measured properties of the pulses.

The first pulse: probably the most intuitive and simplest method is to select the first detected pulse (e.g.: the one with the shortest time-of-arrival), whose amplitude is larger than some predefined threshold. Although it may seem to be very reasonable and works well in a lot of cases, there is a large percentage of A-scans, where this method chooses the wrong pulse. The main sources of errors are: falsely detected pulses in noise (which occur throughout the whole A-scan) and crosstalk pulses (which occur directly before or after strong pulses). It is also hard to set one threshold which would be applicable to all A-scans because the pulse strength changes with the angle of transmission/reception and the noise level differs in each A-scan. An example of correct and wrong selection is displayed in Figure 6-32.

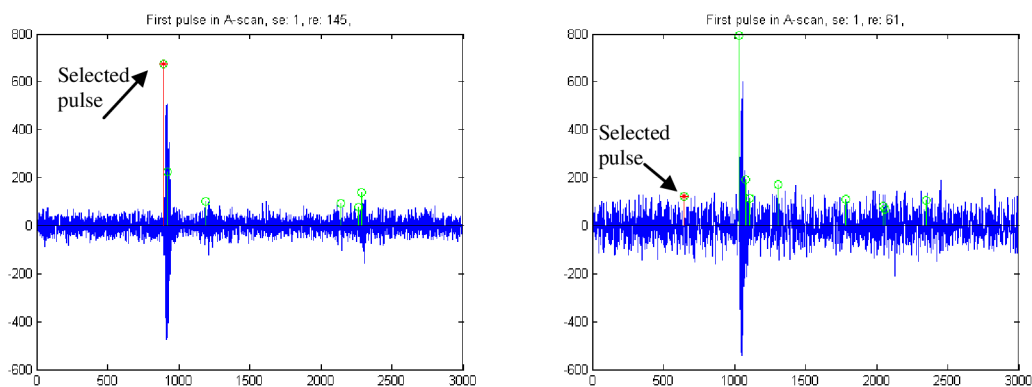


Figure 6-32: The “first pulse” selection method. The method correctly selects the pulse in the left image but wrongly chooses a noise peak in the right image.

The strongest pulse: another simple way to select one of the detected pulses is to use the one with the biggest amplitude. This approach is very insensitive to noise or crosstalk but makes many errors in choosing pulses corresponding to reflections from opposite walls of the USCT tank. This usually occurs in the situations, where the emitter and receiver are very close to each other, the angle of transmission / reception is large, and therefore attenuated a lot by the angular characteristic of the transducers. Reflections from the opposite walls however are much stronger because the transmission / reception angle is near to zero i.e.: at the peak of the main lobe of the angular characteristic. An example of correct and wrong behavior of this pulse selection approach is shown in Figure 6-33.

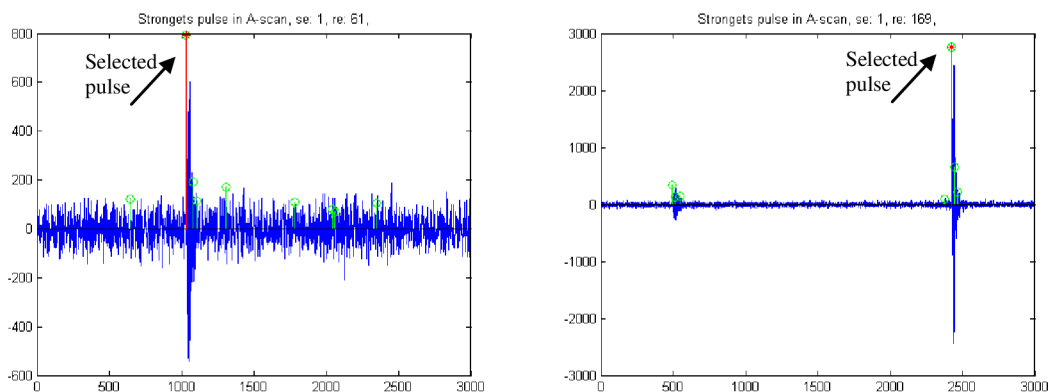


Figure 6-33: The “strongest pulse” selection method. The method correctly ignores noise peaks and selects the direct pulse (image on left) but wrongly chooses a back-wall reflection pulse which has bigger amplitude than the direct pulse (image on right).

The nearest pulse: we also have the possibility to select the nearest pulse to the expected time-of-arrival. This method is significantly less sensitive to falsely choosing noise pulses or reflection pulses, but may suffer from crosstalk pulse selection. A big disadvantage comes from the fact, that the expected TOA is calculated from the transducer position estimates, which are the to-be calibrated unknowns. The first estimates therefore have to be near the true values otherwise the calibration will converge to wrong values or not converge at all.

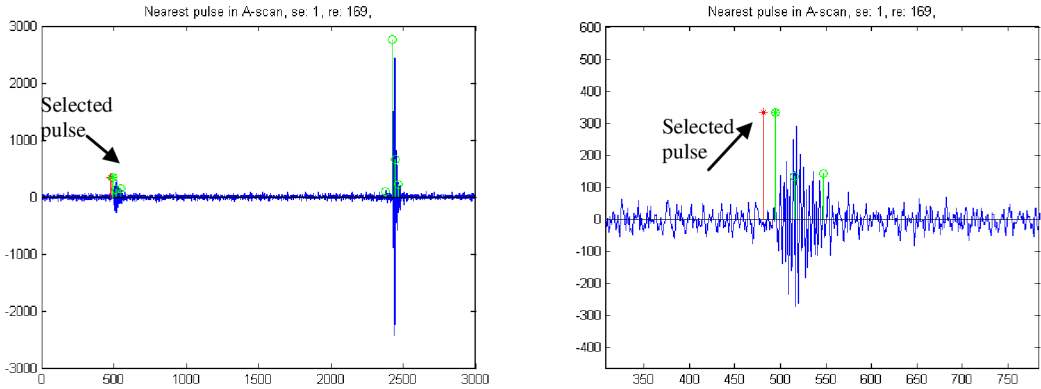


Figure 6-34: The “nearest pulse” selection method correctly selects the direct pulse peak. The whole A-scan (left) and a zoomed area of interest around the direct pulse (right).

In Figure 6-34 displays a situation where the estimated TOA is close enough to the true TOA of the direct pulse wave. On the contrary, Figure 6-35 displays an A-scan where a detected crosstalk/noise peak was closer to the true direct pulse peak.

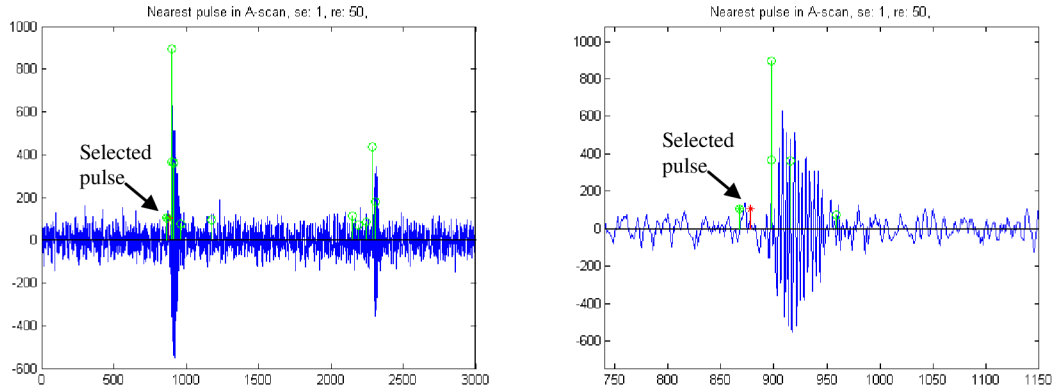


Figure 6-35: Here the “nearest pulse” selection method wrongly selects a crosstalk/noise peak, which was closer to the estimated TOA than the direct pulse peak. The whole A-scan (left) and a zoomed area of interest around the direct pulse (right).

The strongest-nearest pulse: An alternative approach, which proved to be the best, combines “the strongest pulse” and “the nearest pulse” selection approaches. This method chooses the detected pulse which maximizes the product of two quantities: 1) amplitude A_i of the detected pulse and 2) a value p_i expressing the “nearness” of the detected pulse time-of-arrival $TOA_{det,i}$ to the estimated pulse time-of-arrival TOA_{est} :

$$p_i = e^{-\frac{1}{2} \frac{(TOA_{det,i} - TOA_{est})^2}{\sigma_{exp}^2}}$$

$$\operatorname{argmax}_i (p_i \cdot A_i) \quad \left\{ \begin{array}{ll} i, & p_i \cdot A_i \geq \text{noise} \\ \emptyset, & p_i \cdot A_i < \text{noise} \end{array} \right. \quad (6.38)$$

where i is used to index the detected pulses. Note that the nearness function p_i has a form of a Gaussian and can be interpreted as probability or likelihood with which we expect to find the detected pulse. This likelihood is on the range from 0 to 1, with 1 being an exact match (estimated and measured TOAs are the same) and growing smaller for pulses farther away from the expected pulse. The σ_{exp} parameter (which sets the width of the Gaussian curve) is the expected standard deviation of the distance between the detected and the estimated TOA values.

The calibration is essentially a process which minimizes the sum of squares of errors (errors being the differences between the measured and estimated TOAs). Only a few outliers (wrong measurements yielding large errors) could significantly alter the outcome of the calibration. Therefore it is important to discard these measurements. A mechanism for discarding very wrong measurements is implicitly included into the “strongest-nearest” pulse selection method. Equation (6.38) states that a pulse is only chosen if the product of the amplitude and the nearness value is greater than the noise level in the signal. In the case that the noise level is not reached, no pulse is chosen and the measurement is discarded. This can occur if the detected pulse is not strong enough, or is far away from the expected pulse, or both. The noise level can be estimated from A-scans recorded with no emitters firing or from the first part of the A-scans before the arrival of the first pulse.

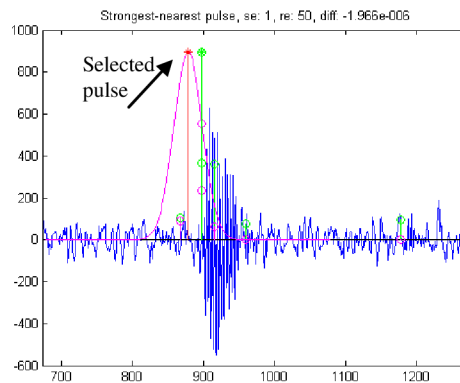


Figure 6-36: The “strongest-nearest pulse” selection method correctly selects the direct pulse peak with higher amplitude even though it is closer to a crosstalk/noise peak.

The approach of the strongest-nearest pulse selection has a hidden risk. All A-scans which have pulses too far from the estimated positions are discarded. In case that the first estimate is far from the true values, the calibration might never converge, or it may converge to wrong results, suiting only the non-discarded measurements.

It is therefore suitable, to start the calibration with a wider Gaussian curve (larger σ_{exp}) allowing for greater uncertainties. We can then reselect the TOAs after every few iterations of the calibration procedure with a narrower Gaussian curve (smaller σ_{exp}). This approach has the advantage that it is not so sensitive to a wrong first estimate and at the same time the outliers are gradually discarded throughout the calibration process.

Another risk involved in the re-selection is that the model of the TOA is not correct in the first place. During the calibration process, the evolving estimates can be driven to wrong results, omitting those measurements which do not adhere to the wrong TOA model. If the

number of discarded measurements is too high, the starting values should be changed or the whole TOA model reconsidered.

6.5.2 Analysis of measurement errors

In this chapter the possible sources of measurement errors are identified. It is discussed how much and in which way these errors affect the calibration.

6.5.2.1 Speed of sound errors

The novel position calibration method assumes the speed of sound of the ultrasonic medium – water – to be known. Because the Karlsruhe USCT setup is maintained in a laboratory environment, this assumption can be valid, but would be very hardly achieved in an application such as the large array underwater imaging system [41]. The main question is how accurately the speed of sound can be estimated.

The velocity of ultrasonic waves in pure water mainly depends on the temperature [24] (water also exhibits dependency on pressure, which can be neglected for the case of a small USCT container – assuming a zero depth, atmospheric pressure in the whole volume). Several scientists (teams) have made very accurate measurements of speed of sound in pure water at various temperatures. After applying a regression analysis, they obtained a polynomial equation which estimates the speed of sound as a function of temperature. Perhaps currently the most used is the Marzcek equation [41], which was calculated based on the combined data of Del Grosso and Mader (1972), Kroebel and Mahrt (1976) and Fujii and Masui (1993) and produced a fifth order polynomial based on the 1990 International Temperature Scale:

$$v(t) = 1.402385 \cdot 10^3 + 5.038813 \cdot t - 5.799136 \cdot 10^{-2} \cdot t^2 + 3.287156 \cdot 10^{-4} \cdot t^3 - 1.398845 \cdot 10^{-6} \cdot t^4 + 2.787860 \cdot 10^{-9} \cdot t^5 \quad (6.39)$$

The Marzcek equation is valid in the range 0-95°C and is accurate to 0.02 m/s.

The speed of sound vs. temperature curve for pure water is shown in Figure 6-37 (top graph). As can be seen, the speed of sound increases with increasing temperature in the interval from 0°C to circa 74°C. For the temperatures above 74°C the speed of sound decreases with increasing temperature. Therefore if we had an option to make measurements at (within some small interval around) 74°C, we wouldn't experience any temperature dependency. Unfortunately measurements at this temperature are not currently possible (and very likely never will be) for the USCT at FZK Karlsruhe.

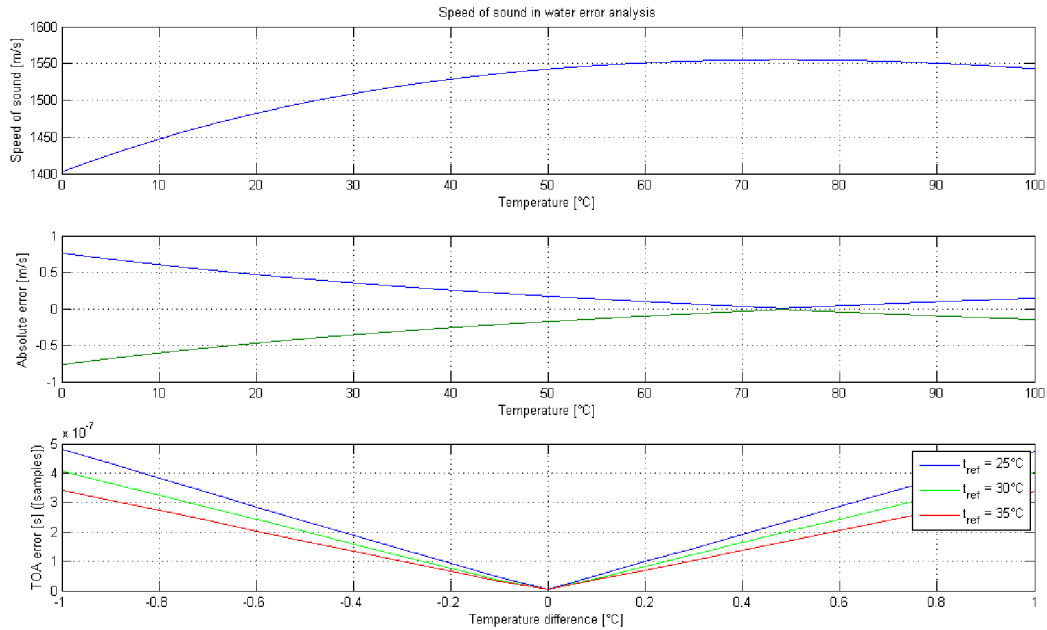


Figure 6-37: The speed of sound as a function of temperature according to the Marczak estimation method (top). Maximum and minimum absolute error of the estimated speed of sound based on temperatures measurements as a function of temperature (middle). Computed time-of-arrival error (in seconds) as a function of measured temperature error for three different water temperatures.

Although there is a different more feasible way how to achieve temperature independency (discussed in chapter 7.2.1), it is at the moment also not possible to test practically on the current USCT system in FZK Karlsruhe. The speed of sound has to therefore be calculated for each A-scan or at least as often as the temperature changes by a detectible amount.

6.5.2.1.1 Thermometer errors

The Marczak equation (6.39) relates the speed of sound to the measured temperature. The error of the temperature measurement therefore directly affects the error of the speed of sound and the whole position calibration. The thermometer used for such measurement in FZK Karlsruhe – the GMH 3750 Greisinger with a calibrated PT100 probe – has an accuracy of 0.07°C . When we put this value into (6.39) we get the accuracy of the calculated speed of sound (the error of the Marczak method 0.02 m/s has to also be added). Because of the nonlinearity of the equation, the error differs for different temperatures. A graph of the accuracy of the speed of sound can be seen in Figure 6-37 (middle).

As anticipated, the error is minimal at 74°C – the zero temperature gradient. Although a measurement at this temperature is not currently realizable, the measurements should be made at the highest possible temperatures as the higher the temperature the higher accuracy of the calculated speed of sound and the whole calibration.

6.5.2.1.2 Temperature variations

Another problem which arose in the USCT setup in FZK Karlsruhe was that the temperature within the USCT tank was not the same. Although the tank is a cylinder of only 20cm in diameter and about 30cm high, the temperature differences were observed to be as high as 0.5°C .

The main differences in temperature were measured to be (as could be expected) between the top and bottom portions of the tank. The main source of heat (when the USCT device is turned on) is from the transducer array systems along the cylinder walls.

Several long measurements of different places in the USCT tank were taken (Figure 6-38) to create a model of the temperature field inside the tank. Although some knowledge of relative temperature field can be deduced from these measurements (Figure 6-39), the behavior of the temperature field was found to be far too complicated to make any firm conclusions within this dissertation.

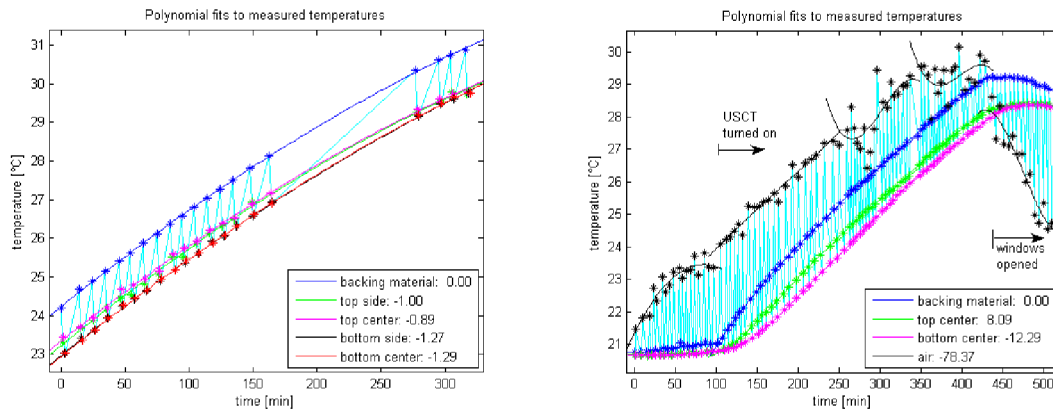


Figure 6-38: Temperatures of water at different places inside the Karlsruhe USCT tank. The left image shows the temperatures in the USCT after it has been turned on for several hours in the same environment. The image on the right shows temperatures developing in a changing environment.

The probe, which measures the temperature during a USCT measurement, is placed inside the “backing material” (layer of damping material along the walls of the USCT). As can be seen, the temperature in the backing material is always about 1°C higher than in the rest of the tank (this is probably due to the better thermal conductivity of the backing material which is pressed against the TASes – the main sources of heat).

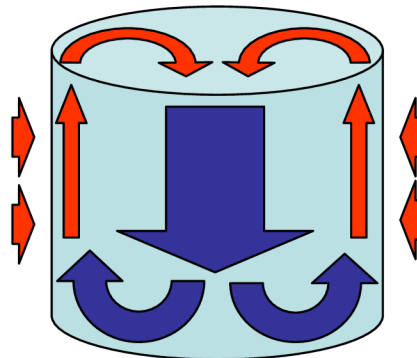


Figure 6-39: Temperature gradient field in the Karlsruhe USCT. The main sources of heat are the TASes along the walls of the cylindrical USCT tank. This image only serves as a main concept based on the authors’ assumptions. Building a precise mathematical model was found to be outside of the scope of this dissertation.

6.5.2.1.3 Error of the speed of sound

Considering all the above, the temperature measurement errors can account for significant errors in the calibration. Figure 6-37 (bottom) shows the relationship of error in measured temperature to error in the computed time-of-arrival (see equations (6.1) and (6.11)) which can then be translated to the error of the whole calibration (see Figure 6-22).

Because of the high attenuation of the ultrasonic transducers at large emitting/receiving angles, measurements with one transducer (e.g. an emitter) at the bottom of the tank and the

other (receiver) at the top of the tank will not be taken into account. Only the measurements within a few transducer layers will be processed for the calibration and here we can expect temperature differences smaller than about 0.2°C. Still this is sufficient to introduce an error of 10^{-7} s in the computed time-of-arrival and therefore an error of $5 \cdot 10^{-5}$ m in the calibrated transducer positions.

6.5.2.2 Thermal expansion errors

With high precision calibration, all aspects effecting the measurements have to be considered. One of these is the thermal expansion of the USCT tank. The whole tank holding the TASes expands with rising temperature. If large changes in temperature are present during the calibration measurement they should be compensated for.

The Karlsruhe USCT tank is a massive cylinder made of stainless steel (Edelstahl V4A, aka. AISI 316L, or X5CrNiMo17-12-2) whose linear thermal expansion coefficient is $\alpha = 16 \cdot 10^{-6} \text{ } ^\circ\text{C}^{-1}$ [46]. The linear thermal coefficient (aka thermal expansion coefficient) is defined as fractional change in length per degree of temperature change:

$$\alpha = \frac{1}{L_0} \frac{\partial L}{\partial T} \quad (6.40)$$

where L_0 is the original length, L the new length, and T the temperature [73]. It relates the change in temperature to the change in a material's linear dimensions.

If an ultrasonic pulse wave travels from an emitter to a receiver the distance $d_{20^\circ\text{C}}$ at 20°C, it will travel the distance d_t at temperature t :

$$d_t = d_{20^\circ\text{C}} + \alpha \cdot (t - 20^\circ\text{C}) \cdot d_{20^\circ\text{C}} \quad (6.41)$$

The thermal expansion at this temperature will be:

$$\Delta d_t = d_t - d_{20^\circ\text{C}} = \alpha \cdot (t - 20^\circ\text{C}) \cdot d_{20^\circ\text{C}} \quad (6.42)$$

and the time-of-arrival error will be:

$$\Delta\text{TOA}_t = \frac{\Delta d_t}{v_t} \quad (6.43)$$

where v_t is the speed of sound at temperature t .

Figure 6-40 displays how the cylinder expands in all directions with rising temperatures. Each point of the tank expands from each other point in the cylinder. The graph on the right shows the magnitudes of the expansion for different n-receiver combinations (different distances) as a function of temperature difference.

In full system scans, which take 10 hours or more, the temperature variations can exceed the 10°C shown on the graph and the thermal expansion errors become significant and should be dealt with.

In short measurements under two to three hours (presently used for the calibration), the temperature variations usually doesn't exceed 5°C and as we can see the resulting errors are not greater than $2 \cdot 10^{-5}$ [m]. As the goal of the calibration is to acquire accuracy of the positions under 10^{-4} [m], this type of error needs not to be considered significant.

Moreover the USCT prototype built in FZK Karlsruhe is planned to be equipped with new data acquisition hardware which should reduce the measurement time to 10 minutes for the whole system scan. The temperature variations (and thus the thermal expansion) during such a short time will be negligible and for this reason the thermal expansion problem is not further discussed in this dissertation.

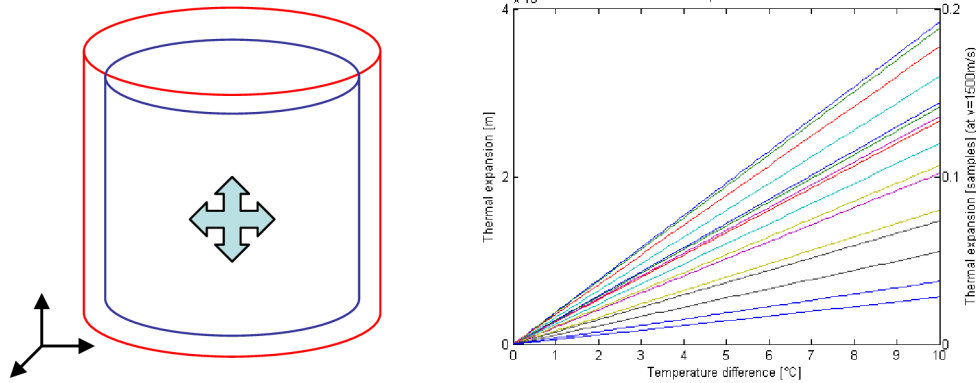


Figure 6-40: The thermal expansion of the Karlsruhe USCT tank. A graphical representation on the left and the dependency of the displacement (in spatial and time domains) on temperature difference for different emitter-receiver combinations (their relative position).

6.5.3 Calibration results based on experimental data

The calibration method was applied to the recorded data in many variations as they were described throughout the whole chapter 6 to test and compare their performance with real data. The calibration was considered as converged when the error root-mean-square (i.e. the RMS of the Δx^k term in (6.4)) dropped below 10^{-6} .

The calibration was implemented in the Matlab programming environment. The computer used was a 2GHz double processor laptop with 4GB RAM running windows XP. Although the code has been partially speed-optimized, it had to be kept very flexible to allow for quick and easy changes of calibration methods throughout the development. If all A-scans would be used for the calibration the computation time would easily reach hundreds of hours. For this reason, and also due to a limited amount of RAM, only the A-scans from every second emitter and receiver of the middle TAS row were considered.

The following paragraphs describe how the different approaches performed.

6.5.3.1 The ITE and the TAS approaches

Most importantly, any attempts to calibrate the Karlsruhe USCT system only succeeded when using the TAS approach. The ITE calibration approach always diverged or converged to nonsense results. The main reasons why TAS outperforms ITE (even if the input data are ideal) are discussed in chapter 6.3. However, the main reason why the ITE method completely fails to give any consistent results are most likely originating in the consistency of the real data. It is the combination the following problems, which the not as robust ITE method is not able to cope with:

- a large percentage of A-scans have to be ignored because the direct signal paths (from the emitter to the receiver) fall outside of the main lobe of the transducers' directivity patterns and the pulses are suppressed by noise
- the TOA values are detected with large errors because the pulses have different shapes and peaks of the pulse envelopes are not always in the middle of the pulse
- the first estimate of the transducer positions is far from the real positions
- there is a bias in the temperature measurements yielding a systematic offset in the computed sound speed values
- the variation of temperature inside the tank is too high

6.5.3.2 Different TOA selection methods

In chapter 6.5.1, the methods of selecting one of the detected peaks in an A-scan yielding the correct time-of-arrival were discussed. Each one of these approaches was used in the calibration algorithm. The results are compared in Table 2.

Table 2: Comparison of calibration performance using different TOA selection methods

	Residual STD	Number of iterations	Computing time
First pulse	NC	NC	NC
Strongest pulse	NC	NC	NC
Nearest pulse	7.944e-7	7	3.16 min
Strongest-nearest pulse	1.727e-7	29 (5 x re-selected)	37.5 min

As can be seen from the table, the first pulse and the strongest pulse methods did not converge at all. The nearest-pulse method converged in 7 iterations, but the standard deviation of the residual (6.2) is higher than the needed. For the TAS method, the goal position accuracy of the transducers - one tenth of a millimeter – is reached when standard deviation of the residual drops below $R = 2 \cdot 10^{-7}$ (see chapter 6.3.3).

The strongest-nearest pulse method worked the best, achieving the smallest residual STD. In fact, when using the strongest-nearest pulse selection approach, a goal residual STD can be set. This goal is achieved by gradually lowering the σ_{exp} parameter (the width of the Gaussian curve) which determines if an A-scan will be selected as a valid measurement or discarded. Each time the σ_{exp} is lowered (after a few iterations, when the error RMS drops below 10^{-6}), the A-scans need to be redetected (using the new position estimates, and the new σ_{exp}). Of course, the parameter cannot be lowered to infinity, as this would result in progressively discarding all measurements.

For the following tests, the strongest-nearest pulse selection method was always used. The important parameter now became the percentage of discarded measurements. A low percentage shows that the calibration algorithm uses a good model of the TOA, and so only a small amount of input data has to be discarded to reach the goal residual.

A last remark to make about the strongest-nearest pulse selection method is that it requires a few re-selections of the pulses in the A-scans during the calibration. This can be a time-consuming procedure, which considerably increases the overall computation time.

6.5.3.3 Alternative calibration solutions

All other described alternatives of the calibration method (see chapter 6.4) were carried out in mutual combinations. Table 3 compares the results. The following list of abbreviations is used:

- GNA – Gauss-Newton algorithm
- LMA – Levenberg-Mardquardt algorithm
- LS – Least-squares solution
- WLS – Weighted least-squares solution
- ND – No delay parameters (only calibrating position parameters)
- CD – Common delay parameter
- ID – Individual delay parameters
- AD – Angular delay parameters

Table 3: Comparison of calibration performance incorporating different methods

Discarded meas. [%] / No. of iterations / Computing time [min]	GNA		LMA	
	LS	WLS	LS	WLS
ND	<u>56</u> / 52 / 49	55 / 58 / 50	54 / 24 / 60	54 / 23 / 66
CD	47 / 37 / 40	47 / 29 / 38	46 / 36 / 55	47 / 55 / 80
ID	NC	NC	44 / <u>72</u> / <u>123</u>	54 / 68 / 102
AD	30 / 26 / 34	30 / 20 / 29	30 / 25 / 45	30 / 24 / 49

The basic model, which computed the position parameters of the TASes and individual delay parameters for the transducer elements (ID) only converged when using the LMA method with the λ reaching very high values. Such a behavior suggests that the shape of the cost function is similar to a long and narrow valley, flat at the bottom. Once the bottom of the valley is reached, the LMA method tends to set higher values of λ , approaching the method of steepest descent. The converging then tends to be very slow.

Alternatively, we can see that the model using only one common delay (CD) instead of individual delays for each transducer, reaches about the same values of discarded measurements in much shorter time. This model also converged using the GNA.

As a reference, the calibration was computed using the ND model - only the position parameters were computed, ignoring the delays completely. As can be seen, this model performed the worst having to discard over 50 % of the A-scans to get to the goal residual.

The best values were surprisingly reached using the AD model – a common angular-dependent delay. Only 30 % of the A-scans were discarded to reach the goal residual. As this could look like a large figure, one has to realize that almost 25% of the recorded A-scans fall into the areas between the main lobe and the side lobes of the used transducers. The peak of the direct pulse in these A-scans is often lost in noise and the measurement is thus useless for the calibration. Another 6.25% represents the A-scans, where the emitter and receiver reside on the same TAS. In such A-scans, the direct pulse is misleading because of high portion of mechanical cross-talk, and is anyway value-less for the geometrical calibration.

Following set of figures (Figure 6-41 to Figure 6-45) shows the histograms of errors (differences of measured TOA and computed TOA values) and errorgrams (a graphical representation of the errors – only the 2D top to bottom projection) before and after calibration for different calibration alternatives.

In the histogram before the calibration (Figure 6-41), several peaks can be seen. None of them is centered on the zero-error. That means that before the calibration, most of the measured TOA values are offset from the computed ones (which are based on the initial geometry and delay estimates) by several wavelengths.

For reference the ND model (calibrating only the position parameters) was included. The calibration centers the histograms' main peak on zero-error but still leaves a lot of errors unaccounted for (Figure 6-42). The calibration tends to converge to a too big diameter of the USCT, compensating for the fact that the delay parameters are not modeled.

The ID model (Figure 6-43) does a slightly better job. The calibrated diameter of the USCT is realistic, but still over 40% of A-scans are discarded to reach the goal residual.

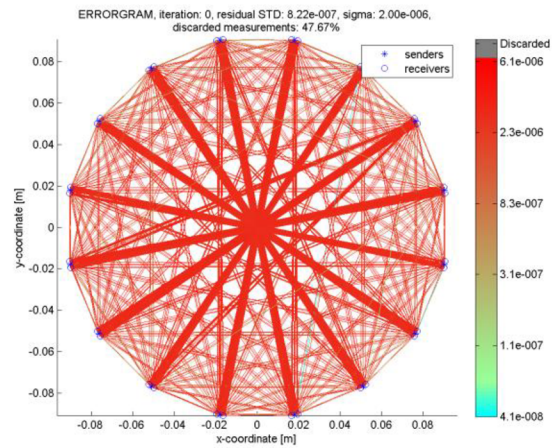
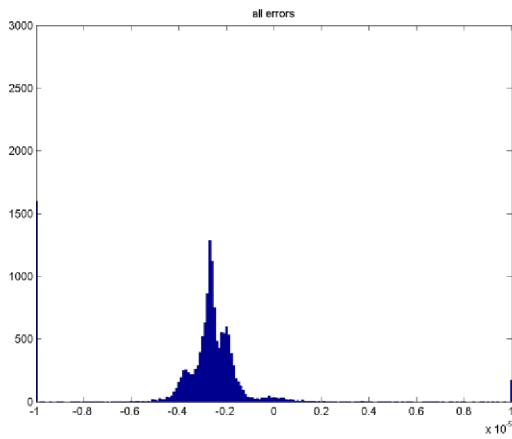


Figure 6-41: Before calibration. Histogram of TOA errors (left) and errorgram – a geometrical representation of TOA errors (right)

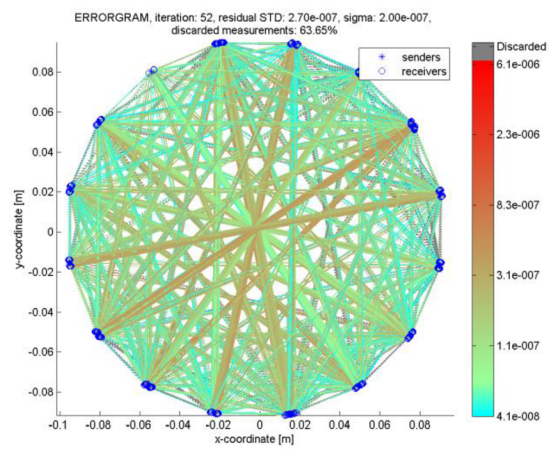
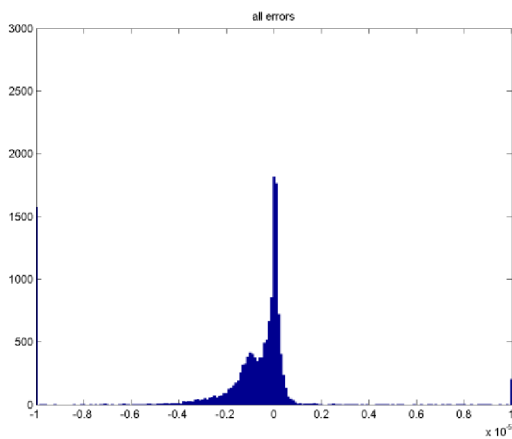


Figure 6-42: After the LMA –WLS – ND calibration. Histogram (left) and errorgram (right)

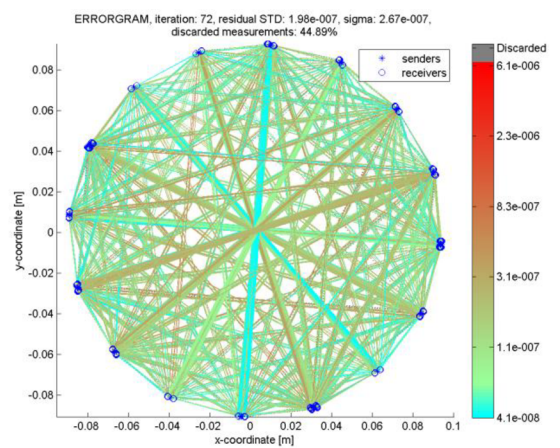
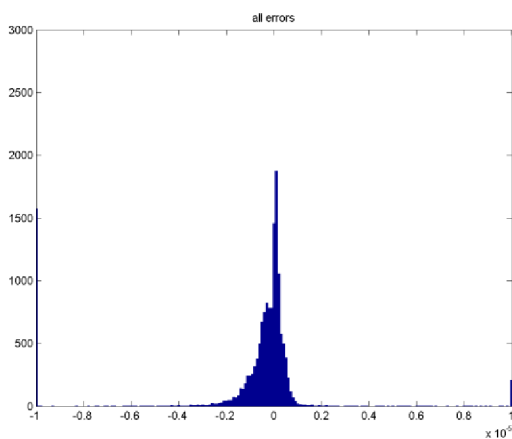


Figure 6-43: After the LMA –LS – ID calibration. Histogram (left) and errorgram (right)

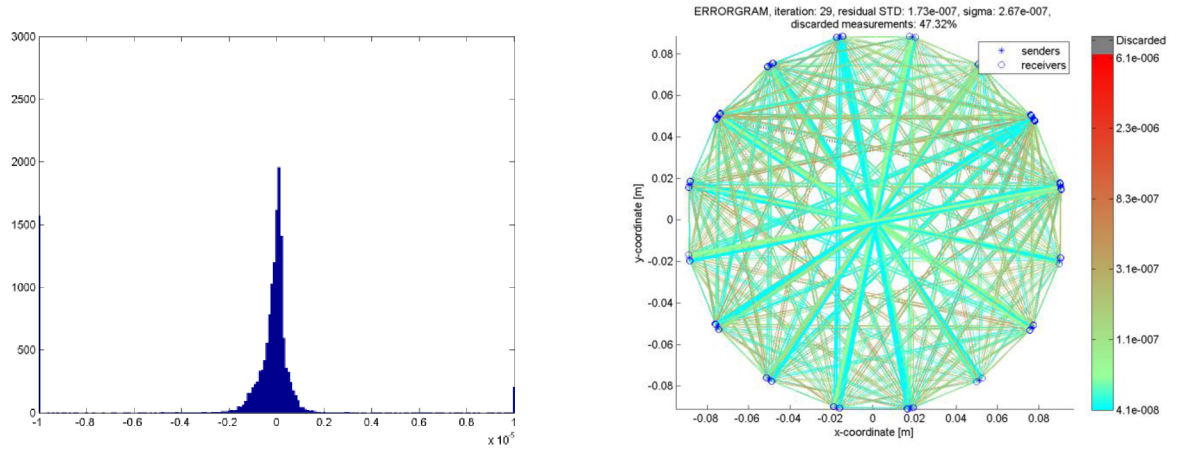


Figure 6-44: After the GNA – LS – CD calibration. Histogram (left) and errorgram (right)

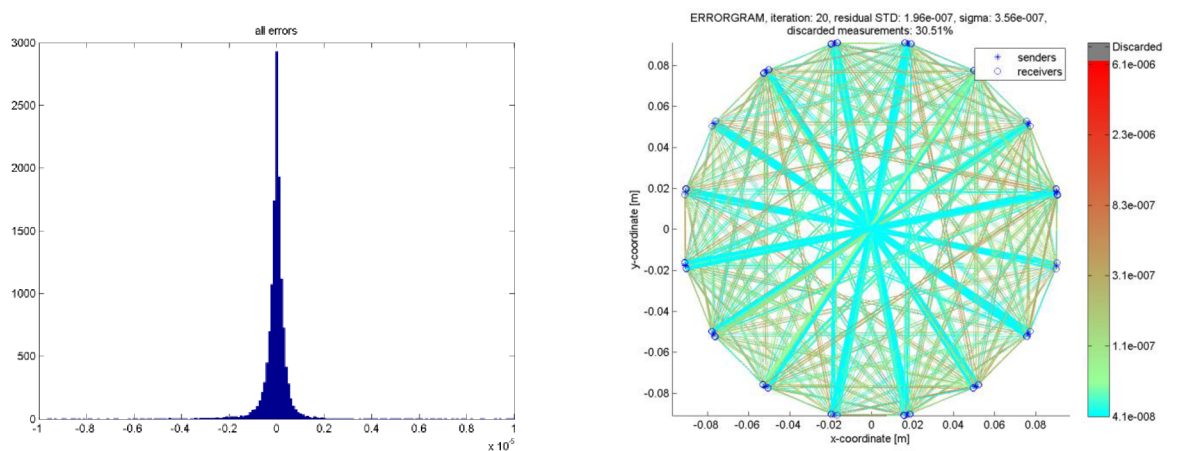


Figure 6-45: After the GNA-LS-AD calibration. Histogram (left) and errorgram (right)

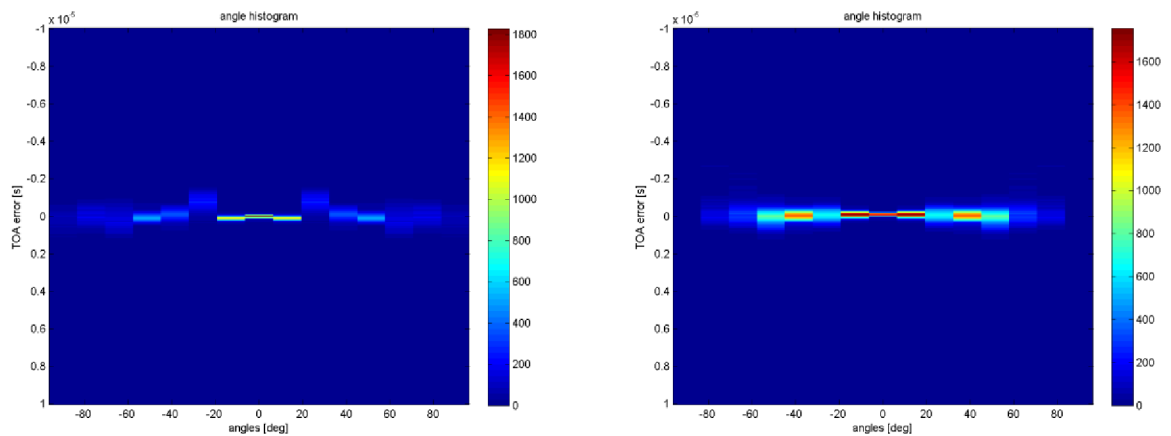


Figure 6-46: Comparison of histograms by emitting/receiving angle. CD method (left), AD (right).

It is interesting to compare the ID and CD models – the later evidently performing slightly better in centering the histogram on zero-error (Figure 6-44). This may be due to the fact that the delay parameters don't differ on a transducer-to-transducer basis. It is rather the bigger robustness of the CD model (the number of unknowns is much smaller) which plays the important role in the calibration.

As stated before, the best performing method surprisingly showed to be the AD model (Figure 6-45), clearly displaying the sharpest peak of the histogram centered on zero-error.

The idea of implementing an angle-dependent delay parameter model originated from the Figure 6-46, showing an angle dependent histogram (for the CD model). The image shows that for different emitting/receiving angles, the peak of the histogram is shifted off the zero-error. For comparison, the same angle-dependent histogram is shown next to it for the AD model. Here, the histogram is centered on the zero-error for all angles. On the main lobe (0 degrees) and the two side lobes (around -40 and 40 degrees) the histogram is sharper, because the higher energy peaks could be detected with better accuracy.

7 Conclusion

The aim of this dissertation was to develop new calibration methods for ultrasound computed tomography systems, which would enhance the quality of the reconstructed images. This chapter summarizes the achieved results and gives recommendations for further research in this area.

7.1 Discussion of the achieved results

The author had the chance to be directly involved in the development of the Karlsruhe USCT experimental device. During several months spent in the Karlsruhe research facility, the author made numerous scans of custom made phantoms using the 2D and 3D USCT devices. These and other scans performed by members of the Karlsruhe team then served as the input of the image reconstruction experiments.

The dissertation work began with an initial research in the area of attenuation image reconstruction (chapter 4). After this first study, it became clear that both the 2D and 3D Karlsruhe USCT devices will need some kind of calibration to produce consistent data. The authors' attention turned to this topic and two main areas of research were identified: the calibration of the sensitivities of the ultrasonic transducer elements (chapter 5), and the geometrical calibration of the system (chapter 6).

The results of work on attenuation imaging and on the two calibration areas are described below.

7.1.1 Attenuation image reconstruction

The first part of work on this dissertation project was mostly concerned with attenuation image reconstruction using data from the Karlsruhe 2D USCT. An initial study was carried out comparing the USCT system geometry with X-ray CT geometry and the possibilities of using the X-ray CT reconstructions techniques were considered.

As an outcome, a new set of rebinning equations (rearranging the fan projections into parallel projections) were formulated (chapter 4.2) specifically for the Karlsruhe 2D USCT. Also an improving modification to a novel reconstruction method utilizing reflected/scattered ultrasonic beams was proposed (chapter 4.3) and published on an international conference in Umea, Sweden [80].

The author made numerous experimental measurements with both the 2D and 3D Karlsruhe USCT systems, using custom-built ultrasonic phantoms. These served as the source data in the development of new image reconstruction algorithms also for other team members.

7.1.2 Sensitivity calibration

A novel method was developed for the 2D USCT. The method consists in solving a large set of log-linearized equations yielding a scalar sensitivity parameter for each transducer element and a directivity pattern common to all transducers. No calibration phantom is needed. All of the measurements are made by the USCT device itself.

The method was implemented in the Matlab programming environment and the results were compared against hydrophone measurements and a wave-equation based simulation. Both comparisons showed reasonable similarity of the results. The method was presented on international conferences in Prague [81] and New York [82].

7.1.3 Geometrical calibration

Most of the research activities were devoted to geometrical calibration of the Karlsruhe 3D USCT. A novel 3D geometrical calibration method (with a few alternative solutions) was developed which, similarly as the sensitivity calibration, does not require any calibration phantoms and the USCT device itself makes all the necessary measurements. The method is inspired by the principles of GPS localization and its time-of-flight based triangulation. The ultrasonic emitters and receivers may be viewed as the satellite transmitters and mobile receiver units in GPS. Contrary to the GPS, where only the receiver's position is unknown, all ultrasonic transducers, emitters and receivers, have to be calibrated in USCT.

The calibration method is defined as an optimization problem, minimizing the squared differences between the measured and estimated time-of-arrival of the ultrasonic pulses. This leads to a solution via Gauss-Newton (or Levenberg-Marquardt) method, iteratively solving a set of nonlinear equations. The method outputs calibrated x , y , and z coordinates of each transducer element and its time-delay parameter.

Because the parameters of all, emitter and receiver, elements are unknown, special attention was given to defining boundary conditions – here called anchors – without which the method does not converge. Due to a large amount of possible anchor combinations and their large effect on final calibration accuracy, a separate analysis was carried out employing a genetic algorithm search for the optimum anchors.

The geometrical calibration method was thoroughly numerically analyzed and tested for performance with simulated noisy measurements.

The author made several scans with the Karlsruhe 3D USCT system. To apply the calibration method to the measured data, the recorded signals had to be preprocessed. De-noising filters were derived based on the signal frequency content. A new algorithm was developed for fast on-line detection of pulses in the recorded signals and a subsequent selection of the pulse corresponding to the direct path from the emitter to the receiver.

The recorded USCT data were applied to the geometrical calibration method (and all the described alternative approaches) and compared. The results are discussed in chapter 6.5.3.

A final test was then performed to see the influence of the calibrated geometry on the reconstructed images. Using the calibrated geometry a reflectivity image of a thread phantom was reconstructed. The phantom consisted of 10 (0.5 mm thick) parallel threads stretched vertically inside the USCT tank. Figure 7-1 compares two reconstructed images (2D horizontal cross-section of the threads) before and after the calibration. As can be seen, the calibration brought a significant improvement in focusing the image.

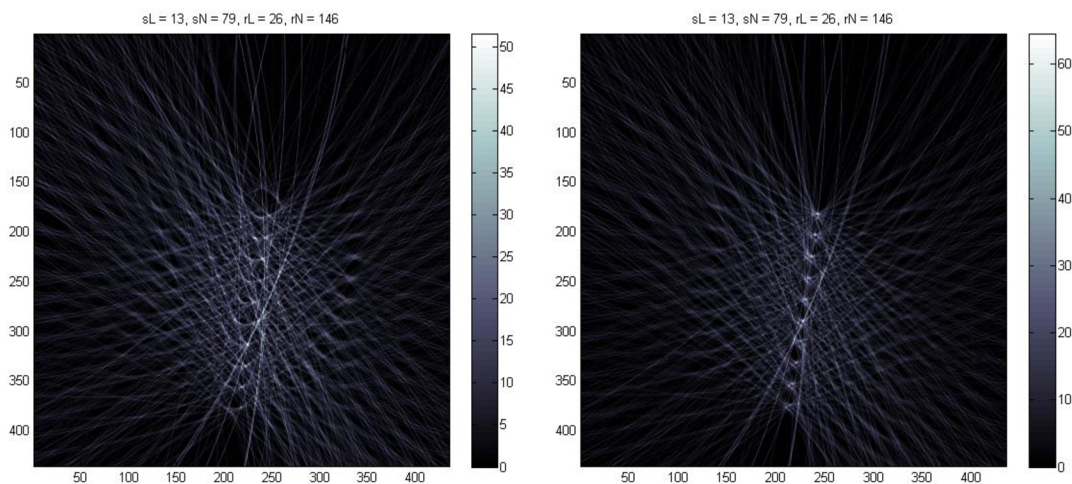


Figure 7-1: Reconstruction of a thread phantom before (left) and after (right) geometrical calibration. The star-shaped artifacts appear because only a low number of A-scans were used.

The calibration method and results were presented on the international conferences in Lyon [84], Riga [85], and Vancouver [86].

7.2 Suggestions for further research

Several new methods and algorithms were developed, implemented and applied to the experimental Karlsruhe USCT data and especially the geometrical calibration shows an increase in quality of the reconstructed images. Nevertheless, there are still ideas, which the author could not achieve to finish in the time of the doctoral studies.

7.2.1 Ethanol solution measurement medium

Considerable sources of uncertainty and errors in both the sensitivity and geometrical calibration originate in the measurements of the speed of sound of the USCT medium. The speed of sound is calculated from a measured temperature of the water inside the USCT tank. The sources of all errors of this method were discussed in chapter 6.5.2. In the future, a more accurate thermometer could provide measurements with smaller error, but the main source of error: the variability of temperature in the USCT tank (and therefore variability of the speed of sound) will always remain.

Giacomini [6] proposes to use a mixture of water and ethanol as a standard ultrasonic medium, where an accurately known speed of sound is of critical importance. Water has a positive temperature coefficient in the interval 0°C to 74°C. Ethanol on the other hand has a negative temperature coefficient in this interval. At a concentration of 17% ethanol in water (by weight), the temperature dependency of the speed of sound vanishes.

A solution of ethanol and water was considered to be used during measurements on the USCT system in FZK Karlsruhe. The author performed several tests of material resistance, which indicated that ethanol could potentially cause damage to parts of the USCT tank - especially the transducer array systems. Because of these tests, it was decided not to use the ethanol solution on the current system.

However, we can assume that the next generations of Karlsruhe USCT system, which will leave the laboratory environment, will have to be constructed from resistant materials to withstand the everyday traffic of patients in the hospitals. Therefore the ethanol solution as a medium for calibration purposes can still remain in consideration for the future.

7.2.2 3D extension to sensitivity calibration

An extended calibration method was also proposed for the 3D USCT. This method takes into account aspects such as the shape of the excitation pulse, the attenuation of the ultrasound pulse along the path from the emitter to the receiver, or the transfer functions of the transducers' electronics. The method is described in chapter 5.2.

7.2.3 Thread phantom calibration

Another alternative to the geometrical calibration was also proposed. This approach utilizes data recorded by the USCT with a thread phantom inside the tank. The A-scans not only show the directly transmitted pulses from an emitter to a receiver, but also reflected pulses from the threads. This information can be used to construct millions of additional equations with just a few more unknowns. The solution thus becomes more stable and less sensitive to measurements noise. The method is fully described in chapter 6.4.5.

7.2.4 LSQR solution to the system of equations

The system of nonlinear equations to be solved in the geometrical calibration is quite extensive (several millions of equations with thousands of unknowns). The proposed calibration method uses the Gauss-Newton or Levenberg-Marquardt methods to solve the equation set. Unfortunately, with these methods it is not possible to solve the complete equation set on 32 bit windows system, which only limits the RAM to 4GB.

An alternative, is to use other methods, such as the LSQR, Kaczmarz, or Newton-Reflection methods. The total computing time increases, because the inversion of the system matrix is done iteratively, but the methods require much less memory. Moreover, the Kaczmarz method can be adapted to a distributed environment and so several computers can simultaneously contribute to the calculations decreasing the total calculation time.

7.2.5 Different pulse shapes, Pulse trains, Chirps

It was not yet tested on the Karlsruhe USCT system if a different pulse shape would enhance the time-of-arrival detection accuracy. Especially the use of a “pulse train” (a set of pulses with defined delay intervals in between) could be useful. Another approach would be to use frequency modulated chirps, which are known to increase the detection accuracy in other ultrasound systems.

7.2.6 Single- and double-differences

Finally, the single- and double-differences approaches could be adapted for the geometrical calibration. In such an approach, pairs of measured TOAs belonging to the same transducer element are subtracted from each other, and these values are then used to set up the equation system. With the subtraction, the time-delay parameter vanishes from the unknowns, and only the geometrical parameters (x,y,z) are part of the solution. The time-delay parameters can then be easily computed based on the solution of the geometrical calibration. Such an approach is documented to be more stable [26],[42].

8 References

- [1] AGREN, S. et. al., *Distance Geometry of Molecules*, 14th ECMI modeling week, Lund, 2000.
- [2] ANDRE, M: et al. *A new consideration of diffraction computed tomography for breast imaging: studies in phantoms and patients*. In *Acoustic Imaging*, vol. 21, 1995.
- [3] ANDRE, M., et al. *Reduction of phase aberration in a diffraction tomography system for breast imaging*. *Acoustical Imaging*, 1996.
- [4] ANDRE, M. P., et al. *High-Speed Data Acquisition in a Diffraction Tomography System Employing Large-Scale Toroidal Arrays*. John Wiley & Sons, Inc. 1997
- [5] AZHARI, H., SAZBON, D. *Volumetric Imaging with Spiral CT*. in *Radiology*, 1999.
- [6] BAMBER J.C., HILL C.R, *Physical Principles of Medical Ultrasonics*, John Wiley and Sons, 2004.
- [7] BEUTEL, J., KUNDEL, H.L., VAN METTER, R., *Handbook of Medical Imaging: Medical Image Processing and Analysis*. SPIE Press, 2000
- [8] BIRCHFIELD, S.T., *Geometric Microphone Array Calibration by Multidimensional Scaling*. IEEE International Conference on Acoustics Speech, and Signal Processing 2003, Hong Kong.
- [9] BIRCHFIELD, S.T., SUBRAMANYA, A. *Microphone Array Position Calibration by Basis-point Classical Multidimensional Scaling*. IEEE Transactions on Speech and Audio Processing, 2004.
- [10] BRONSTEIN, M. M., et al. *Reconstruction in Diffraction Ultrasound Tomography Using Nonuniform FFT*, IEEE Transactions on Medical Imaging vol. 21, no. 11, November 2002.
- [11] BULUSU, B., ESTRIN, D., GIROD, L., *Scalable Coordination for Wireless Sensor Networks: Self-Configuring Localization Systems*, Proceedings of the 6th {IEEE} International Symposium on Communication Theory and Application, 2001.
- [12] CHEW, W.C., et al. *Nonlinear Diffraction tomography, The Use of Inverse Scattering for Imaging*. International Journal of Imaging Systems and Technology, 1996.
- [13] CRAIG, J.J., *Introduction to Robotics: Mechanics and Control*, Addison-Wesley, Reading, Massachusetts, 1989
- [14] COX, T.F., COX, M.M., *Multidimensional scaling*, London, Chapman Hall, 1994.
- [15] DUCK, F. A. *Physical properties of tissue: a comprehensive reference book*. London: Academic Press, 1990.
- [16] DURIC, N ; LITTRUP, P ; BABKIN, A, et al: *Development of Ultrasound Tomography for Breast Imaging: Technical Assessment*, Medical Physics; Journal Volume: 32; Journal Issue: 5, 2004.
- [17] DURIC, N ; LITTRUP, P., RAMA, O., et al: *Computerized Ultrasound Risk Evaluation (CURE): First Clinical Results*. *Acoustical Imaging*, Volume 28, 2007.
- [18] FOLDS, D.L. *Experimental Determination of Ultrasonic Wave Velocities in Plastics, Elastomers, and Synthetic Foam as a Function of Temperature*. *J. Acoust. Soc. Am.*, Vol. 56, No. 4, October 1974.
- [19] GEMMECKE, H., et al.: *First measurements with the Auger fluorescence detector data acquisition system*. Proceedings of the ICRC 2001, 2001.
- [20] GLOOVER, G.H., SHARP, J.C. *Reconstruction of Ultrasound Propagation Speed distributions in Soft Tissue: Time of Flight Tomography*. In IEEE Transactions on Sonic and Ultrasonics, vol. SU-24, no. 4, July 1977.
- [21] GREENLEAF, J. F., et al. *Algebraic reconstruction of spatial distributions of acoustic absorption within tissue from their two dimensional acoustic projections*, in *Acoustical Holography*, vol. 5, P. S. Greene, Ed. New York, NY: Plenum Press, 1974, pp. 591 - 603.
- [22] GREENLEAF, J. F., et al. *Algebraic reconstruction of spatial distributions of acoustic velocities in tissue from their time-of-flight profiles*, in *Acoustical Holography*. H. Booth, Ed. New York, NY: Plenum Press, 1975, pp. 71-90.

- [23] GREENLEAF, J. F., BAHN R. C., *Clinical Imaging with Transmissive Ultrasonic Computerized Tomography*. IEEE Transactions on Biomedical Engineering, 1981. BME-28(2): p. 177-185
- [24] HERVE, A., *Metric Multidimensional Scaling (MDS): Analyzing Distance Matrices*. In: Neil Salkind (Ed.) (2007). Encyclopedia of Measurement and Statistics.
- [25] HILL, C.R., BAMBER, J.C, HARR, G.R. *Physical Principles of Medical Ultrasonics*. John Wiley & Sons Ltd., England, 2004.
- [26] HOFFMANN-WELLENHOF, B., LICHTINEGGER, H., and COLLINS, J., *GPS: Theory and Practice*, 2001, Springer-Verlag Wien.
- [27] HORN, B. K. P., *Fan-Beam Reconstruction Methods*, in Proceedings of the IEEE, vol. 67 no. 12. December 1979.
- [28] JAIN, A.K. *Fundamentals of Digital Image Processing*. Prentice-Hall, 1989.
- [29] JAN, J.: *Medical Image Processing, Reconstruction and Restoration – Concepts and Methods*. CRC Inc. 2005.
- [30] JEONG-WON JEONG, et al. *Soft Tissue Differentiation Using Multiband Signatures of High Resolution Ultrasonic Transmission Tomography*, in IEEE Transactions on Medical Imaging, vol. 24, no. 3, March 2005.
- [31] JIŘÍK R., STOTZKA R, TAXT T. (2005): ‘Ultrasonic Attenuation Tomography Based on Log-Spectrum Analysis,’ Proceedings of SPIE, Medical Imaging 2005. Volume: 5750, 2005.
- [32] JIŘÍK R., TAXT T., JAN J.: *Ultrasound Attenuation Imaging*, Journal of ELECTRICAL ENGINEERING, VOL. 55, NO. 7-8, 2004.
- [33] JANÉE, H.S., ANDRÉ, M.P., YSRAEL, M., et al: *Diffraction Tomography Breast Imaging System: Patient Image Reconstruction and Analysis*. Acoustical Imaging, Volume 24, 2006.
- [34] JONES H.W. *Recent Activity in ultrasonic tomography*. In Ultrasonics 1993, vol. 31, no. 5. 1993.
- [35] KAK A.C, SLANEY M. (2002): Principles of Computerized Tomographic Imaging, IEEE Press, 1988
- [36] KRUCKER, J.F., FOWLKES, J.B, CARSON, P.L., Sound Speed Estimation Using Automatic Ultrasound Image Registration. In IEEE Transactions on Ultrasonics, Ferroelectrics, and Frequency Control, vol. 51, no.9, September 2004.
- [37] LANGLEY, R.B. *Dilution of Precision*. In GPS World, May 1999.
- [38] LAURENT, M., *Matrix completion problems*. In The Encyclopaedia of Optimization, vol. III (Interior - M), pages 221-229, (C.A. Floudas and P.M. Pardalos), 2001.
- [39] LANGEDOEN, K., REIJERS, N., *Distributed localization in wireless sensor networks: a quantitative comparison*. Elsevier Computer Networks 43 (2003) 499–518.
- [40] LEACH, R.R., et-al. *A comparison of ultrasound tomography methods in circular geometry*. In Proc. SPIE Vol. 4687, 2002.
- [41] Li, Y., “Position and Time-Delay Calibration of Transducer Elements in a Sparse Array for Underwater Ultrasound Imaging“, *IEEE Transaction on Ultrasonics, Ferroelectrics, and Frequency Control*, Vol. 53, No.8, Aug. 2006.
- [42] Li, Y. et al. “Single- and Double-Difference Algorithms for Position and Time-Delay Calibration of Transducer Elements in a Sparse Array” *IEEE Transaction on Ultrasonics, Ferroelectrics, and Frequency Control*, Vol. 54, No.6, June 2007.
- [43] LITRUP, P.J., DURIC, N., AZEVADO, D., et al: *Computerized Ultrasound Risk Evaluation (CURE) System: Development of Combined Transmission and Reflection Ultrasound with New Reconstruction Algorithms for Breast Imaging*. 26th International Acoustical Imaging Symposium, Ontario, Canada, 2001.
- [44] MARCZAK W. *Water as a standard in the measurements of speed of sound in liquids*. J. Acoust. Soc. Am. 102(5) pp 2776-2779. 1997
- [45] MASATOSHI S. *Genetic Algorithms And Fuzzy Multiobjective Optimization*. Springer. 2002
- [46] MATLAB[®] v. 7.1 (R14) manual, Mathworks 2005 (www.mathworks.com/products/matlab)

- [47] Matweb contributors, "AISI 316L" *Matweb – Material property data*, <http://www.matweb.com>.
- [48] MICHAELSON, J.S., et al. *Predicting the Survival of Patients with Breast Carcinoma using Tumor Size*. In *Cancer*, vol. 95, no. 4, American Cancer Society, 2002.
- [49] MING, L.: *Ultrasound computer tomography image reconstruction regarding object and sensor properties*, Master thesis, Forschungszentrum Karlsruhe, University of Applied Science Karlsruhe, 2003.
- [50] MOSES, R., PATTERSON, R., GARBER, W., Self Localization of Acoustic Sensor Networks. *Eurasip Journal on Applied Signal Processing, Special Issue on Sensor Networks*, Vol. 2003, No. 4, pp. 148-158, Mar. 2003.
- [51] MULLER, T.O. et al.: *Ultrasound computertomography: image reconstruction using local absorption and sound speed profiles*, ESEM - European Society for Engineering and Medicine, 2003.
- [52] NORTON, S. J., LINZER, M. *Ultrasonic Reflectivity Tomography: Reconstruction with Circular Transducer Arrays*, in *Ultrasonic Imaging 1*, Academic Press Inc., 1979
- [53] NOCEDAL, J., WRIGTH, S.J., *Numerical Optimization*. Springer 1999.
- [54] POULARIKAS, A.D. *The Transforms and Applications Handbook*, second edition. CRC Press, 2000.
- [55] PRASOLOV, V.V., TIKHOMIROV, V. M. *Geometry*, American Mathematical Society, Providence, Rhode Island, USA 2001.
- [56] PRESS, W. H. et al.: *Numerical Recipes in C, The Art of Scientific Computing (Second edition)*, Cambridge University Press, 2002.
- [57] QUIST, M., YONA, G., *Distributional Scaling: An Algorithm for Structure-Preserving Embedding of Metric and Nonmetric Spaces*. *Journal of Machine Learning Research* 5 (2004) 399–430.
- [58] RUITER, N.V., et. al. *3D Ultrasound Computer Tomography: Results with a Clinical Breast Phantom*, IEEE Ultrasonics, 2006.
- [59] RUITER, N.V., et. al. *Ultrasound Computer Tomography: An Addition to MRI?* *European Radiology*, 16, Suppl. 5, pp. 82-85, 2006.
- [60] RUITER, N. et al. *Evaluation of Different Approaches for Transmission Tomography in Ultrasound Computer Tomography*.: <http://fuzzy.fzk.de/~mueller/publications/%5BRui05%5D%20Evaluation%20of%20Different%20Approaches%20of%20Transmission%20Tomography%20in%20Ultrasound%20Computer%20Tomography.pdf>
- [61] ROZMAN, J. *Ultrazvuková technika v lékařství – Diagnostické systémy*. Czech Republic: Ediční středisko VUT Brno, 1979.
- [62] SCHRIEMAN, J. S., et. al., *Ultrasound Transmission Computed Tomography of the Breast*. *Radiology*, 1984. 150: p. 523-530
- [63] SCHMITT, M.R., et al (1984): *Error Reduction in Through Transmission Tomography Using Large Receiving Arrays with Phase-Insensitive Signal Processing*, IEEE Transactions on Sonics and Ultrasonics, vol. SU-31, no. 4, July 1984.
- [64] SMITH, W. *Piezocomposite materials for acoustical imaging transducers*, in *Acoustical Imaging 21*, pp. 121-138, 1995.
- [65] STOTZKA, R., et al (2002): *Medical Imaging by Ultrasound-Computertomography*, SPIE Medical Imaging, 2002 / 25.
- [66] STOTZKA, R., et al: *Ultrasound computer tomography for breast cancer diagnosis*, 7th conference of the European Society for Engineering and Medicine, 2003.
- [67] STOTZKA, R., GOBEL, G., SCHLOTE-HOLUBEK, K. *Development of transducer arrays for ultrasound computer tomography*, Forschungszentrum Karlsruhe, 2004.
- [68] STOTZKA, R., et al. *A New 3D Ultrasound Computer Tomography Demonstration System*, Forschungszentrum Karlsruhe, 2004.
- [69] STOTZKA, R., et al. *Prototype of a new 3D ultrasound computer tomography system: transducer design and data recording*, in *SPIE Medical Imaging 2*, 2004.

- [70] STOTZKA, R., et. al., *High resolution image reconstruction in ultrasound computer tomography using deconvolution*, Proc. SPIE Med. Imag., 5750, pp. 325-325, 2005.
- [71] TORSSET, M.W., Distance Matrix Completion by Numerical Optimization, *Comput. Optim. Appl.* 17, Oct. 2000.
- [72] VIOLA, F., WALKER, W.F., A Spline-Based algorithm for Continuous Time-Delay Estimation Using Sampled data, in *IEEE Transactions on Ultrasonics, Ferroelectrics, and Frequency Control*, vol. 51, no.9, September 2004.
- [73] WAAG, R., FEDWA, R.: *A Ring transducer system for Medical Ultrasound Research*, in IEEE Transactions on Ultrasonics, Ferroelectrics, and Frequency Control, vol. 53, no.10, October 2006.
- [74] WHO, "Global cancer rates could increase by 50% to 15 million by 2020", *World Health Organisation*, <http://www.who.int/mediacentre/news/releases/2003/pr27/en/> (accessed July 4, 2008)
- [75] Wikipedia contributors, "Coefficient of thermal expansion," *Wikipedia, The Free Encyclopedia*, http://en.wikipedia.org/w/index.php?title=Coefficient_of_thermal_expansion&oldid=163610299 (accessed October 10, 2007).
- [76] Wikipedia contributors, "Levenberg-Marquardt algorithm," *Wikipedia, The Free Encyclopedia*, http://en.wikipedia.org/w/index.php?title=Levenberg-Marquardt_algorithm&oldid=152452539 (accessed September 20, 2007).

9 List of author's publications

- [77] FILIPÍK, A., JAN, J. *Reconstructing attenuation Images in Ultrasonic Computed Tomography*. In Proceedings of Radioelektronika 2005 conference, Brno, 2005.
- [78] FILIPÍK, A. *Attenuation Imaging in Ultrasonic Computed Tomography*. In Proceedings of Poster 2005 conference, Prague, 2005.
- [79] FILIPÍK, A., JAN, J. *Ultrasonic Attenuation in Computed Tomography*. In Proceedings of Student EEICT 2005 conference, Brno, 2005.
- [80] FILIPÍK, A., JIŘÍK, R., JAN, J. *Ultrasonic Attenuation Imaging Using Coherent Processing in Ultrasonic Computed Tomography*. In Proceedings of the 13th Nordic Baltic Conference on Biomedical Engineering and medical Physics: Swedish Society for Medical Engineering and Medical Physics, 2005, p. 119 - 120, Umea, Sweden, 2005.
- [81] FILIPÍK, A., JAN, J., JIŘÍK, R. *Transducer Calibration in Transmission Ultrasound Tomography* In IFMBE Proceedings (EMBEC). The 3rd European Medical and Biological Engineering Conference EMBEC'05. Praha: IFMBE, 2005, p. 450 – 453.
- [82] ZAČAL, J., HEMZAL, D., JAN, J., FILIPÍK, A., JIŘÍK, R., KOLÁŘ, R. *Comparison of Wave-Equation Versus Measurement-Processing Transducer Calibration for Ultrasonic Transmission Tomography* In Proceedings of 28th Annual International Conference IEEE EMBS. 28th Annual International Conference IEEE EMBS 2006. New York (USA), 2006, p. 2754 - 2 757.
- [83] FILIPÍK, A., JAN, J., JIŘÍK, R. *Calibration of a Transmission Ultrasound Computed Tomography System* In Abstracts of 2nd Int. Workshop on Data-Algorithms-Decision making. 2nd intern. workshop on Data - Algorithms - Decision Making. Třešť: UTIA AVČR Praha, 2006
- [84] FILIPÍK, A., PETERLÍK, I., HEMZAL, D., et al: *Calibrating an Ultrasonic Computed Tomography System Using a Time-of-Flight Based Positioning Algorithm*. EMBS 2007. 29th Annual International Conference of the IEEE, Lyon, France, 2007.
- [85] FILIPÍK, A., JAN, J., PETERLÍK, I., HEMZAL, D., JIŘÍK, R. *Two aspects of Calibrating a 3D Ultrasonic Computed Tomography System*, IFMBE Proceedings, 14th Nordic-Baltic Conference on Biomedical Engineering and Medical Physics NBC 2008, Riga, Latvia, 2008
- [86] FILIPÍK, A., JAN, J., PETERLÍK, I., et al: *Modified time-of-flight based calibration approach for ultrasonic computed tomography*, EMBS 2008, 30th Annual International Conference of the IEEE, Vancouver, Canada 2008.